Translocator Protein and Methionine PET Imaging in Glioma

A thesis submitted to the University of Manchester for the degree of Doctor of Philosophy in the Faculty of Biology, Medicine and Health

2019

Erjon Agushi

UNIVERSITY OF MANCHESTER – SCHOOL OF HEALTH SCIENCES

Blank page

Table of Contents

Final Word Count = 40,532

List of Figures

List of Tables

Abstract

Introduction: Brain tumours continue to present specific imaging challenges, in particular related to grading and progression, from initial diagnosis, through surveillance and treatment planning, to response assessment and prognostication. In this project we explored the role of advanced MR biomarkers and PET imaging with two different tracers in glioma, [^{11}C]-Methionine and TSPO-binding ligand [^{11}C]-(R)-PK11195. Both PET tracers are ubiquitously low in the normal brain and high in the pathological tissue.

Methods: In the first experimental chapter we investigated the role of [^{11}C]-(R)-PK11195 and relative cerebral blood volume (rCBV) in prediction of transformation in a cohort of 26 low grade gliomas (LGGs). Results were further validated on tissue derived from a consecutive cohort of 30 oligodendroglial tumours. The second step of our study extended to a larger cohort of 41 low and high grade gliomas, where we compared [^{11}C]-Methionine uptake to rCBV and diffusion tensor imaging (DTI) derived metrics in correlation to strongest signal areas of the tumour. Finally, in the last chapter we investigated the extent and potential causes of neuro-inflammation in the normal appearing brain of 66 patients with glioma, comparing to a cohort of 19 healthy controls and 27 patients with other types of intracranial tumours.

Results: Progressively higher uptake of [11C]-(R)PK11195 was seen in anaplastic gliomas compared to the lower grade ($p=0.001$), whilst rCBV failed to show a significant difference ($p=0.23$). Tissue data from TSPO antibody staining showed a very good correlation to the imaging results and were further validated in a cohort of 30 oligodendroglial tumours (sensitivity 92.85% and specificity 93.75%). In the second study, significant [11C]-Methionine uptake was seen with increasing histological grade ($p<0.001$). Significant rank correlations were identified between peak methionine uptake ratios and peak values for both relative blood volume ($p=0.004$) and flow ($p=0.036$). Correlation of peak methionine values was additionally noted to inversely correlate with trough values of mean diffusivity ($p=0.001$). Tumours with vivid [11C]-Methionine uptake appeared to have a poorer prognosis with shorter time-to-progression interval ($p=0.015$). Lastly, we found increased microglia activation, in both cerebral hemispheres in glioma patients compared to controls. This was most prominent in the tumour-bearing hemisphere ($p<0.0001$) but was also evident in the controlateral hemisphere ($p=0.0078$). Patients presenting with seizures showed a positive correlation between extra-tumoural microglial activation in the cerebrum and the duration of epilepsy.

Conclusions: TSPO PET imaging can offer good accuracy in prediction of transformation which can be also translated in tissue analysis via antibody staining. Identifying tumour most malignant regions can be trivial using only MR derived data and PET imaging with [11C]-Methionine can contribute to better surgical planning and understanding of tumour microenvironment. Increased neuro-inflammation in patients with glioma is linked to seizure activity, although it is difficult to ascertain cause and effect.

Declaration

No portion of the work referred to in this thesis has been submitted in support of an application for another degree or qualification of this or any other university or other institute of learning.

Copyright Statement

i. The author of this thesis (including any appendices and/or schedules to this thesis) owns certain copyright or related rights in it (the "Copyright") and s/he has given The University of Manchester certain rights to use such Copyright, including for administrative purposes.

ii. Copies of this thesis, either in full or in extracts and whether in hard or electronic copy, may be made only in accordance with the Copyright, Designs and Patents Act 1988 (as amended) and regulations issued under it or, where appropriate, in accordance with licensing agreements which the University has from time to time. This page must form part of any such copies made.

iii. The ownership of certain Copyright, patents, designs, trademarks and other intellectual property (the "Intellectual Property") and any reproductions of copyright works in the thesis, for example graphs and tables ("Reproductions"), which may be described in this thesis, may not be owned by the author and may be owned by third parties. Such Intellectual Property and Reproductions cannot and must not be made available for use without the prior written permission of the owner(s) of the relevant Intellectual Property and/or Reproductions.

iv. Further information on the conditions under which disclosure, publication and commercialisation of this thesis, the Copyright and any Intellectual Property and/or Reproductions described in it may take place is available in the University IP Policy (http://documents.manchester.ac.uk/DocuInfo.aspx?DocID=24420), in any relevant Thesis restriction declarations deposited in the University Library, The University Library's regulations and in The University's policy on Presentation of Theses (http://www.library.manchester.ac.uk/about/regulations/).

Acknowledgements

Firstly, my deep gratefulness is own to my mentors Prof Alan Jackson and Mr David Coope, who have put their faith on me into this great endeavour. Without their support, expertise and enthusiasm it would have been impossible to succeed.

I would also like to acknowledge Cancer Research UK for their generous funding which made this research possible.

As in any research project, even the simplest task takes considerable time, dedication and joint team efforts. This thesis would have been impossible without the contributions of my colleagues and friends. In particular would like to praise Dr Rainer Hinz, Prof Federico Roncaroli, Dr Ibrahim Djoukhadar, Dr Zhangjie Su, Dr Jose-Anton Rodriguez, Dr Ka-loh Li, Dr Xiaoping Zhu, Dr Marie-Claude Anselin, Mr Daniel Lewis and Mr Mueez Waqar for the help in recruitment, data processing, tissue analysis and their constructive feedback on the manuscripts.

Enormous thanks goes also to all the Neurosurgeons and Oncologists for their dedication and help in the recruitment for this project, especially Prof Andrew King, Mrs Konstantina Karabatsou, Mr Pietro D'Urso, Mr James Leggate, Mr Matthew Bailey, Dr Catherine McBain, Dr Rao Gattamaneni, Dr Stephen Kennedy, Dr Gillian Whitfield, Dr Roven Colaco.

A number of other people have further contributed to this project, no matter how small or big, their support has proven crucial to the project: Eleanor Duncan-Rose, Diana Almeida, Barry Whitnall, Neal Sherratt, Sarah Lehmann, Harris Khan, Sarah Wood, Denise Ogden, Richard Smallmen, and Catherine Shortt.

Finally, but most importantly, my most profound gratitude and admiration is reserved to all the participants in this research who sacrificed their time, despite going through the most difficult period of their life.

I will always be grateful and indebt to all of you.

Dedication

To my wife Amada and our wonderful daughter Aria

Thank you

List of Abbreviations

AA	Anaplastic Astrocytoma
ADC	Apparent Diffusion Coefficient
AO	Anaplastic Oligodendroglioma
BPND	Binding Potential Non-Displaceable ratio at equilibrium of specifically bound radioligand to that of non-displaceable radioligand in tissue.
CBF	Cerebral Blood Flow
CBV	Cerebral Blood Volume
CE	Contrast Enhancement
CMZ	Carbamazepine
CNS	Central Nervous System
CSF	Cerebrospinal Fluid
DIF	Double Immunofluorescence
DOI	Depth of Interaction
DSC	Dynamic Susceptibility Contrast imaging
DTI	Diffusion Tensor Imaging
EPI	Echo Plannar Imaging
FA	Fractional Anisotropy
FDG	[18F]-fluoro-deoxyglucose
FET	Fluoro-Ethyl-Tyrosine
FISH	Fluorescence In Situ Hybridization
FLAIR	Fluid Attenuation Inversion Recovery
FOV	Field of View
FWHM	Full Width at Half Maximum
GAMM	Glioma Associated Macrophages and Microglia
GBM	Glioblastoma Multiforme
GM	Grey Matter
HE	Hematoxylin-Eosin
HGG	High Grade Glioma
HRRT	High Resolution Research Tomography
IDH	Isocitrate Dehydrogenase
IHC	Immunohistochemistry
KM	Kaplan-Meiers
LAM	Lamotrigine
LAT	Large Amino acid Transporter
LEV	Levetiracetam
LGA	Low Grade Astrocytoma
LGG	Low Grade Glioma
LGO	Low Grade Oligodendroglioma
LSO	Lutetium oxyorthosilicate
LYSO	Lutetium–yttrium oxyorthosilicate
MBq	Mega Bequerel
MD	Mean Diffusivity
MDT	Multidisciplinary Meeting
MET	Metastasis

MetPET	[11C]-Methionine PET imaging
MR	Magnetic Resonance
MRI	Magnetic Resonance Imaging
MST	Median Survival Time
MTT	Mean Transition Time
NAB	Normal Appearing Brain
OD	Optical Density
OP-OSEM	Ordinary Poisson Ordered-Subset Expectation Maximization
PBR	Peripheral Benzodiazepine Receptor
PET	Positron Emission Tomography
PHEN	Phenytoin
PS	Pixel Size
ptxGBM	Post-Treatment Glioblastoma Multiforme
rCBF	relative Cerebral Blood Flow
rCBV	relative Cerebral Blood Volume
ROI	Region of Interest
SD	Standard Deviation
SRFT	Salford Royal NHS Foundation Trust
SRTM	Simplified Reference Tissue Model
ST	Slice Thickness
T/N	Tumour/Normal
TE	Echo Time
TI	Inversion Time
TLGG	Transforming Low grade Glioma
TMA	Tissue Microarray
TR	Repetition Time
TSPO	Translocator Protein
VAL	Valproate
VOI	Volume of Interest
VS	Vestibular Schwannoma
WHO	World Health Organization
WM	White Matter
WMIC	Wolfson Molecular Imaging Centre

Blank page

Chapter 1 – The Journal Format of thesis

1.1 Overview and Rationale

The use of PET imaging is growing in neuro-oncology and slowly entering clinical practice but much work is needed to validate molecular imaging data versus conventional imaging modalities. Very few studies have applied tissue analysis to confirm and optimise molecular imaging.

The overall aim of my project is to investigate the suitability of molecular imaging modalities with commonly used tracers in patients with glioma. Specifically, this study evaluates advanced magnetic resonance (MR) and positron emission tomography (PET) imaging using [^{11}C]-(*R*)PK11195 and [^{11}C]Methionine in patients with primary brain tumours and correlates the results to the tissue markers.

The thesis will be presented in the Journal Thesis format, allowing incorporating sections that are in a format suitable for submission in peer reviewed journals. Due to my clinical work and shared time with ongoing research activities, the Journal Thesis format would allow adequate and more efficient use of time to prepare the manuscripts. Additionally peer-reviewed feedback would be further beneficial to improve writing and defending of my thesis.

1.2 Study objectives

The objectives of this study are:

i. To assess [^{11}C]-(*R*)-PK11195 uptake characteristics in the early identification of transformation in low grade gliomas(LGG)
ii. To correlate tumour extension and characteristics of [^{11}C]-Methionine uptake to MR perfusion and diffusion parameters
iii. To investigate neuro-inflammation in the normal appearing brain of patients with glioma using [^{11}C]-(*R*)-PK11195 PET imaging

1.3 Thesis outline

Chapter 1 - This chapter contains a brief summary of the work presented in the thesis. The general structure consists of two sections, the first describing detailed methodology and context literature review on [^{11}C]-(*R*)-PK11195 and [^{11}C]-Methionine PET imaging in glioma. The second section represents three experimental chapters drafted as original research manuscripts.

Chapter 2 – A comprehensive and updated review of previous literature in glioma [^{11}C]-(*R*)-PK11195 and [^{11}C]-Methionine PET imaging is provided. Additionally, concepts of MR perfusion and diffusion in glioma invasion are discussed in the context of the research questions to be answered.

Chapter 3 – This chapter underlines in more detail the methodological approach to the study objectives and aims. A brief introduction as well as key image acquisition and processing are included.

Chapter 4 – TSPO PET imaging in TLGG is the first experimental chapter which has been submitted to the Journal of Clinical Cancer Research. This chapter highlights the advantages of [^{11}C]-(*R*)-PK11195 PET imaging in early diagnosis of transformation, especially in the oligodendroglial type.

Chapter 5 - [^{11}C]-Methionine PET imaging and advanced MR imaging in glioma, submitted to Journal of Neuro-Oncology. This chapter investigates tumour extension and [^{11}C]-Methionine uptake in correlation to MR diffusion and perfusion metrics. Additionally it demonstrates the utilty of [^{11}C]-Methionine in surgical planning and prognostication.

Chapter 6 – Seizure correlation to neuroinflammation in the normal appearing brain of brain tumour patients. In this chapter the microglial activation has been assessed in the whole brain excluding tumour and abnormal areas using [^{11}C]-(R)-PK11195. The findings presented describe an overall inflammatory response of the brain as a whole organ against the tumour triggered by seizures rather than a focal disease. The final draft is in preparation for submission to the Lancet Neurology.

Chapter 7 – Summary of the findings and extension of the discussion from the experimental chapters with future perspectives.

Chapter 2 – Background and Rationale

2.1 Glioma grading and prognosis

Gliomas account for more than 70% of primary brain neoplasms in adults [1]. For almost a century, gliomas have been classified according to the World Health Organization (WHO) classification based on their light microscopic and molecular features. They were graded from I to IV on the basis of their light microscopic features such as nuclear atypia, mitotic activity, endothelial cell proliferation and necrosis. WHO grade I and II were classified as low-grade gliomas (LGGs), and grade III and IV as high-grade gliomas (HGGs). The WHO classification has evolved with the understanding of the physiopathological mechanisms and clinical course, leading to implementation of the molecular profile integrated in the classification system on the last revised edition [2]. This use of integrated phenotypic and genotypic features in the last updated classification has added more conformity and objectivity in diagnostication.

In this new classification, the diffuse gliomas include the WHO grade II and grade III astrocytic tumors, the grade II and III oligodendrogliomas, the grade IV glioblastomas, as well as the related diffuse gliomas of childhood. This approach leaves those astrocytomas that have a more circumscribed growth pattern with lack of IDH gene family alterations and frequently have BRAF alterations (pilocytic astrocytoma, pleomorphic xanthastrocytoma) distinct from the diffuse gliomas. The major refinement on the updated guidelines relates to the abolishment of the previous oligoastrocytoma classification. The two previously known molecular alterations that have well-established associations with prognosis [3], isocitrate dehydrogenase (IDH) mutations and 1p/19q-codeletions, were implemented to separate into more biologically distinct entities than histological classification alone. Among the numerous molecular alterations, these two are particularly noteworthy, because they occur early during glioma formation, are prevalent in glioma, and strongly associated with overall survival.

The first alteration, the codeletion of chromosome arms 1p and 19q (1p/19q codeletion), has been associated with the oligodendroglial histologic type and with sensitivity to chemotherapy with alkylating agents [4, 5]. The second mutation in

either IDH1 or IDH2 (these genes are very similar to one another and are collectively referred to as IDH), which is not restricted to a specific histopathological type of glioma but instead has been associated with a distinctive tumour-cell metabolism[6]. Using both genotype (IDH mutation and 1p/19q codeletion status) and phenotype to diagnose these tumors has resulted in more homogeneous defined groups, with only rare reports of molecularly "true" oligoastrocytomas consisting of histologically and genetically distinct astrocytic (IDH-mutant, ATRX-mutant, 1p/19q-intact) and oligodendroglial (IDH-mutant, ATRX-wildtype and 1p/19q-codeleted) tumor populations (Figure 2.1).

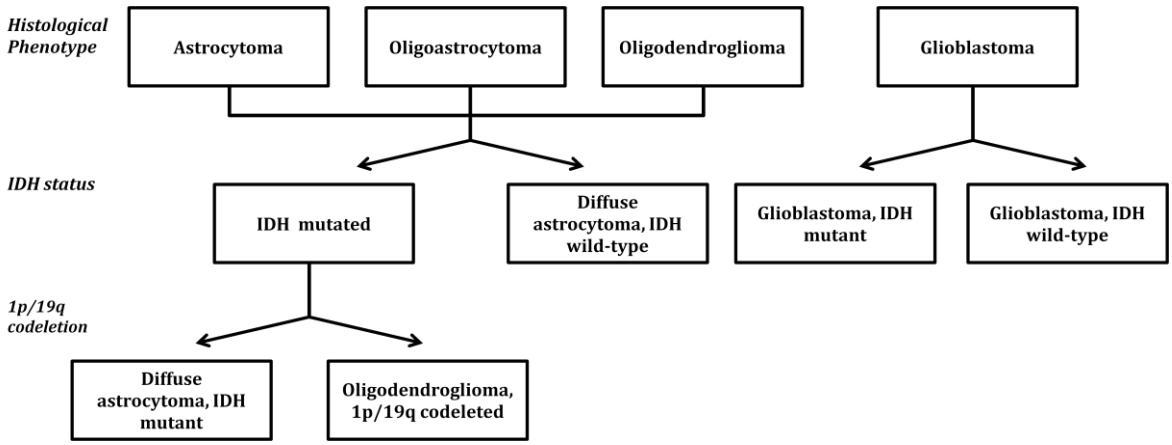

Figure 2.1 Simplified representation of WHO 2016 classification [2] using the histological phenotype and molecular markers for IDH mutation and 1p/19q codeletion.

Most gliomas have poor prognosis due to their invasive growth, high propensity for recurrence and limited response to radio- or chemotherapy [2, 7-9]. Progressive advances in surgery, radio- and chemotherapy, altogether with better understanding of physiopathology and molecular marker implementation have improved just ever slightly the prognosis of glioma patients. The average survival time in glioblastoma multiforme (GBM) is expected 12-18 months following maximal safe resection and adjuvant therapy, with only 25% of glioblastoma patients surviving more than one year, and only 5% of patients more than five years[10, 11].

The prognosis of astrocytoma patients also remains dismal, with only 55·9% of anaplastic astrocytomas WHO grade III (1p/19q non-codeleted) reaching the 5-year

survival (95%CI; 47·2–63·8) and a median progression-free survival (PFS) time of 42·8 months (95%CI; 28·6–60·6) [12]. Anaplastic oligodendrogliomas instead have been noted to have a better prognosis with some early trials showing up to 70% response to chemotherapy with procarbazine, lomustine, and vincristine (PCV)[13, 14]. The latest randomized trials have shown an improved overall survival (OS) in anaplastic oligodendrogliomas (1p/19q codeleted) treated with radiotherapy and PCV, reaching a median OS of 122.8 months (95%CI; 95.0 – NR) and median progression-free survival time of 75.7 months (95% CI;49.9 to 136.8)[5].

Finally the LGGs have shown better outcomes with astrocytomas WHO grade II (IDH mutant) showing a median OS of 115.2 (95%CI; 55.4-164.0) although with a similar median PFS to anaplastic astrocytomas (43.2 months, 95%CI; 35.7-60.0). Whilst 1p/19q codeleted oligodendrogliomas of WHO grade II have a significantly better median OS (163.7 months, 95%CI; 67.3-235.4) with a median PFS of 59.20 months (95%CI; 46.3-91.2)[15]. Yet, even in low grade tumours with IDH mutation and 1p/19q codeletion, tumour recurrence is still the norm [16, 17]. Along with histological grade and type, age of patients is also an important predictive factor of prognosis. Young age at diagnosis is correlated with longer survival of patients with LGGs or HGGs at the population level, while old age remains a significant predictor for poor outcomes [18, 19].

Approximately two-thirds of LGGs progress to HGGs over 4 to 5 years from onset. At present, this particular triggering point in time of malignant progression cannot be accurately predicted based on data obtained from routine brain tumour protocols used in clinical setting [20-25]. Among increasing novel imaging techniques, measurements of tumour blood volume changes have shown an increased risk of malignant transformation [26-28]. In most of the cases, once the transformation has occurred the progression to a higher grade is rapid and disease will follow a fatal course in virtually all patients with gliomas [8, 29]. Thus prediction of malignant transformation and early identification of recurrence in the already resected tumours are among the most important clinical goals in the management of gliomas. Currently, most therapeutic strategies are largely based around active monitoring of disease progression using serial conventional contrast enhanced MRI with physiologic imaging performed in selected cases.

2.2 MRI Imaging in Glioma

MRI remains the modality of choice to investigate gliomas. MRI can offer an accurate morphological and anatomical information regarding the tumour although clinical protocols mainly offer only limited details on the biological features and activity of each tumour[30, 31]. MRI is used largely in clinical setting to detect and localize lesions, define the target area for biopsies, plan surgical and radiation interventions and assess tumour progression and treatment outcome.

MRI can be a versatile and powerful diagnostic tool although acquisition time and consistency in protocols remains a challenge in clinical setting. Dynamic MRI techniques for deriving perfusion and permeability metrics have been of particular interest with T2* dynamic susceptibility contrast (DSC) enhanced MRI being the most widely available [31]. Derived parameters include relative cerebral blood flow (rCBF) and relative cerebral blood volume (rCBV), which has been shown to correlate with microvessel density in human gliomas [32]. Increasing rCBV values have been found in higher grade tumours [26]and perhaps more importantly increases in rCBV have been noted to precede the appearance of contrast enhancement by up to 12 months [27]. Peak rCBV has also been used to determine appropriate targets for biopsy particularly in non-enhancing gliomas that would otherwise pose a challenge [33].

Another important and widely used MRI modality is diffusion-weighted imaging (DWI) which can be used to derive information reflecting changes in the micro-environment both of the tumour and of the surrounding brain. DWI has been very usefully implemented in several clinical settings including ischemic and demyelinating inflammatory diseases, in addition to studies involving normal brain structures. The technique utilises the Brownian self-diffusion characteristics of water molecules in generating images by applying different magnetic gradients to the area studied. Movement of water between areas of different magnetic strength causes a measurable signal drop from which the apparent diffusion coefficient (ADC) can be calculated. The b value is a summary diffusion weighting factor which encapsulates those aspects of the particular pulse sequence which impart sensitivity to proton mobility, such as the duration, direction, and magnitude[34].

An important and useful enhancement to DWI is the Diffusion tensor imaging (DTI), which is an extension to the standard diffusion protocol where the scanned medium

is assumed to exhibit anisotropic diffusion of water and this movement is further characterised. By measuring diffusion in at least 6 non-collinear, non-coplanar directions, with a suitable gradient arrangement, a nine element, second order 3D tensor can be populated. The eigenvectors and eigenvalues derived from solving this tensor describe an ellipsoid which effectively demonstrates three dimensional diffusion magnitude and direction with respect to the FoV [35, 36]. The sphericity relates to the degree of directionality or anisotropy, while the size relates to the rate of diffusion. The mean eigenvalue produces a rotationally invariant measure of diffusivity (mean diffusivity – MD), which is the DTI equivalent of DWI-derived ADC. The ratio of longitudinal to transverse or radial diffusivity gives a second rotationally invariant measure from DTI indicating the degree of diffusion anisotropy (fractional anisotropy – FA)[34].

Two main roles have been described for the DTI application in gliomas; further diffusion characterisation of the tumour and mapping of any distorted or broken white matter tracts by the tumour invasion or infiltration. In gliomas, the normal brain architecture can be disrupted by oedema, tumour infiltration or necrosis. Astrocytomas have shown increased diffusion compared to normal brain with a trend towards lower ACD values in higher grades [37]. This probably reflects a restriction of water movement with increased cellularity. Increased ADC values have been noted from oedematous areas surrounding metastatic tumours, which could represent increased endothelial permeability or could simply reflect increased cellularity from local tumour invasion [38, 39]. In vivo studies have, however produced mixed results [39-41]. This inconsistency may reflect the influence of changes in the extra-cellular space whose constituents and physical characteristics also vary with histological grade in-line with the measured decrease in local diffusivity[42]. Few studies have suggested that MD (or the equivalent ADC), can be used to differentiate between normal white matter and enhancing tumour margin or vasogenic oedema in HGG [43]. It has also been suggested that FA values of the tumour core can be used to discriminate between LGG and HGG [44].

Although these recently developed techniques and the improvement of previous modalities with empowerment of resolution of the MR scanners have been promising, they are not yet able to fully characterise gliomas.

2.3 TSPO and its role in Glioma

The translocator protein (TSPO), formerly known as the peripheral benzodiazepine receptor (PBR) [45] is a high affinity cholesterol- and drug-binding protein located in the outer mitochondrial membrane of a variety of cell types. This 18 kDa protein is a ubiquitous mitochondrial protein with five transmembrane domain protein found as a monomer, dimer and polymer [46, 47], containing separate drug and cholesterol binding domains [48, 49]. TSPO role in normal cells has been described mainly as a "housekeeping" protein. Studies of its responses to drug and endogenous ligands have shown TSPO to be involved either directly or indirectly in numerous biological functions, including mitochondrial cholesterol transport and steroid hormone biosynthesis, porphyrin transport and heme synthesis, apoptosis, cell proliferation, and anion transport[50-52]. In the normal CNS, TSPO expression is low and limited to vessels, ependyma and choroid plexus; in pathological conditions, TSPO increases in microglia/macrophages as well as reactive astrocytes, and becomes abundant in the tissue affected by a wide range of diseases [53], establishing the TSPO as a generic marker for detection of active disease processes in the brain [53-55]. It is up-regulated as a reaction not only to acute insults such as stroke and traumatic brain injury, but also in chronic diseases including Alzheimer's disease, Parkinson's disease, Huntington's disease, multiple sclerosis, and multiple system atrophy [56-58].

In oncology TSPO has several relevant potential functions, including contributing to the regulation of cellular proliferation, immuno-modulation and apoptosis [47, 59-61]. Expression of TSPO is low in the human brain but up regulation in glial and ependymal cells occurs in response to brain injury and microglial activation [51, 62]. The majority of neuroimaging studies to date have therefore focussed upon the potential role of TSPO ligands to delineate and quantify neuroinflammation [63, 64]. In addition to enabling study of the immune response to brain tumours, glioma cells of differing types and from a number of widely used glioma cell lines are known to directly express TSPO[65, 66]. Expression levels in human astrocytoma specimens have been shown to correlate with tumour grade [67-69] in addition to correlating with markers of cellular proliferation [68] and apoptosis [69]. Similar prognostic relevance of TSPO expression levels has also been demonstrated for other human neoplasms including colorectal [70-72], oesophageal [73], breast [74-76], hepatic [77] and prostate cancer [78]. A corresponding pattern is seen with the study of

experimental glioma cell lines, amongst commonly studied cell lines higher proliferation rates and other features of in vitro tumourigenicity were seen in cells with higher TSPO expression.

In vivo human studies have confirmed that the density of TSPO is significantly greater in higher grade tumours, suggesting that imaging of TSPO expression may be used to differentiate HGGs from LGGs [65, 79]. This was further demonstrated in a recent study from our group which also identified the origin of the signal seen on [11C]-PK11195PET to be TSPO expression on tumour cells themselves rather than reflecting the host immune response [65]. Together these findings suggest a potential role of the TSPO receptor in tumour progression and prognostication.

[^{11}C]-(R)-PK11195 is the 'prototype' PET TSPO ligand and although several second generation probes have been proposed to have specific advantages in the imaging of neuroinflammation, there is little evidence upon which to select another tracer for the study of gliomas [63]. Our research group has previously used [11C]-PK11195 in this context where it has the advantage of relatively low cost and a short half-life which helps to reduce the total radiation dose. There is also a well-established pipeline for data analysis and quantification with [11C](R)-PK11195 including a library of scans from normal controls and non-glioma patients for comparison. This is complimented by imaging on the High Resolution Research Tomograph (HRRT) which is a dedicated PET brain scanner that offers a spatial resolution adequate to quantify uptake in relatively small areas within the tumour. This capability is unique to only a few centres worldwide. This, combined with the large patient cohort in Greater Manchester, made it feasible to conduct this work at Salford Royal NHS Foundation Trust (SRFT). Should this and future work demonstrate the ability of PET imaging to detect transformation and invasion areas, there may be the potential to further develop not only diagnostic but also therapeutic and prognostic biomarkers.

2.4 Methionine PET Imaging in Glioma

The low uptake in the normal brain and increased uptake in brain tumours, including non-enhancing gliomas, makes radio-labelled amino acid tracers an appealing approach of imaging in neuro-oncology. [11C]-methionine is perhaps the best-evidenced tracer and has been applied to the differential diagnosis [80], biopsy

targeting [81], resection [82] and radiotherapy planning [83] in gliomas. The clinical utility of [11C]-methionine PET (MetPET) is limited by the short half-life of the tracer, which necessitates on-site production. However, amino acid tracers with more practicable half-lives such as [18F]-fluoroethyl-tyrosine (FET) [84] and [18F]-fluoro-DOPA [85] are increasingly available and yield similar results [86].

Methionine is transported across the BBB via the large amino acid transporters (LAT), predominantly LAT1 but also LAT2 in a lesser degree [87-89]. An increase in methionine uptake has been demonstrated with increasing tumour grade [80] which is robust within gliomas of a specific histological type [90]. The relatively high sensitivity and specificity of the technique in delineating tumour extent [91] combined with correlation between peak uptake and histological grade makes MetPET well suited to tumour surveillance and evaluation of treatment response [92]. Methionine uptake has also been shown to correlate with microvessel density [93] and tumour cell density [94] on previous histopathological studies in addition to correlating with tumour cell proliferative activity [94, 95].

Amino acid PET has proven diagnostic utility for guiding stereotactic biopsy [81, 85, 96, 97] and a similar role has been proposed for perfusion-weighted MR imaging [33], which has the potential to be much more readily available. A better understanding of the relationship between the findings obtained by these different approaches would enable diagnostic strategies to be rationalized, particularly with respect to the role of amino acid PET given its cost and relative lack of availability. Intra-tumoural variability in the extent to which the results different modalities correlate may also yield further insights into tumour behaviour in vivo. However, the current evidence base describing multi-modal investigation of individual tumours with PET and extended MRI is limited, in part due to the technical challenges in correlating results from different modalities with differing spatial and statistical characteristics. The increasing availability of high field strength MRI and improved spatial resolution in PET imaging also allows more detailed study of the intra-tumoural distribution of imaging changes and for the location of high-signal areas, as indicators of tumour regions with the “highest malignancy” and as potential biopsy targets.

2.5 Research Questions

This research project is an imaging study with advanced MR and PET imaging focusing on the patterns of glioma transformation and disease progression. The study was conducted in two parallel stages.

The first stage investigated TSPO PET imaging as a potential tracer for early identification of transformation in LGG and tumour recurrence in HGG. From previous work, a correlation of histological grading with TSPO uptake has already been described. This project further explored the correlation of increased TSPO with perfusion and diffusion metrics. Research questions and tested hypotheses generated from this stage were as follows:

- How will the correlation between increased uptake and grading be affected by the new implementation of molecular markers in the WHO classification. Which is the most reliable imaging marker in oligodendrogliomas?
- Why the oligodendrogliomas have increased uptake compared to the similar grade astrocytomas? The current hypothesis is that the prominent vasculature in oligodendrogliomas accounts for the increased endothelial binding of TSPO therefore the increased tracer uptake. If this hypothesis is true we would expect a similar co-localisation of increased tracer uptake and increased rCBV.
- Can the TSPO PET imaging provide a reliable tool for targeting biopsies in LGG and at what threshold would be considered safe to biopsy? In multiple amino acid tracer studies the conventional threshold 1.4 of tumour-to-normal ratio has been largely accepted as a good discriminator for tumour versus normal brain area. In TSPO PET imaging studies yet there is no description of a reference value.
- Can TSPO or MR diffusion metrics predict the site of tumour transformation in LGG? The hypothesis is that visible increased uptake of TSPO PET ligands can precede structural MR imaging changes in disease progression.
- Is the rest of the brain affected by the glioma? The hypothesis is that primary brain tumours are not just a focal disease but involve the whole brain due to an inflammatory response..

The second stage of this project evaluated the role of Methionine in defining the tumour extent and the correlation between uptake and MR perfusion and diffusion metrics which are the most easily accessible in clinical setting. The research questions that arose from this stage were:

- How does methionine uptake correlate to histopathological findings and perfusion/diffusion parameters?
- Does dynamic methionine PET scan provide additional information valuable for grading and prognostication?

Blank page

Chapter 3 – Methodology

3.1 Patient recruitment

The subjects for this study were recruited during an 11 year period (2008 – 2019) through six different non-randomised unblinded prospective studies approved by the relevant Ethics Committees including the University of Manchester Ethics Committee:

- TSPO PET imaging in Glioma (West Manchester Local Research Ethics Committee – reference 14/NW/0429)
- Imaging of the 18kDa Translocator Protein in Primary and Recurrent High-Grade Glioma using PET (Greater Manchester South Ethics Committee – reference 16/NW/0548).
- Translocator Protein Expression in Transforming Gliomas (Central Manchester – reference 14/NW/0071)
- TSPO PET imaging in predicting Vestibular Schwannoma growth (Salford and Trafford Local Research Ethics Committee - reference 07/Q1404/50)
- Evaluation of TSPO expression by PET imaging in healthy subjects (Wrightington, Wigan and Leigh Local Research Ethics Committee – reference 109/H1014/41)
- Utility of [11C]-(R)-PK11195 PET to assess metastatic disease in the brain (West Manchester – reference 14/NW/1255)

Permission to administer radioisotopes was granted for all the studies by the Administration of Radioactive Substances Advisory Committee (ARSAC) of the Department of Health, UK.

Patients with evidence of brain tumours on diagnostic MRI were identified at the weekly Neuro-Oncology Multidisciplinary Meeting (MDT) at Salford Royal NHS Foundation Trust and recruited during their clinic appointments with the treating Consultant.

Only patients in whom surgical intervention (tumour biopsy and/or resection) was considered were approached to ensure that a contemporary histological diagnosis was available in the majority of cases. However, this criterion was not met at all times, since the final decision on surgical intervention could not be made until all

diagnostic investigations were completed. The specific inclusion and exclusion criteria for the studies were:

Inclusion Criteria:

1) Age greater than 18 years and less than 80 years;

* Children are excluded primarily due to constraints on the dose of injected radiotracer. Patients over 80-year-old are more prone to co-morbid conditions that might trigger neuroinflammation, and/or increased microglia activation in the brain due to aging effects [98].

2) MRI evidence of space occupying lesion with the appearance likely to be a primary glioma, secondary tumour (for the "TSPO in Brain Metastasis" study) or Vestibular Schwannoma (for the "TSPO in Vestibular Schwannoma" study)

3) Karnofsky performance score ≥ 70 and WHO performance status score ≤ 2;

* Patients who required in-patient care, or were systemically unwell such that taking part would become an increased burden to them were excluded.

4) Life expectancy longer than 3 months;

5) Ability to give fully informed consent and comply with the protocol;

6) Using effective contraception if of childbearing potential.

* Due to the radiation dose involved, female participants were required to demonstrate that they were not pregnant

Exclusion Criteria:

1) Co-morbid conditions or current status likely to interfere with the capacity to comply with assessments, imaging (including lying flat supine for up to 70 min), biopsy and/or treatment;

2) Specific contra-indication to MRI (e.g. pacemaker or a ferromagnetic implant such as intracranial aneurysm clip, and claustrophobia) or failure to tolerate diagnostic MRI scan previously;

3) Known additional malignant tumour or evidence of additional significant intracranial lesion (this exclusion criteria was only for the glioma and vestibular schwannoma studies);

* Additional malignant tumour increases the risk of the presence of intracranial metastases; additional intracranial lesion would lead to neuroinflammatory responses, especially microglial activation.

4) Patients who are taking minocycline (in the recent 3 months prior to the PET scan) and/or corticosteroids (corticosteroids should be discontinued for at least 2 weeks before the PET scan, unless indicated otherwise by individual pharmacokinetics);

* Minocycline and corticosteroids have been shown to interfere with microglial activation in the brain (potential suppressive effects)[99-102].

5) Pregnant or lactating women;

6) Sexually active female patients who are not employing adequate contraception (pregnancy tests were performed in all women of childbearing potential; this population were also strongly advised to avoid pregnancy during the study);

7) Severe uncontrolled systemic diseases.

In total 119 patients were recruited and completed the relevant scanning protocol, in more detail:

- 27 patients recruited through “TSPO and Methionine PET Imaging in HGG” study
- 23 patient recruited through “TSPO in Glioma” study
- 21 patients recruited through “TSPO in Transforming LGG” study
- 21 patients recruited through “Methionine PET Imaging in LGG” study
- 19 patients recruited through “ TSPO in Vestibular Schwannoma” study
- 8 patients recruited through “TSPO in Brain Metastasis” study

Information sheets about the study were provided to all study subjects. They were given a minimum of 24 hours to make a decision about participation in the study. All participants gave informed consent to the imaging investigations, the image-guided

biopsies, and the extended analysis of tissue specimens. Participants' information was recorded following recruitment including the identifier number, hospital number, date of birth, age, gender, handedness, contact details, brief clinical history, medications and follow up.

To determine the [11C]-(*R*)PK11195 uptake in normal brain structures, 19 healthy volunteers were also scanned for comparison. Control subjects underwent medical history taking, physical and neurological examinations. None of them reported any significant somatic or psychiatric illnesses; all had normal examination findings, and showed no significant structural lesions on anatomical MRI as judged by an experienced neuroradiologist (AJ/ID).

3.2 MR Imaging

All participants underwent a standardized brain tumour protocol performed on a Philips Achieva 3.0 or 1.5 Tesla scanners (Philips Healthcare, The Netherlands). MRI scans were performed within a month time from the PET scan, in most of the cases performed on the same day.

Anatomical sequences included an axial T1 inversion recovery (TI=1150ms, pixel size(PS)=0.94x0.94mm, slice thickness (ST)=1.8mm on the 3T scanner and TI=1000ms, PS=1.19x1.19mm, ST=1.25mm on the 1.5T scanner), high resolution axial T2 (3T acquisition PS=0.26x0.26mm, ST=3.0mm and 1.5T PS=0.45x0.45mm, ST=6mm) and coronal FLAIR (3T acquisition PS=0.45x0.45mm, ST=3.0mm and 1.5T PS=1.07x1.07mm, ST=1.25mm).

Diffusion tensor images (DTI) were acquired with 6 non-collinear gradient directions on both scanners (B=0 and 1000 s/mm2, PS=1.8x1.8mm, ST=5mm on the 3T scanner and PS=1.8x1.8mm, ST=1.8mm on the 1.5T respectively).

The MR protocol used in this study included two different methods of acquisition; T2*-dynamic susceptibility contrast imaging sequence (2D T2*W-field echo-plannar multi-shot sequence which relies on first pass drop in signal), as well as a T1-dynamic contrast enhancement sequence (that measures transfer of contrast from blood into extravascular, extracellular space through multiple T1-weighted high spatial and high temporal resolution scans). Due to the high analytic demand of the T1-weighted

dynamic images and the versatility of T2*W DSC imaging used also in clinical setting, only the last one was used in the next 3 experimental chapters. To increase the accuracy of rCBV measurements and derived parametric maps from T2*W DSC acquisition and avoid artefacts from blood-brain barrier (BBB) disruption, resulting in contrast leakage with T2*-weighted imaging residual effects, the T2*DSC sequence was performed at the end of the protocol after an initial dose of contrast given for the T1W dynamic images and post-contrast brainlab sequence was acquired (for intraoperative navigation). This preload dosing, together with baseline subtraction during image processing of T2*W images have been proposed as simple methods to minimize and correct for T1-weighted leakage and T2/T2*WI residual effects [103].

Both perfusion and permeability sequences were acquired as an oblique sagittal block incorporating the tumour along with the ipsilateral middle cerebral and internal carotid arteries. This acquisition is planned to optimize temporal and spatial resolution whilst facilitating input function calculation. Acquisition of T2* weighted data was carried out immediately after completion of T1 weighted dynamic data acquisition, with the time delay set at a fixed duration, so that pre-enhancement would minimize residual relaxitivity effects. T2* weighted dynamic contrast-enhanced data were acquired similarly on either 3T or 1.5T scanners using a multislice 2D T2*W-FEEPI (field echo-EPI) multi-shot sequence (3T acquisition TR 440ms, TE 30ms, PS=1.8x1.8mm, ST=3.5mm, and 1.5T acquisition TR 16ms, TE 24ms, PS=1.8x1.8mm, ST=3.5mm). The dynamic contrast-enhanced series consisted of 52 scans at a flip angle of 35° and a temporal spacing of 1.8 s. Gadolinium-based contrast agent (Gd-DTPA-BMA; Omniscan2, Amersham Health AS, Oslo, Norway) was injected as a bolus over 4 s at a dose of 0.1 mmol/kg of body weight after the fifth dynamic scan. Pre- and post-contrast T1 images were acquired both to correspond as much possible with the perfusion imaging and as a volumetric acquisition (3T: PS=0.94x0.94mm, ST=1.0mm and 1.5T PS=1.0x1.0mm, ST=1.25mm).

3.3 TSPO PET Imaging

3.3.1 [11C]-(*R*)PK11195 production

The radiotracer [11C]-(*R*)-PK11195 (1-(2-chlorophenyl)-N-methyl-N-(1-methylpropyl)-3-isoquinoline carboxamide) was produced on-site at the Wolfson Molecular Imaging Centre (WMIC). It was synthesised by reaction of [11C]methyliodide with the precursor N-Desmethyl-(*R*)PK11195 adopting the previously described method [104, 105]. The reference standard for (*R*)PK11195 and the precursor N-Desmethyl-(*R*)PK11195 were obtained from ABX Advanced Biochemical Compounds (Radeberg, Germany). Both captive solvent radiosynthesis and quality control were performed to ensure that the product is free of radiolabelled impurity originating from dechlorination of [11C]-(*R*)PK11195 [106, 107].

3.3.2 The High Resolution Research Tomograph (HRRT)

PET scans were performed at the WMIC on a dedicated PET brain scanner: the High Resolution Research Tomograph (HRRT, Siemens/CTI, Knoxville, TE, USA). It provides an intrinsic spatial resolution of approximately 2.5 mm throughout the field of view (FOV, axial: 252mm, transaxial: 312mm), which is unprecedented by any other clinical PET scanners currently available [108, 109]. This high resolution is mainly achieved by its unique design of eight planar detector heads arranged in an octagon and equipped with dual-layer LSO/LYSO scintillator crystals for the determination of depth of interaction (DOI, the depth at which a gamma ray strikes the detector)[108]. The DOI information helps in reducing the so-called parallax errors and can be applied during the image reconstruction to reduce the degradation of spatial resolution, particularly near the edge of the field of view (FOV). A scintillator absorbs the high energy gamma rays produced by positron annihilation and fluoresces to yield a measurable response. Using LSO (lutetium oxyorthosilicate) as the first layer of scintillators allows higher light output and faster decay time than previously employed counterparts [110], while the second layer of LYSO (lutetiumyttrium oxyorthosilicate) produces a similar light yield but a slightly longer decay time [108]. Such difference in light decay of the two layers allows the

measurement of DOI and distinction of events between the first and second layer. The DOI and location information obtained by this system contributes to the increased resolution as well as similar sensitivity compared with the best detector system currently available.

The improvement in resolution and corresponding reduction in partial volume effects allow small structures within the brain to be imaged by PET in unparalleled detail[111]. The HRRT has great potential to investigate functional changes not only within gliomas of heterogeneous nature but also in the surrounding brain tissue, and provides a useful modality to evaluate the response of the tumours to therapeutic interventions.

3.3.3 Image acquisition

Participants were allowed to eat and drink normally on the day of scanning. As [11C]-(*R*)PK11195 is a ligand for the TSPO (peripheral benzodiazepine receptor), patients must not have been taking benzodiazepines with a long half-life that would interfere with the [11C]-(*R*)PK11195 binding. Patients if on any benzodiazepines were asked to stop taking them for at least 3 days prior to the PET scanning. After the venous cannulation, subjects were positioned in the scanner with a custom head holder to support the head and straps were placed across the forehead and chin to deter head movement.

A 7-minute transmission scan using a 137Caesium (137Cs) point source was acquired for subsequent attenuation and scatter correction. Shortly after the start of the emission scan, [11C]-(*R*)PK11195 was injected intravenously by hand as a slow bolus (10ml) over approximately 15 seconds and flushed with 0.9% saline (10ml) at the same rate. The comparisons of injected dose, specific radioactivity, injected mass of stable [11C]-(*R*)PK11195 and radiochemical purity between the patients and controls are summarized in Table 3.1. Emission data were then acquired for 60 minutes post injection in list mode and histogrammed post acquisition. 18 time frames of increasing length were generated: one background frame of variable length prior to the injection, then one 15s frame, one 5s frame, one 10s frame, one 30s frame, four 60s frames, seven 300s frames and two 600s frames. Subjects' head positioning was

recorded (using laser beams) and monitored (via a camera) throughout the scan and corrected immediately, when necessary.

	Controls N=19	*Glioma N=66*	*Metastasis N=8*	*VS N=19*
Age (years)	47 ± 18	47 ± 16	63 ± 8	57 ± 16
Injected Dose (MBq)	544 ± 126	623 ± 132	663 ± 89	699 ± 78
Specific Activity (GBq/µmol)	106 ± 39	159 ± 62	270 ± 79	228 ± 76
Injected Mass of Stable PK11195 (µg)	2.2 ± 1.42	1.6 ± 0.71	1.0 ± 0.35	1.2 ± 0.54
Radiochemical Purity (%)	98.3	98.6	99.14	99.08

Table 3.1 Comparison of age and injected radioactivity details for [11C]-(R)-PK11195 in different groups.

3.4 Methionine PET Imaging

PET scans were performed on an ECAT High Resolution Research Tomograph (HRRT) (CTI / Siemens Molecular Imaging Inc., TN, USA). Subjects were fasted for a minimum of six hours prior to the scan, which was performed in a quiet room with dimmed lighting and a regulated ambient temperature. A 6.5 minute transmission scan was performed for attenuation correction prior to injection of the tracer using a 137Caesium transmission point source. A target dose of 740MBq of [11C]-methionine was injected manually over 20 seconds followed immediately by a 10ml 0.9% saline flush injected at the same rate. Emission data was acquired for 40 minutes from injection and reconstructed to give a static frame from 20-40 minutes post-injection. Image reconstruction was performed using an iterative algorithm, Ordinary Poisson Ordered-Subset Expectation Maximization (OP-OSEM) (12 iterations, 16 subsets)[112], with corrections applied for random events [113], attenuation [114] and scatter [115]. Images were calibrated against a phantom with known radioactivity and smoothed with a 2.5mm FWHM Gaussian filter corresponding to the resolution of the scanner.

3.5 Data Analysis

Image processing followed the four parallel steps represented on the flowchart in Figure 3.1 and further explained in the respective subsections.

PET and MRI scans were co-registered using the summed PET image and the T1-weighted IR or the post-contrast MR image in a 2-step rigid-body co-registration with

the software package FSL version 3.3 (FMRIB Software Library, Oxford, UK). The summed PET image was obtained as the sum of frames 2 to 18 in both [11C]Methionine and [11C]-(R)PK11195 PET scans; this summation image contains blood flow dependent signal and provides good anatomic detail for accurate co-registration [116]. Initially the images were co-registered from low (PET) to high (MR) resolution, and then the inverse transformation matrix was applied to co-register the high resolution MR sequences to the PET space. The quality of co-registration was visually inspected for accurate anatomical co-localisation.

For image-guided biopsy, PET images were registered to MR images to facilitate such clinical application as the latter was the modality used in the operation theatre; for quantitative analysis, MR images were registered to PET images in order to preserve the original PET data.

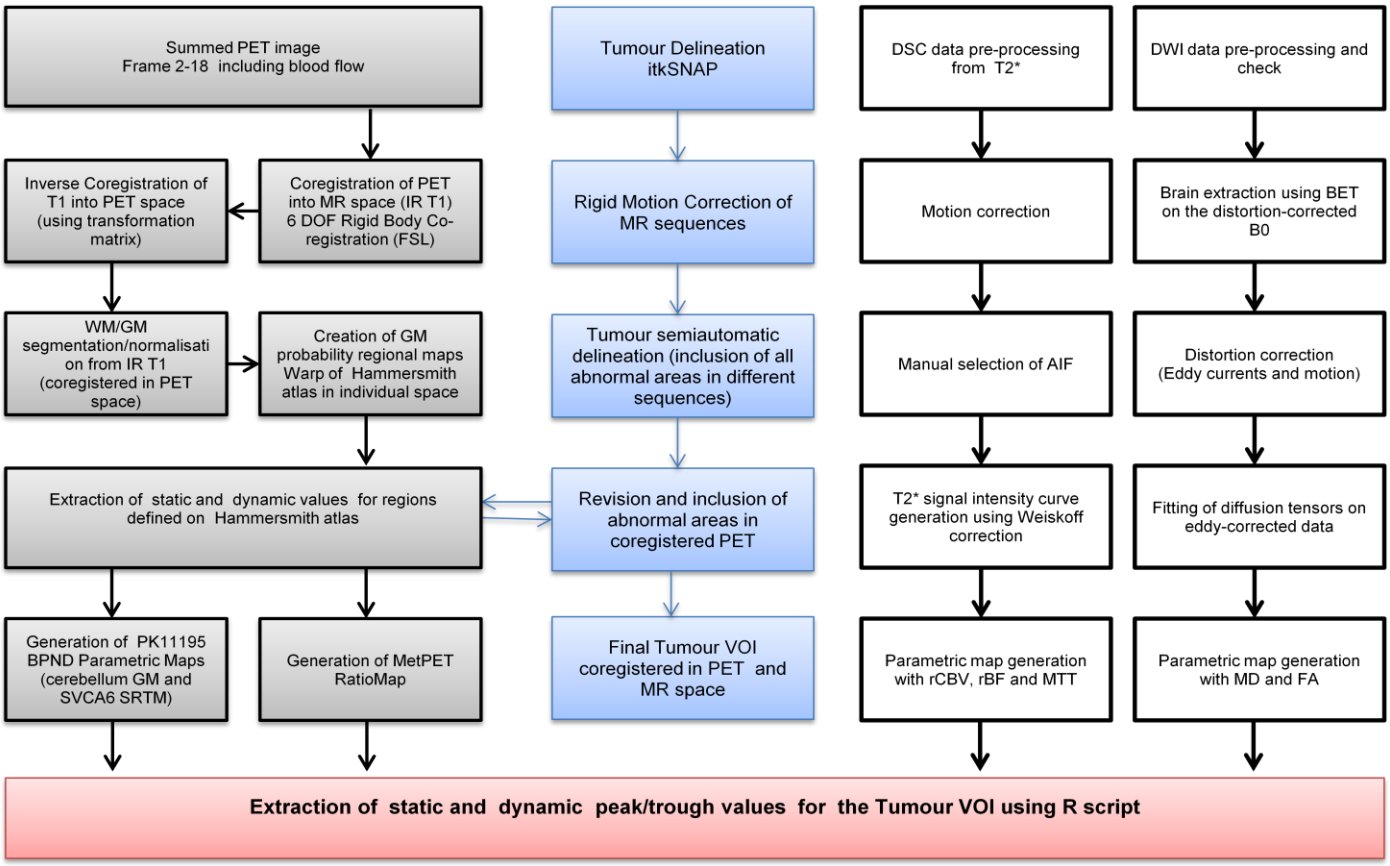

Figure 3.1 Flowchart representing the basic steps for image processing. (from left to right) In grey; boxes processing of PET images and registration of inversed recovery T1 images, followed by WM/GM segmentation and exctraction of input function from cerebellum GM to construct BPND parametric maps. In blue; tumour delineation by including all abnormal areas defined on MR and PET. In white; MR perfusion and diffusion processing. DOF=Degree of Freedom, IR=Inverse Recovery, WM=White Matter, GM=Grey Matter, SVCA6=Supervised Cluster Analysis using 6 predefined classes, VOI=volume of interest, AIF=arterial input function, rCBV=relative Cerebral Blood Volume, rBF=relative Blood Flow, MTT=Mean Transition Time, MD=Mean Diffusivity, FA=Fractional Anisotropy, BET=Brain extraction tool

3.5.1 [11C]-(*R*)PK11195 PET Image Processing

Parametric maps demonstrating [11C]-(R)PK11195 binding potentials (BPND) as the ratio of specifically bound tracer over non-displaceable tracer in tissue at equilibrium were generated [117]. These were calculated using a simplified reference tissue model (SRTM) with two different 'pseudoreference' tissue input functions: 1) a cluster of grey matter (GM) voxels extracted using a supervised clustering algorithm [118]; 2) atlas defined cerebellar GM as a large and relatively homogeneous structure distant from the tumours [119]. After confirming that no significant difference was introduced between the reference tissue approaches, cerebellar GM was selected as the preferred method for the remainder of the analysis due to its proven robustness[119].

The tumour VOI for each subject was projected onto the BPND parametric map to enable the region of peak tracer uptake within the FLAIR defined tumour volume to be identified and sampled. Mean BPND for a spherical sampling VOI with a 7mm diameter (179 voxels) centered on the voxel of interest was calculated for every voxel in the final tumour VOI using an automated analysis performed in R statistics (R Foundation for Statistical Computing, Vienna, Austria)(Figure 3.1). The 7mm diameter sphere, defined as an approximate biopsy target, searched within the final tumour VOI for the peak region and automatically generated a VOI in the PET space. Locations in which the sampling VOI extended beyond tumour region or which contained missing values were excluded. Maximum binding potential (BPNDmax) was defined as the mean of the sampling VOI which yielded the greatest value and was recorded along with the location of the center of the VOI.

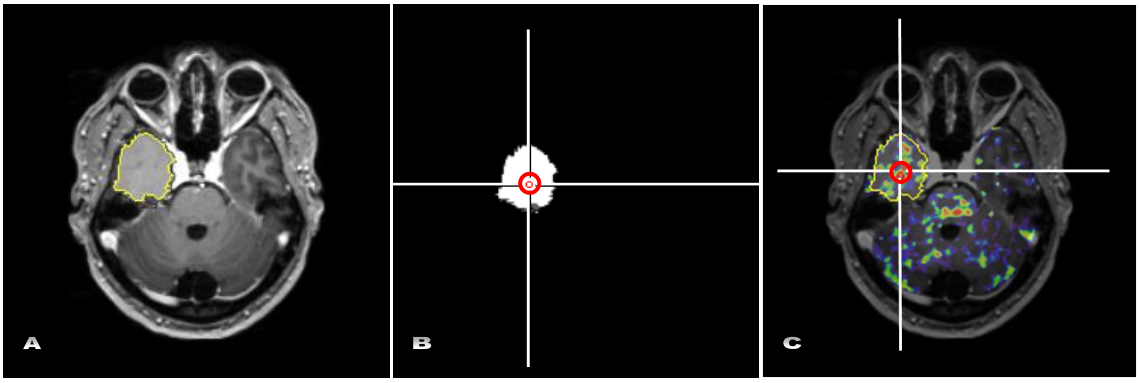

Figure 3.2 A. Post-contrast T1 with final tumour VOI delineated in FLAIR (in yellow); B. Representation of the 7mm sphere (in red) defined in R which automatically searches for the highest uptake region within the tumour mask registered into the PET space; C. Fused PET/MR image with the final visual representation of the 7mm sphere VOI (in red) automatically generated in peak region of tracer uptake within the defined tumour mask (in yellow) on the coregistered PET, areas in red represent the highest uptake.

All data were expressed as mean ± one SD. [11C]-(R)PK11195 uptake parameters were compared between grade II and grade III gliomas according to their histological type using 2-tailed t-test. A threshold value of BPNDmax >1.4 was evaluated as a potential discriminator for low grade and anaplastic glioma and selected on the optimal Youden index (Figure 3.2) based on the highest sensitivity and specificity. The Youden index is a way of summarising the performance of a diagnostic test. Its value ranges from 0 through 1, and has a zero value when a diagnostic test gives the same proportion of positive results for groups with and without the disease, meaning the test is not useful. A value of 1 indicates that there are no false positives or false negatives, i.e. the test is perfect.

BPND parametric images generated using different input functions were compared voxel-by-voxel using Bland–Altman plots [120] with local regression [121] and regional tumour VOI BPND values derived from the two input functions were compared using Pitman's test of difference in variance [122]. A probability of $p<0.05$ was considered statistically significant.

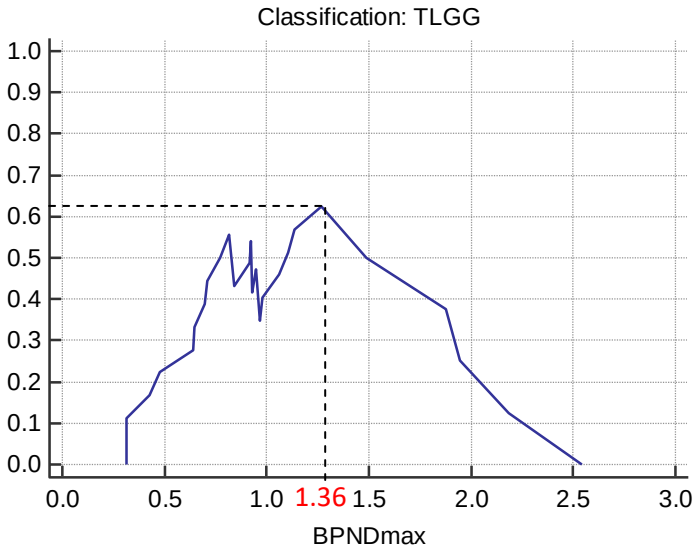

Figure 3.3 Definining optimal threshold value of 1.4 based on the highest Youden index *J = max (sensitivity + specificity - 1). X-axis expressing the Youden index based on discrimination of high vs. low grade gliomas. Y-axis representing the BPNDmax.*

3.5.2 [^{11}C]-Methionine PET Image Processing

Individual PET and MRI sequences were co-registered to the T1 Inversion Recovery data, re-sliced to give isotropic 1mm^3 voxels, using a hierarchical rigid-body registration algorithm [116] implemented in Vinci version 2.53 (Max-Planck Institute for Neurological Research, Cologne, Germany). For the DTI and DSC data, B0 and pre-injection T2* images respectively were co-registered using an initial manual pre-fitting followed by a constrained 2-level rigid-body registration process with the resulting transformations subsequently applied to the derived parametric images. Co-registered anatomical images were segmented using the "New Segment" tool [123] in Statistical Parametric Mapping version 8 (SPM, Wellcome Trust Centre for Neuroimaging, University College London, UK). White and grey matter masks for intensity normalization were prepared using a threshold value of 95%. A brain mask was also derived from summed white and grey matter segments with a low threshold (10%) to ensure that the tumour was not excluded from this mask.

3.5.3 Perfusion-Weighted MRI

Processing of the DSC data was performed using both Phillips proprietary software for treatment planning and using MIStar (Apollo Medical Imaging Technology Pty. Ltd., Melbourne, Australia) for further analysis. The model employed was a Singular Value Decomposition Deconvolution with Weiskoff correction for contrast extravasation [124]. A manually defined input function was utilized, defined as 2-5 voxels from 1-3 contiguous slices through a transverse section of the middle cerebral artery ipsilateral to the tumour being studied. Voxels adjacent to and not within the artery were selected to optimize measurement of the susceptibility effect [125]. T2* signal intensity curve was transformed into contrast concentration time course data which was fitted by gamma-variate fitting. CBV maps were calculated by numerical integration of the area under the concentration time curve from the arrival to recirculation of the contrast bolus [126]. The CBV map was co-registered to the T1-weighted post-contrast MRI that had already been registered to the summed PET image. Tumour blood volume was quantified using rCBV (CBV relative to the normal appearing white matter in the controlateral cerebral hemisphere). For this process, an elliptical ROI was placed within the controlateral frontal white matter on the CBV map guided by overlaid T1-weighted post-contrast image. An rCBV map was derived by dividing the CBV map by the mean value of the controlateral white matter ROI. The whole tumour ROI was further edited to exclude areas of large vessels, when present, and projected onto the rCBV map to sample the mean rCBV value of the entire tumour. Small ROIs were also drawn in areas of increased rCBV within the tumour (avoiding blood vessels, calcification and haemorrhage) to extract the maximal rCBV values from the 'hottest' voxel in those ROIs.

3.5.4 Diffusion-Weighted MRI

DTI data was processed using FDT (FMRIB's Diffusion Toolbox) from FSL version 3.3 [127]. Eddy current and motion correction was performed prior to fitting of the diffusion tensors. A binary brain mask image was initially generated removing scalp and soft tissue and was applied to the diffusion data. Revised fitting of diffusion

tensors was performed on eddy-corrected, calculating the tensor for each point within the brain mask generated. Mean Diffusivity and Fractional Anisotropy parametric maps generated were co-registered to the PET images by applying the transformation file from B0 rigid co-registration to PET summed images.

3.5.5 Tumour and ROI definitions

Individual MRI scans were co-registered with the corresponding summed PET images utilising a hierarchical rigid body co-registration algorithm [116]. The quality of co-registration was visually inspected for accurate anatomical co-localisation.

In vestibular schwannomas, tumour ROIs were manually delineated on the co-registered T1-weighted post-contrast images with care in avoiding partial volume effects from nearby structures or surrounding CSF [128].

Tumour volumes in low grade gliomas (including visible oedema, if present) were delineated semi-automatically initially on FLAIR images using thresholding and active contour tool in itk-SNAP [129] (Figure 3.3). Tumour masks generated were further confirmed against the T1-weighted post-contrast sequences to include any abnormal areas [31]. In gliomas of higher grade and metastatic lesions instead, tumours were delineated initially on T1-weighted post-contrast images and any abnormal areas on T2-weighted and [^{11}C]-Methionine PET images were included in the tumour masks generated (Figure 3.4). All patient scans were reviewed by an expert neuro-radiologist and classified into two groups according to their contrast-enhancement on post-gadolinium scans: no enhancement and subtle or patchy enhancement.

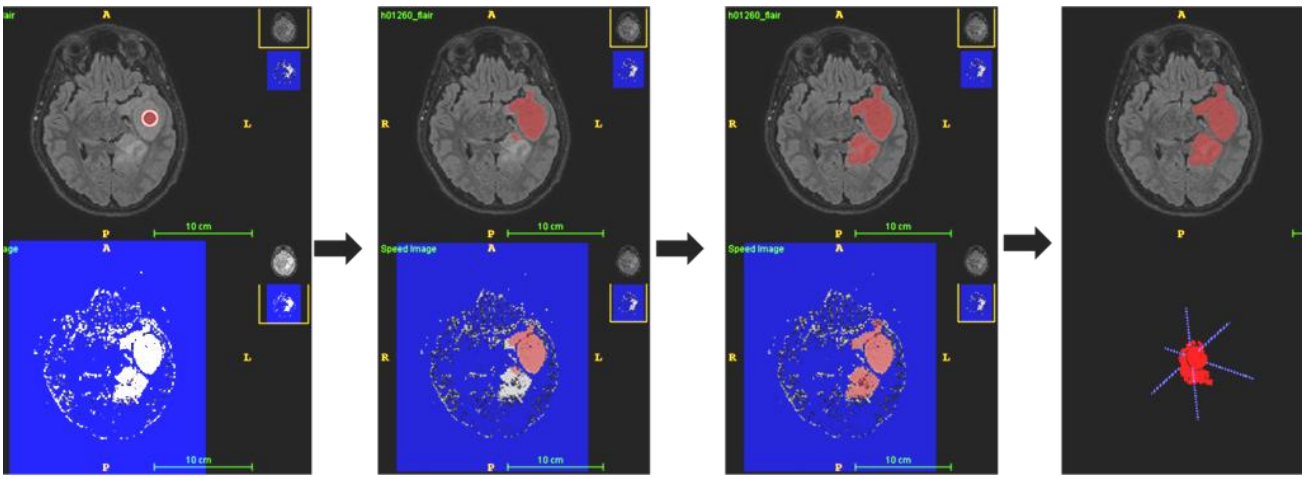

Figure 3.4 Initial semi-automatic delineation of tumours using itkSNAP algorithm for contour evolution. Tumour classes defined on the FLAIR sequence and a probability map (cut section in blue) automatically was generated. A seeding point (red sphere on the left image) placed manually on the tumour. Algorithm-run evolution and expansion of the tumour VOI (area expanding in red) until whole tumour included satisfactorily and final generation of a 3D tumour VOI ready for visual inspection.

Disease progression was defined according to the RANO criteria [130] following expert review by neuro-radiologist and correlation with the clinical status at the neuro-oncology MDT. Peak uptake was determined using the mean of a spherical VOI with a 7mm diameter (179 voxels), every voxel in the final tumour VOI was evaluated to determine which yielded the peak value using an automated analysis performed in R statistics (R Foundation for Statistical Computing, Vienna, Austria). Trough values were also calculated for the DTI metrics. MetPET uptake values are presented as the ratio to normal appearing cortex. DSC values are presented as the ratio to normal appearing white matter defined as the mean of the white matter segment after exclusion of the tumour VOI as data for mirrored controlateral regions was not consistently available. Fractional anisotropy (FA) and mean diffusivity (MD) are presented as the calculated values.

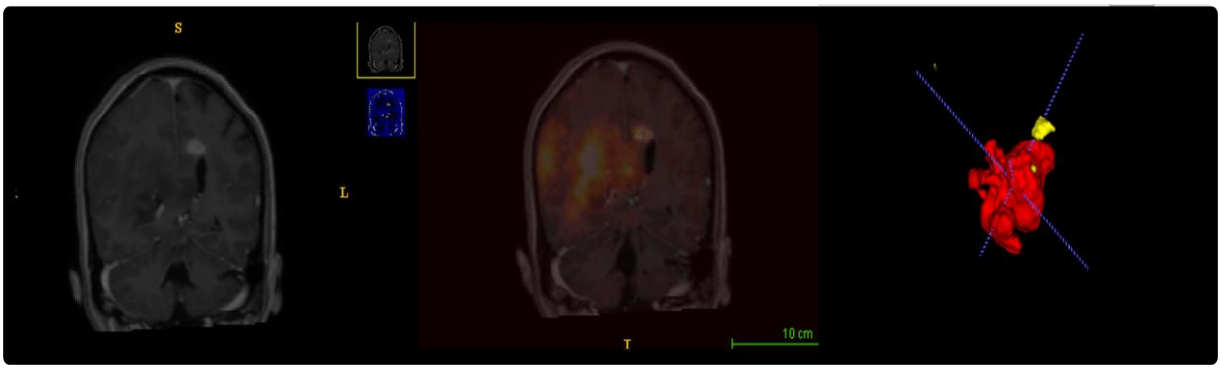

Figure 3.5 Delineation of tumour on post-contrast T1 showing only a minor area of enhancement, addition of PET abnormal uptake area within the tumour mask and 3D configuration.

3.6 Image-guided biopsies

Regions of raised rCBV or [11C]-(R)PK11195 uptake were selected as targets for image guided biopsies. Targeted biopsies were taken in 23 subjects followed by tumour debulking and in 3 cases of suspected transforming gliomas, only biopsies were performed. Biopsies were only taken from regions confirmed radiologically to represent tumour on anatomical MRI sequences and planned for subsequent resection in debulking cases. PET and MRI defined targets were transferred to the intra-operative neuronavigation system using anatomical landmarks and multimodal intraoperative display (Figure 3.5). Burr-hole / trephine biopsy was performed with neuronavigation guidance using BrainLAB or Stealth (Medtronic) systems. Patients undergoing subsequent tumour resection had open biopsies with samples taken immediately following dural opening using either standard tracked brain biopsy needle or using a biopsy rongeur under neuronavigation guidance. BrainLAB or Stealth co-ordinates for the location from which tissue samples were taken were recorded in the systems and together with the registration data were downloaded at the end of the procedure for translation back to the original data set.

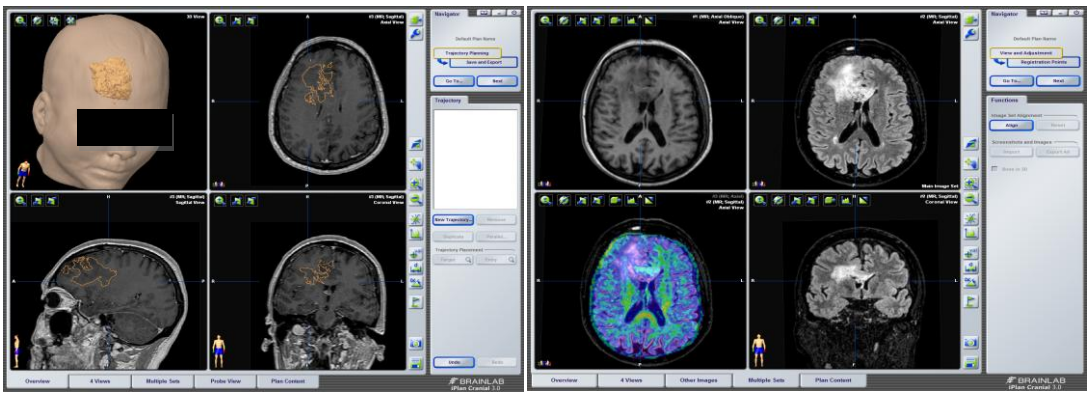

Figure 3.6 Example of multimodality imaging in surgical planning implementation on BrainLab. Pre and Post-Contrast T1 images in addition to FLAIR and fused PET.

3.7 Neuropathology assessment

Surgical specimens were fixed in 10% buffered formalin and paraffin embedded. The haematoxylin-eosin (HE) stained sections were reviewed by an experienced neuropathologist (F.R.) and diagnoses were made according to WHO criteria [131]. IDH-1 status and loss of heterozygosity of chromosomes 1p/19q assessed with immunohistochemistry (IHC) and genetic sequencing were used to inform type classification.

The extent of TSPO expression in neoplastic cells, vessels and microglial macrophages were assessed using peroxidase immunohistochemistry (IHC). This was performed using the Super Sensitive Polymer HRP IHC Detection System (BioGenex Laboratories, Inc. San Ramon, CA, USA) according to the manufacturer's protocol, with antibodies directed against TSPO (polyclonal goat anti-TSPO, dilution 1:750, GeneTex, Hamburg, Germany), $IDH1^{R132H}$ (Dianova, Hamburg, Germany monoclonal H09, 1:200) for IDH1 mutant tumour cells, the vascular marker CD31 (Dako CloneJC7QA Ref M0823, dilution 1:30) and macrophages / microglia (polyclonal rabbit anti-Iba1, dilution 1:500, WAKO, Neuss, Germany).

Distribution analysis of the TSPO in relation to CD31, IDH1 and Iba1 was performed using the Bitplane Imaris 3D/4D imaging software (Bitplane AG Zurich,Switzerland). (Full details of the procedure are reported in Appendix 1) [132]. In addition, we used double immunofluorescence (DIF) to quantitatively define TSPO expression in

neoplastic and microglial cells. TSPO and Iba1 immunostaining was evaluated using optical densitometry (OD) (Figure 4).

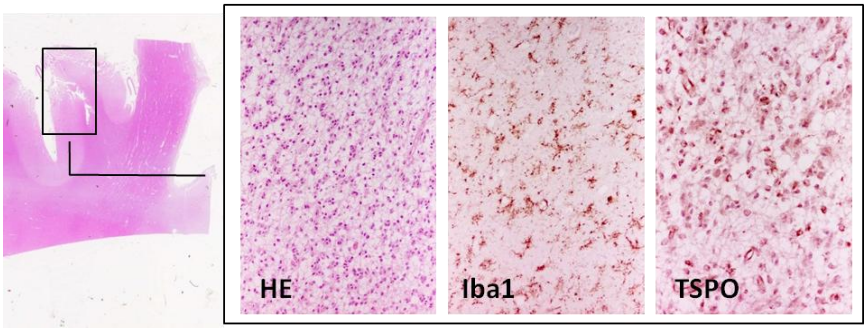

Figure 3.7 Different immunohistochemical staining used to define GAMMs (Iba1) and TSPO expressing cells in addition to conventional hematossilin-eosin (HE).

3.8 Role of the author in the Project

My role in the present work included project planning and governance, patient recruitment, data acquisition, image processing and data analysis.

The research concept was ideated by my supervisors Prof Alan Jackson , Mr David Coope, Dr Rainer Hinz and Prof Roncaroli, with some further subsequent small modifications during the data collection. In my initial period of PhD, I performed an extensive literature review on TSPO and other PET tracers used in glioma, in order to get an updated view ahead of our project. In the same time I started the ethical and the necessary R&D applications. During this period I also took ownership of the recruitment for two other TSPO PET imaging studies, "TSPO in TLGG" and "TSPO in VS". Along with the recruitment and preparation of all this paperwork, I gained hands-on experience in the analysis of a [^{11}C]-(*R*)PK11195 PET images as well as a novel 3-dimensional (3D) tissue histology technique, which led to two manuscripts I co-authored [128, 132]. At the same time, I worked on the PET and MRI scanning protocols for my study with the help of Mr Coope, Dr Hinz and rest of the team. All the essential approvals were obtained by the end of my first year, and with my completion of the remaining study governance requirements (e.g. research passport application), assisted by the project management team in WMIC, the study was finally launched and patient recruitment commenced on February 2017.

My role since then involved participant identification and recruitment, MRI and PET session booking, clinical supervision during scanning sessions, PET image processing,

analysis, and result presentation in the multi-disciplinary team meeting as well as to the neurosurgical team in the operation theatre. I attended the weekly neuro-oncology multi-disciplinary team meeting at Salford Royal Hospital for identification of suitable patients. I approached the patients mainly by joining the clinic of the treating consultants for clinical interview and consenting. Once verbal consent was obtained from the patients, I scheduled MRI and PET appointments as well as arranged the necessary logistics. Written consent was then obtained when the patients came for their first research MRI scan. I co-supervised the scanning and cannulated the patient, injected the contrast agent and radiotracer, and provided clinical cover. I then analysed the imaging data, worked out appropriate targets for the tumour biopsy, and presented them in the multi-disciplinary team meeting. With the help of Dr Coope, the biopsy targets were transferred to the neuronavigation system in the theatre, where I also presented for the operation to ensure correct tissue sampling and handling, and to record the biopsy locations. Subsequent histopathological assessment of specimens for the present study was done under the supervision of Professor Roncaroli.

During the second year of my PhD, a malfunctioning of the HRRT caused all PET scanning to be suspended until it was repaired, a period which lasted almost 8 months. During this time, I presented the preliminary findings in national and international conferences.

Once patient recruitment was resumed, I submitted ethical amendments to facilitate the recruitment and to broaden the study cohort, i.e. inclusion of the Christie NHS Foundation Trust as an additional collaborating centre, and permission to include post-treatment recurrent HGG patients as well as follow-up scans, supported by Prof Jackson and Mr Coope. In addition to my previous role in patient recruitment and scanning, I had gained additional skills in inserting arterial cannula and managing the blood trolley for radioactivity and metabolite analysis. These skills helped me to complete the final cohort of the TSPO in TLGG study, which required metabolite analysis in view of validating for the first time the largely accepted cerebellar input function. Moreover, I have also volunteered in performing scans for other studies necessitating arterial line input functions and metabolite analysis like “FAZA in GBM” and “Leucine PET imaging in Dementia”.

PET image reconstruction and pre-processing (section 3.4.1) was done by Dr Anton and Dr Hinz. I conducted all the remaining PET data analysis as specified in this chapter. MR perfusion maps (e.g. CBV) were generated by Dr Xiaoping and Dr Kaloh, and analysed by me. I updated the literature review, interpreted the results and prepared the manuscripts presented in the experimental chapters, which were read and edited by all my supervisors as well as Prof Roncaroli (who conducted the histopathological assessment).

Chapter 4 – The Mitochondrial Translocator Protein Can Predict Anaplastic Transformation of Diffuse Gliomas

4.1 Abstract

Introduction: Early transformation from low- to high-grade glioma (HGG) remains challenging to detect with conventional MRI. Regions of malignant transformation can be missed where stereotactic biopsy depends solely on post-contrast MRI, subsequently under-grading the lesion. The translocator protein (TSPO) is an 18 kDa mitochondrial molecule up-regulated in gliomas and can be imaged by positron emission tomography (PET) using the selective radiotracer [11C]-(R)PK11195. We compared peak [11C]-(R)PK11195 uptake in relation to rCBV which has been demonstrated to rise in advance of conventional MRI markers of tumour progression.

Methods: Twenty-six patients (mean age 38±11.5, M/F=16/10) with lesions suspicious of transforming glioma on clinical MRI were recruited. All patients underwent perfusion MRI and dynamic [11C]-(R)PK11195 PET scans. Parametric maps of rCBV and TSPO binding potential were generated. Co-registered MR/PET images were used to guide tumour biopsy/resection. Tumour tissue resected was assessed using immunohistochemistry for TSPO antibody binding through optical density measurements and 3D reconstruction of tissue microarrays. Results of TSPO OD measurements were validated in a cohort of 30 consecutive oligodendroglioma.

Results: TSPO PET imaging with [11C]-(R)PK11195 showed an excellent accuracy in predicting transformation in LGG, especially in the oligodendroglial type. Progressively higher uptake of [11C]-(R)PK11195 was seen in anaplastic gliomas compared to the lower grade (BPNDmax: 1.59 ± 0.63 vs. 0.79 ± 0.28, $p=0.001$), whilst rCBV failed to show a significant difference (rCBVmax: 4.02 ± 2.51 vs. 3.01 ± 1.15, $p=0.23$). Expression of TSPO measured with an OD approach as a surrogate marker of protein content, correlated significantly with [11C]-(R)PK11195 BPNDmax (Pearson $r = 0.73$, $p<0.001$). TSPO antibody staining over 4% of the total area showed a good discrimination of low-grade from anaplastic tumours in a validation cohort of 30 oligodendroglial tumours (sensitivity 92.85% and specificity 93.75%, Youden Index 4.395). Double antibody staining showed a predominance of TSPO in the neoplastic tissue.

Conclusion: [11C]-(R)PK11195 PET imaging can offer good accuracy in prediction of transformation which can be also translated in tissue analysis via antibody staining. TSPO binding was mainly noted in the neoplastic cells and areas of peak tracer uptake did not co-localize to increased rCBV.

4.2 Introduction

Low grade and anaplastic gliomas account for approximately 20-30% of primary brain tumours[133] but have a socioeconomic impact that is disproportionate to their incidence due in part to their propensity to affect young adults [23, 134]. According to the current World Health Organization (WHO) classification [2], low grade and anaplastic astrocytomas (LGA, AA) or oligodendrogliomas (LGOs, AOs) are graded on the basis of their histological and molecular features as discussed earlier in section 2.1. Low-grade gliomas almost invariably progress to an anaplastic lesion and are eventually fatal, the interval from presentation to transformation is however highly variable and cannot be reliably predicted [23-25]. The low grade tumours in particular present specific challenges to management with the evidence of benefit from radical surgery and early oncological intervention needing to be balanced against the risk of inducing neurological deficits [135].

MRI remains the modality of choice to provide accurate morphological and anatomical information although conventional sequences offer only limited detail on the specific biological features and activity of an individual tumour. Tumour delineation, non-invasive grading and treatment planning for gliomas using MRI rely primarily on fluid T2-weighted attenuated inverse recovery (FLAIR) and contrast-enhanced T1 sequences augmented with diffusion- and perfusion-weighted acquisitions. However, the presence or absence of contrast enhancement lacks specificity which raises concerns of inaccurate grading [25, 136] whilst T2 derived FLAIR sequences can overestimate tumour extent [137, 138]. Positron emission tomography (PET) can provide complementary and in some cases unique information on tumour behaviour [139-141]. PET allows non-invasive characterisation of physiologic, metabolic and functional changes relevant to a disease, which may guide the therapeutic approach and additionally inform prognosis [139, 142, 143].
The translocator protein (TSPO) is an 18kDa highly conserved protein located in the outer mitochondrial membrane. It is composed of five transmembrane domains and in physiological conditions aggregates in homo-dimmers [50, 52]. TSPO represents one of the more promising PET imaging targets with an increasing interest in the last

ten years. It offers several advantages in the study of brain tumours because of its high expression of TSPO in gliomas, low uptake in the normal brain and biological relevance [65, 79]. In our previous studies, we demonstrated the suitability of the first generation TSPO ligand [^{11}C]-(R)PK11195 to investigate human gliomas and subsequently proved a correlation between TSPO expression and WHO grade [65, 119]. We also demonstrated neoplastic cells to be the major source of TSPO with endothelium and glioma associated macrophages and microglia (GAMMs) only partially contributing to PET signal [65].

We hypothesized that TSPO expression presents a specific marker of progression in gliomas and we have investigated this through an expanded cohort of histologically confirmed WHO grade II and III diffuse gliomas. We then validated PET imaging results against an independent tissue-based analysis focussing on oligodendrogliomas which demonstrate the strongest correlation between TSPO PET imaging and TSPO expression. The contribution to TSPO expression of neoplastic, endothelial cells and GAMMs was also investigated through a novel 3D histological approach and PET parameters evaluated against MRI metrics including cerebral blood volume for accuracy in determining tumour grade.

4.3 Materials and Methods

4.3.1 Patient selection

Twenty-six patients with a radiological diagnosis of a diffuse glioma on diagnostic MRI were recruited. All patients included in this study demonstrated radiological features suggestive of progression as evaluated by the Neuro-Oncology MDT and were suitable surgical candidates for either biopsy or debulking. Fourteen patients were part of a previous study cohort (TSPO imaging in Glioma, REC reference 09/H1014/41) recruited from January 2010 to November 2012, whilst twelve patients were recruited as part of an ongoing project commenced in April 2014 (TSPO imaging in Transforming Glioma, REC reference 15/NW/0071). Patients on treatment with benzodiazepines were excluded from recruitment, due to the potential competing binding with TSPO receptor. An additional cohort of tissue samples from Salford Royal NHS Foundation Trust Brain Tumour Biorepository of thirty consecutive resected oligodendrogliomas of WHO grade II and III was selected

retrospectively and anonymised for tissue validation. Written informed consent was obtained from all participants. Studies were approved by the Wrightington, Wigan and Leigh, and Central Manchester Ethics Committees respectively. Permission to administer radioisotopes was granted by the Administration of Radioactive Substances Advisory Committee of the Department of Health (ARSAC), UK.

4.3.2 MRI Imaging

All subjects underwent a dedicated study MRI scan within one month prior to the PET imaging (median 5 days, range 0 to 31 days) on a 3.0 or 1.5 Tesla scanner (Philips Achieva, Philips Medical System, Best, NL). Anatomical sequences were acquired as follows: 3D T1-weighted gradient echo, 2D T2-weighted turbo spin-echo, T2-weighted FLAIR and post-contrast 3D T1-weighted images following intravenous Gadolinium (Gd, Dotarem, Guerbet Laboratories, Aulnay-sous-Bois, France) administration.

T2* weighted dynamic contrast-enhanced data were acquired similarly on either 3T or 1.5T scanners using a multislice 2D T2*W-FEEPI (field echo-EPI) multi-shot sequence (3T acquisition TR 440ms, TE 30ms, PS=1.8x1.8mm, ST=3.5mm, and 1.5T acquisition TR 16ms, TE 24ms, PS=1.8x1.8mm, ST=3.5mm). Further details of DSC acquisition are described in Chapter 3 section 3.5.3 .

4.3.3 [^{11}C]-(*R*)PK11195 production and PET acquisition

[11C]-(R)PK11195 (1-(2-chlorophenyl)-N-methyl-N-(1-methylpropyl)-3-isoquinoline carboxamide) was synthesised as previously described [104]. All PET scans were performed on the High Resolution Research Tomograph (HRRT, Siemens/CTI, Knoxville, TE, US) with a final reconstructed voxel size of 1.22x1.22x1.22mm. Following injection of a target dose of 740MBq of [11C]-(R)PK11195 dynamic data was acquired for 60 minutes. Corrections for attenuation, scatter, dead time, random coincidences and detector normalisation were applied as previously described [65]. Post-reconstruction images were regularised with a 3D Gaussian filter of 4mm full width at half maximum to reduce image noise at the voxel level.

4.3.4 Image reconstruction and analysis

Parametric maps demonstrating [11C]-(R)PK11195 binding potentials (BPND) as the ratio of specifically bound tracer over non-displaceable tracer in tissue at equilibrium were generated. These were calculated using a simplified reference tissue model (SRTM) with two different 'pseudoreference' tissue input functions: 1) a cluster of grey matter (GM) voxels extracted using a supervised clustering algorithm [118]; 2) atlas defined cerebellar GM as a large and relatively homogeneous structure distant from the tumours [119]. After confirming that no significant difference was generated between the reference tissue approaches, cerebellar GM was selected as the preferred method for the remainder of the analysis.

The tumour VOI for each subject was projected onto the BPND parametric map to enable the region of peak tracer uptake within the FLAIR defined tumour volume to be identified and sampled. Mean BPND for a spherical sampling VOI with a 7mm diameter (179 voxels) centered on the voxel of interest was calculated for every voxel in the final tumour VOI using an automated analysis performed in R statistics (R Foundation for Statistical Computing, Vienna, Austria). Locations in which the sampling VOI extended beyond tumour region or which contained missing values were excluded. Maximum binding potential (BPNDmax) was defined as the mean of the sampling VOI which yielded the greatest value and was recorded along with the location of the center of the VOI.

All data were expressed as mean ± one SD. [11C]-(R)PK11195 uptake parameters were compared between grade II and grade III diffuse gliomas according to their histological type using 2-tailed t-test. A threshold value of BPNDmax >1.4 was evaluated as a potential discriminator for low grade and anaplastic glioma (threshold selected based on optimal Youden index and our previous imaging analysis in addition to similar other amino acid PET studies using T/N ratios [141, 144, 145]). BPND parametric images generated using different input functions were compared voxel-by-voxel using Bland–Altman plots [120] with local regression [121] and regional tumour VOI BPND values derived from the two input functions were compared using Pitman's test of difference in variance. A probability of $p<0.05$ was considered statistically significant.

4.3.5 T2* DSC image analysis

T2* DSC-MRI data were analysed in MIStar (Apollo Medical Imaging Technology, Melbourne, Australia). Relative cerebral blood volume (rCBV) maps were generated using delay- and dispersion-corrected singular value deconvolution [124]. rCBV maps were co-registered to the T1-weighted post-contrast MRI in PET space to minimise the interpolation of data while preserving the original PET data.

Similar to [11C]-(R)PK11195 analysis, rCBV peak values were extracted using a 7mm diameter spherical sampling VOI automatically drawn within the tumour mask after visual inspection to avoid blood vessels, calcification and haemorrhage. Pearson correlation coefficient between rCBVmax and BPNDmax values were calculated using GraphPad Prism version 8.1.2 (GraphPad Software, San Diego, USA).

4.3.6 Tissue analysis

Surgical specimens were fixed in 10% buffered formalin and paraffin embedded. The haematoxylin-eosin (HE) stained sections were reviewed by an experienced neuropathologist (F.R.) and diagnoses were made according to WHO criteria [131]. IDH-1 status and loss of heterozygosity of chromosomes 1p/19q were assessed with fluorescence in situ hybridization (FISH) .

The extent of TSPO expression in neoplastic cells, endothelial cells and GAMMs was assessed using peroxidase immunohistochemistry (IHC). This was performed using the Super Sensitive Polymer HRP IHC Detection System (BioGenex Laboratories, Inc. San Ramon, CA, USA) according to the manufacturer's protocol, with antibodies directed against TSPO (polyclonal goat anti-TSPO, dilution 1:750, GeneTex, Hamburg, Germany), $IDH1^{R132H}$ (Dianova, Hamburg, Germany monoclonal H09, 1:200) for IDH1 mutant tumour cells, the vascular marker CD31 (Dako CloneJC7QA Ref M0823, dilution 1:30) and macrophages / microglia (polyclonal rabbit anti-Iba1, dilution 1:500, WAKO, Neuss, Germany).

Distribution analysis of the TSPO in relation to CD31, IDH1 and Iba1 was performed using the Bitplane Imaris 3D/4D imaging software (Bitplane AG Zurich,Switzerland). (Full details of the technical aspects are reported in supplementary materials – please see Appendix 1). In addition, we used double immunofluorescence (DIF) to quantitatively define TSPO expression in neoplastic and microglial cells. TSPO and Iba1 immunostaining was evaluated using optical densitometry (OD). In seven

patients from our cohort TSPO OD was also evaluated from tissue obtained following a second surgical debulking due to progression.

Manders coefficients were used to quantify the co-localisation of different cells according to their immune-histochemical characterisation. Each subgroup (CD31, IDH1, TSPO and Iba1) was assigned a different colour channel. Proportional to the amount of the co-localizing voxels in each colour channel, values range from 0 to 1, expressing the fraction of intensity in a channel that is located in voxels where there is above zero (or threshold) intensity in the other colour channel. The closer to 1 the stronger is the co-localisation. [146]

4.3.7 Tissue validation cohort

TSPO OD was further validated in a cohort of tissue from 30 consecutive patients with oligodendroglioma of whom 14 were classified WHO grade III. All cases showed IDH1/2 mutation and 1p19q co-deletion. Five representative images were captured at a magnification of 20× (Nikon Fluoroplan 0.75mm, Nikon, Ltd. Japan) using a digital camera (DS Camera Control Unit DS-L1 and DS Camera Head DS-5M, Nikon, Ltd. Japan). Haemorrhagic areas, microcysts, necrosis and the fields at the edge of tissue sections were avoided. Image analysis was performed using Image J (ImageJ, U. S. National Institutes of Health, Bethesda, Maryland, USA). Following nuclear deconvolution, the surface area of TSPO staining was calculated against the total surface area and averaged for the 5 images representing each case. OD values expressed as average percentage of the total area were compared between low grade and anaplastic oligodendrogliomas using a two tailed t-test.

4.4 Results

Twenty-six patients (mean age 38±11.5, M/F=16/10) with a radiological diagnosis of a diffuse glioma and evidence of possible anaplastic progression on their diagnostic MRI were recruited. Fourteen patients were confirmed oligodendrogliomas with 1p/19q codeleted, of whom 3 were classified WHO grade III. Whilst 12 patients were diagnosed with diffuse astrocytomas, of whom 5 were anaplastic WHO grade III (details on Table 4.1). None of the patient had significant concurrent systemic disease and histological confirmation of diagnosis was obtained in all subjects. The

most common presentation was seizure (19 out of 26 subjects), managed with anti-epileptics. None of the subjects had surgical intervention, radiotherapy or chemotherapy prior to PET scanning. Nine patients were treated with dexamethasone which was stopped for at least 2 weeks prior to the PET scanning, except in two patients (patients 1 and 6) where the discontinuation was considered to be clinically contraindicated. Written informed consent was obtained from all participants.

Fifteen tumours showed no contrast enhancement, while the remaining eleven showed either faint (patients 1, 4, 5, 7, 16 and 26) or patchy enhancement areas (patients 9, 12, 21, 22, 25). Near or sub-total macroscopic surgical resection was achieved in 88.4% of patients and three patients underwent a diagnostic biopsy due to tumour location or patients' choice. Details of demographics, histology, surgical treatment and follow-up are summarized in Table 4.1. Mean follow-up time was 5.74 years (range 2.03 – 8.44 years). 13 subjects have been diagnosed with disease progression; 4 LGO (mean progression time 54.5 months, SD 27.06), 5 LGA (25.6 months, SD 21.14), 2 AO (56.5 months, SD 2.12) and 2 AA (40 months, SD 36.7).

ID	*Sex*	*Age*	*Presentation*	*Location*	*Resection*	*Histology*	*Progression*	*FUP (yrs)*
1	M	41	Seizures	Right temporal	ST	Oligodendroglioma WHO II	Yes	5.42
2	F	25	Headaches, personality changes	Right frontal	ST	Astrocytoma WHO II	Yes	0.99
3	F	37	Seizures	Right fronto-temporal	ST	Anaplastic Astrocytoma WHO III	No	4.75
4	M	45	Seizures	Right temporal	Bx	Oligodendroglioma WHO II	Yes	5.50
5	F	24	Headaches, seizures	Right occipital	ST	Oligodendroglioma WHO II	No	5.84
6	M	40	Seizures	Right frontal	ST	Oligodendroglioma WHO II	No	5.67
7	F	63	Seizures	Left parietal	Bx	Astrocytoma WHO II	Yes	6.45
8	M	33	Seizures	Right parietal	NT	Astrocytoma WHO II	No	5.17
9	M	42	Seizures	Left frontal	NT	Anaplastic Astrocytoma WHO III	No	5.54
10	M	31	Headaches	Right frontal	ST	Oligodendroglioma WHO II	Yes	1.66
11	F	47	Seizures	Left temporal	Bx	Astrocytoma WHO II	Yes	3.67
12	M	47	Seizures	Left temporal	ST	Anaplastic Astrocytoma WHO III	No	5.06
13	M	22	Left arm paraesthesia	Right parietal	NT	Anaplastic Oligodendroglioma WHO III	Yes	4.80
14	M	33	Seizures	Left frontal	NT	Astrocytoma WHO II	Yes	4.30

ID	*Sex*	*Age*	*Presentation*	*Location*	*Resection*	*Histology*	*Progression*	*FUP (yrs)*
15	M	42	Seizures	Left temporal	ST	Astrocytoma WHO II	Yes	4.71
16	M	24	Seizures	Right temporal	ST	Oligodendroglioma WHO II	Yes	2.31
17	F	50	Speech disturbance	Left frontal	ST	Oligodendroglioma II	No	4.81
18	M	24	Seizures	Left frontal	NT	Anaplastic Oligodendroglioma III	No	4.79
19	M	38	Incidental	Left frontal	ST	Astrocytoma II	Yes	1.01
20	F	52	Seizures	Right temporal	NT	Oligodendroglioma II	No	1.65
21	M	37	Seizures	Left frontal	NT	Oligodendroglioma II	No	1.61
22	F	54	Seizures	Right temporal	ST	Anaplastic Astrocytoma III	Yes	1.15
23	F	48	Speech disturbance	Left parietal	NT	Oligodendroglioma II	No	1.34
24	M	19	Seizures	Right fronto-temporal	NT	Anaplastic Astrocytoma III	Yes	1.19
25	M	24	Seizures	Left frontal	ST	Anaplastic Oligodendroglioma III	No	0.53
26	F	45	Seizures	Right frontal	ST	Oligodendroglioma II	No	0.42

Table 4.1 Details of demographics, histology, surgical treatment and follow-up.

4.4.1 [11C]-(R)PK11195 parametric images

Using the cerebellar GM SRTM derived BPND parametric maps, anaplastic gliomas demonstrated higher peak uptake of [11C]-(R)PK11195 compared to low grade gliomas (BPNDmax: 1.59 ± 0.63 vs. 0.79 ±0.28, p=0.001) (Figure 4.1).

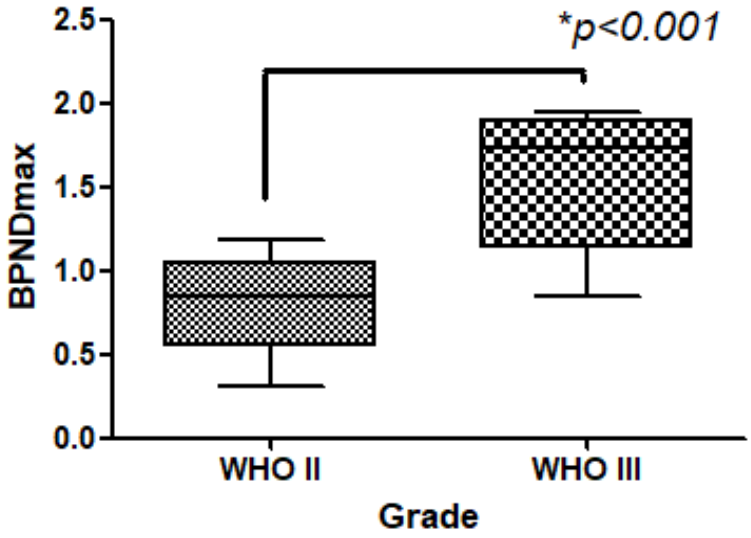

Figure 4.1 Box-plot comparing peak BPND values between WHO grade II and III gliomas.

Differences in BPNDmax persisted when astrocytomas and oligodendrogliomas were investigated separately (Figure 4.2 and 4.3). In particular, we observed a significantly raised BPNDmax in AOs compared to LGOs (BPNDmax: 1.96 ±0.53 vs. 0.84 ±0.26, $p<0.001$). The increased BPNDmax values were also present in AAs compared to LGAs (BPNDmax: 1.37±0.63 vs. 0.68 ±0.29, $p=0.029$). A threshold value of BPNDmax>1.4 showed 100% accuracy in discriminating LGO from AO. The sensitivity in distinguishing between LGAs and AAs was lower (40%) due to three AAs that displayed similar uptake as LGAs (patients 3, 9 and 12) (BP max 0.93, 0.96 and 0.84 respectively). Specificity though, was still 100% (with no false positives being identified), bringing the overall accuracy of detecting transformation to 75% (due to the 3 false negatives) in astrocytoma type.

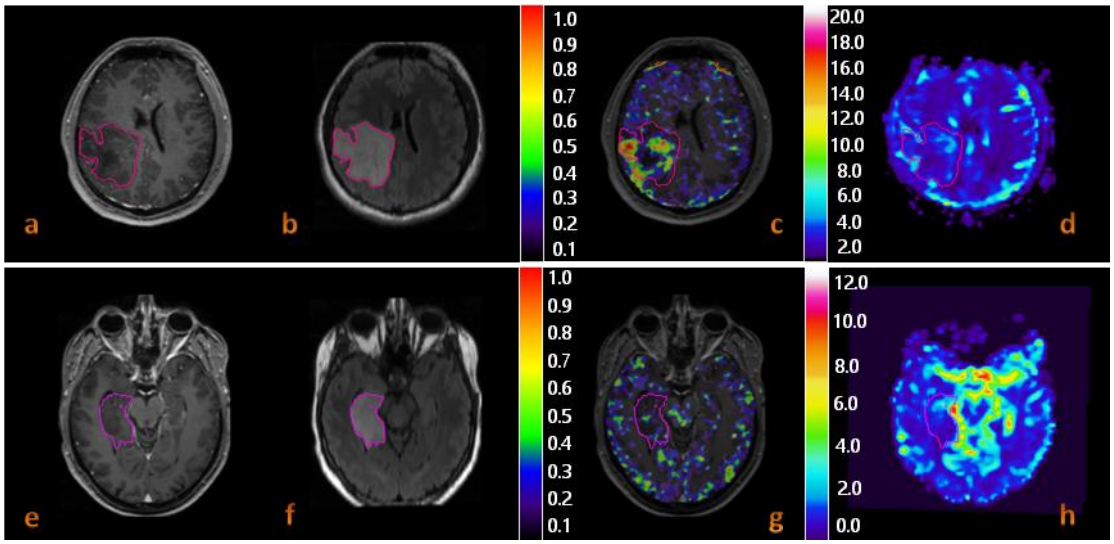

Figure 4.2 (a,b,e,f) Coregistered axial T1 post-contrast and axial T2 FLAIR MR scan images showing non enhancing lesions delineated according to the FLAIR hyper-intense signal change. (a,b) Anaplastic Oligodendroglioma WHO III. (e,f) Oligodendroglioma WHO II (c,g) Corresponding 11C-PK11195 binding potential parametric maps overlaying coregistered post-contrast T1 axial images. (d,h) Coregistered rCBV maps derived from T2*.

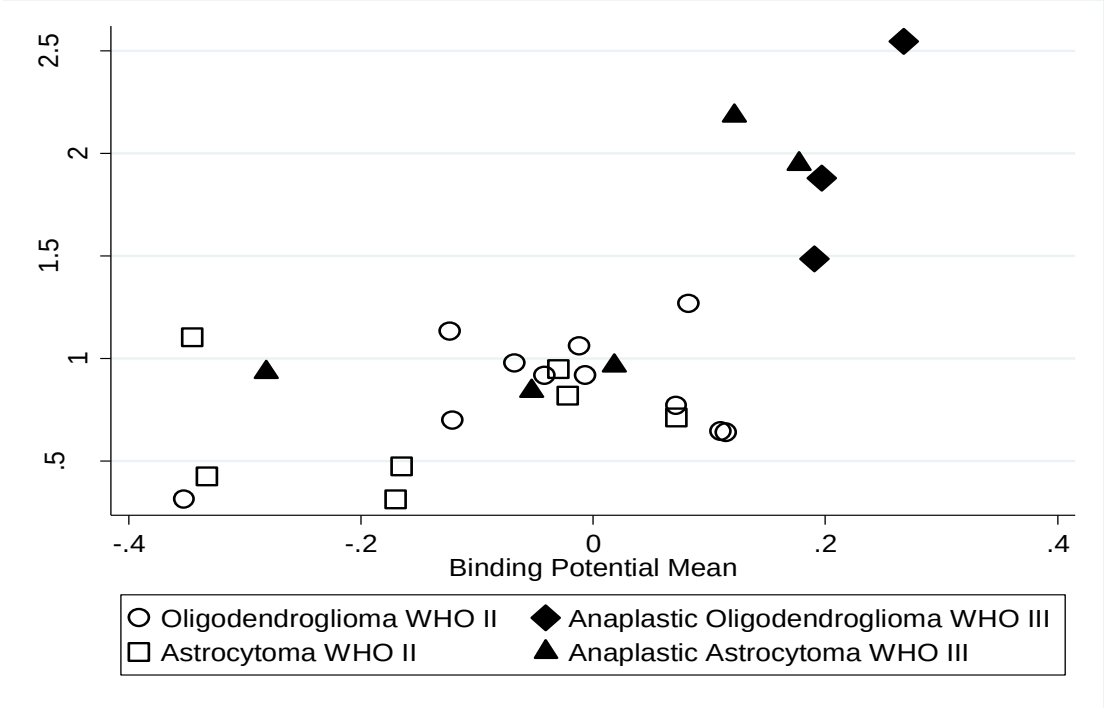

Figure 4.3 Scatterplot representing the exact BPNDmax (x-axis) and BPNDmean (y-axis) values for the whole tumour according to histotype and grade for each of the subject. Low grade tumours appear in empty symbols whilst the WHO grade III gliomas filled black. Of note all 3 anaplastic oligodendrogliomas are above the 1.4 BPNDmax threshold selected, whilst only 2 of the 5 anaplastic astrocytomas appeared above this threshold.

4.4.2 Comparison between post-gadolinium contrast enhancement and [11C]-(R)PK11195 binding

No significant difference was found in [11C]-(R)PK11195 binding between enhancing and non-enhancing tumours BPNDmax (0.97 ± 0.49 vs 1.13 ± 0.64, p= 0.47, two tailed t-test). 4 out of 8 grade III tumours showed no CE and 7/18 low grade tumours showed faint CE highlighting the poor discrimination in post-contrast MRI. Three anaplastic tumours in particular displayed no CE but pronounced [11C]-(R)PK11195 binding with BPNDmax over 1.4. Conversely none of the low grade tumours with faint enhancement demonstrated any rise in tracer uptake (Figure 4.4).

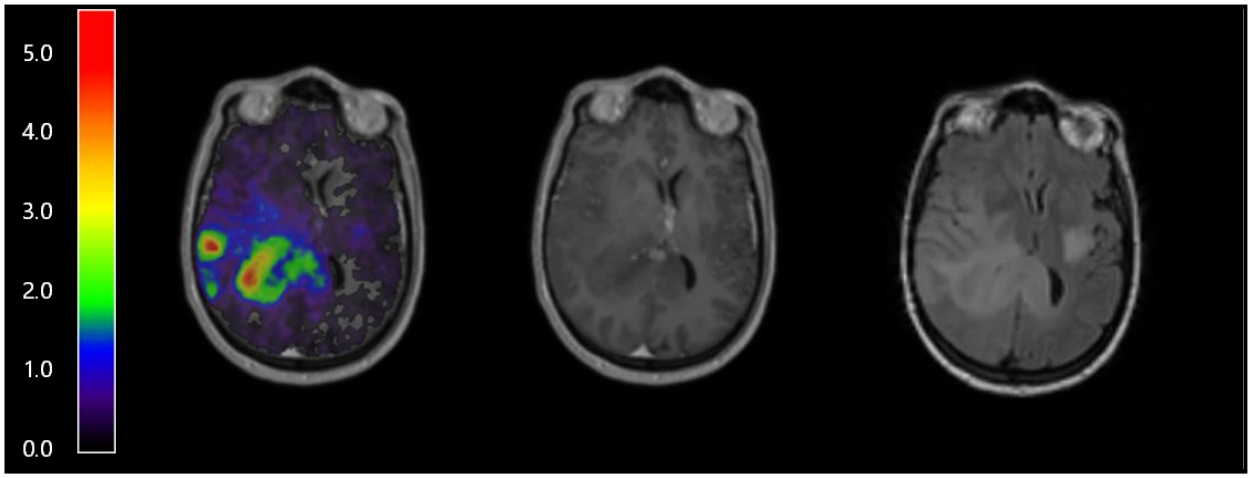

Figure 4.4 Diffuse anaplastic glioma showing areas of significant increased tracer uptake and no evident contrast enhancement. (from left to right: colour bar indicating BPND and coregistered PET, post-contrast T1 and FLAIR)

4.4.3 rCBV and [11C]-(*R*)PK11195 correlation

T2*-weighted DSC-MRI was acquired in all patients but following inspection was determined to be suitable for full analysis in 22 patients. Increased rCBVmax values were seen in oligodendrogliomas grade II and III compared to astrocytomas of the same grade (rCBVmax in LGOs vs LGAs: 1.67±0.56 vs 0.79±0.41 2-tailed t-test p=0.005, and in AOs vs AAs 2.59±0.96 vs. 1.24±0.37 respectively, p=0.0553). No significant difference in rCBVmax by grade was identified when the histological types were combined (rCBVmax in WHO II glioma 1.34±0.67 vs 1.69±0.86 in glioma WHO III, p=0.32) (Figure 4.5).

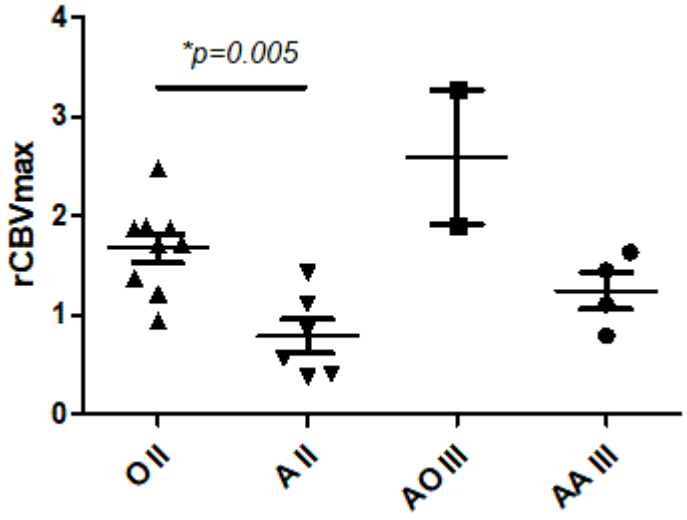

Figure 4.5 Peak rCBV (y-axis) by histological type and grade, represented in a dot chart. Low grade oligodendrogliomas showed a significantly higher rCBVmax compared to same grade astrocytomas, the rest of the groups showed no statistical difference. Bars and whiskers represent mean and standard deviation. O II = Oligodendroglioma WHO II, A II = Astrocytoma WHO II, AO III = Anaplastic Oligodendroglioma WHO III, AA III = Anaplastic Astrocytoma WHO III.

No correlation was found between rCBVmax and BPNDmax (Pearson's correlation coefficient 0.18, p=0.41). On visual inspection and using our in-house analysis the peak rCBV region and the maximal BPND within the tumour region were not spatially co-located (Dice Coefficient of spatial correlation 0.247, range 0.159 – 0.434).

4.4.4 Overlap FLAIR and [11C]-(R)PK11195

Analysis of co-registered FLAIR and [11C]-(R)PK11195 PET images did not reveal any areas of focally increased (BPND>1.4) [11C]-(R)PK11195 uptake outside of the tumour region delimited on FLAIR. In 10/26 patients we observed increased uptake in the ipsilateral hemisphere to the tumour location, specifically more in the cortex surrounding the tumour, occipital lobes, thalamus and brainstem. This was the case in five astrocytomas (subjects 3, 8, 11, 22, and 24) and five oligodendrogliomas (13, 16, 18, 25, and 26). In six patients we found focal areas of moderate increase in tracer uptake in the controlateral hemisphere to the tumour (two astrocytomas/four oligodendrogliomas) but this was under threshold value of 1.4 used to discriminate tumour with 100% specificity.

4.4.5 Tissue Analysis

Expression of TSPO measured with an OD approach as a surrogate marker of protein content correlated significantly with [11C]-(R)PK11195 BPNDmax (Pearson r = 0.56, p=0.0004) and therefore with WHO grade (Figure 4.6). Similar to the imaging results, three AAs showed low TSPO and overlapped with LGAs. In contrast, the three AOs showed 3 folds increase in TSPO compared to LGOs (TSPO OD mean 8.17 SD 1.21 vs. 2.51 SD 3.27, two tailed t-test p = 0.027).

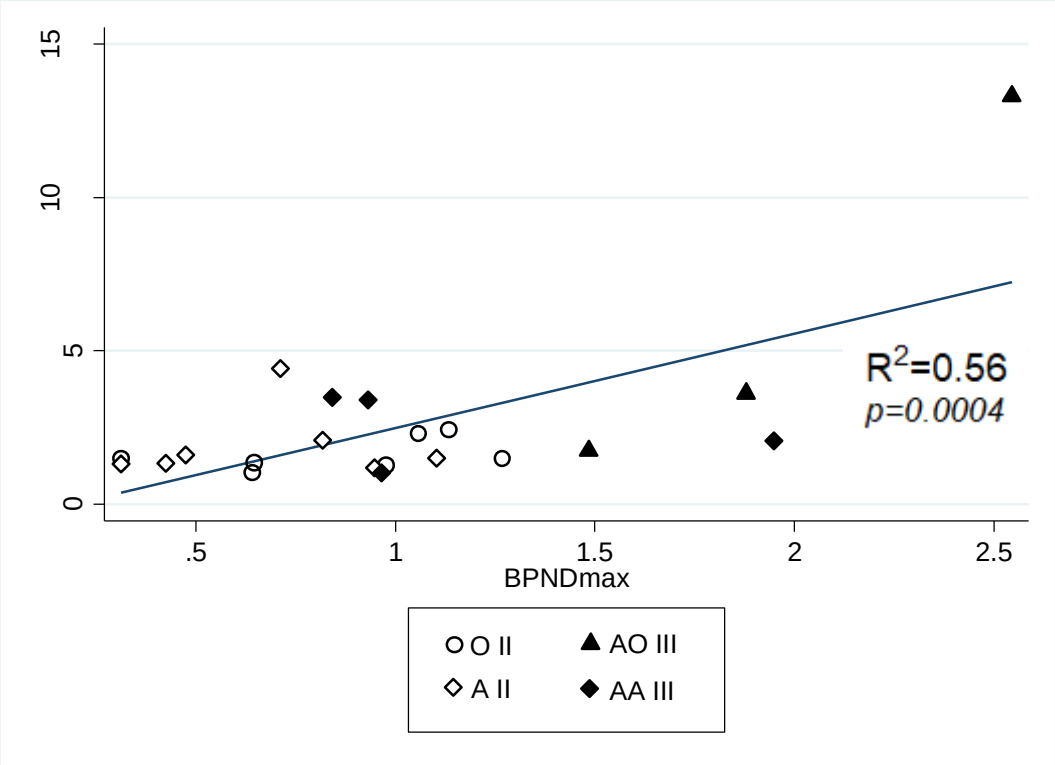

Figure 4.6 Tissue TSPO Optical Density measurements in correlation with [11C]-(R)PK11195 BPNDmax quantification.

OD analysis seven patients that underwent re-do surgery for recurrences showed significant increase in expression of TSPO in five tumours that progressed from low-grade to anaplastic (average OD primary: 1.30; average OD at recurrence: 4.98; paired t-test: 0.0048); one AO (patient 13) demonstrated similar expression in the recurrence (OD primary: 12.28; OD recurrence: 11.32) while one LGA (patient 11) did not show any increase in TSPO when progressing to anaplastic (OD primary: 1.49; OD

recurrence 1.75). Anaplastic features in this latter tumour were limited to a single area where mitotic activity was substantially increased. Changes in TSPO expression in primary and recurrent tumours are represented in Figure 4.7.

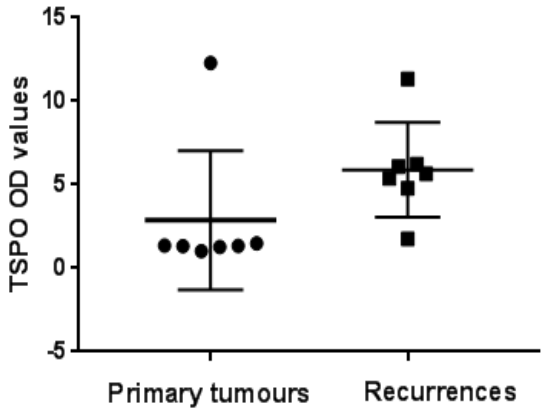

Figure 4.7 Dot-plot chart representing tissue TSPO binding measured through OD at first and second surgical procedure.

4.4.6 TMA

3D reconstructions of tissue samples from regions with high BPNDmax were used to evaluate the relative contributions of neoplastic cells, endothelium or GAMMs to TSPO binding. Tumour cells made the largest contribution to TSPO expression, as evaluated by the co-localisation coefficient of IDH1 to TSPO immunohistochemical colouration (mean Manders coefficient: 0.51) while endothelium (CD31 expressing cells) and GAMMs (Iba1 positive) contributed to TSPO expression for about 40% of the overall expression (mean Manders coefficient for endothelium: 0.370; mean Manders coefficient for GAMMs: 0.328). When compared with samples from LGG with lower overall expression the contribution from endothelium and GAMMs remained stable whereas the neoplastic expression reduced resulting in the overall reduction in measured TSPO expression (Figure 4.8).

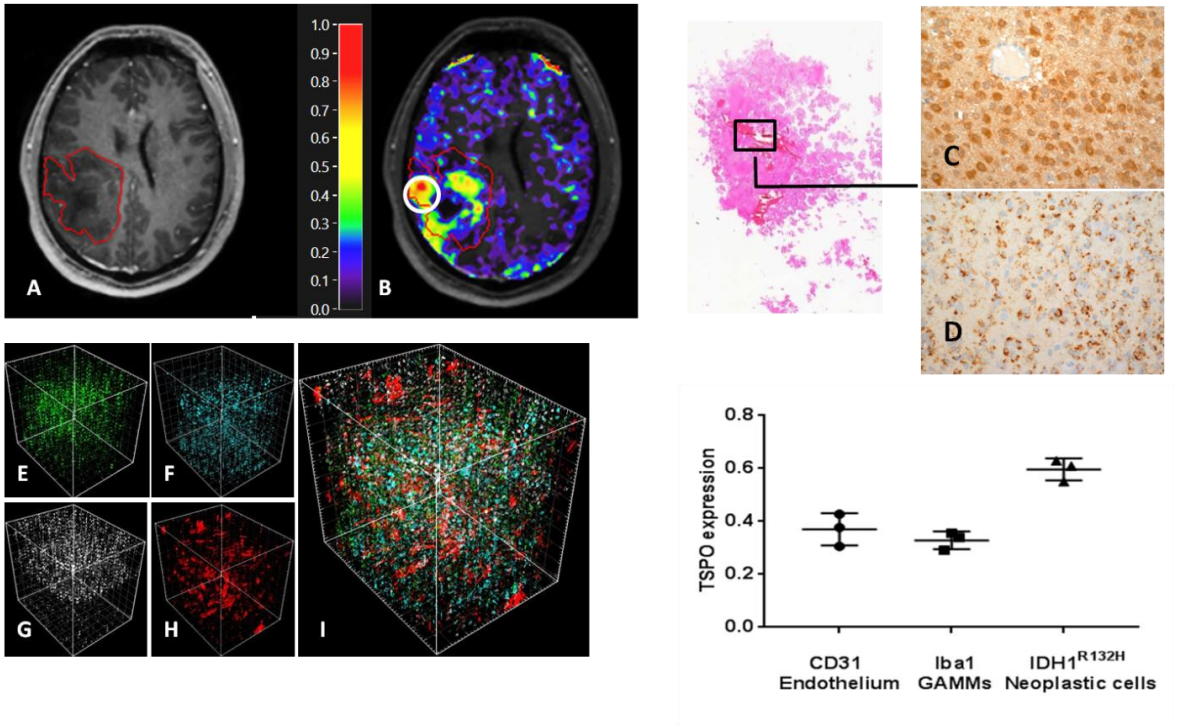

Figure 4.8 (A)Post-contrast T1 axial image with tumour delineated in red. (B) Coregistered fused PET with biopsy target area circled in white. (C) HE stained tissue from biopsied area showing x20 subsection of Iba1 (C) and TSPO (D) antibody IHC staining. (E-I) 3D tissue reconstructions of TSPO (E), Iba1(F),IDH1(G),CD31(H) and all fused in the same 3D space (I). (J) Index of TSPO co-localisation quantified by double antibody IHC staining showing prevalence in neoplastic cells.

4.4.7 Validation Cohort

Thirty consecutive oligodendroglial tumours were evaluated of which sixteen were WHO grade II and fourteen WHO grade III. LGO had an overall lower mean OD of 2.34 (SD 1.15) compared to AO 9.87 (SD 8.43) (Figure 4.9). Applying a threshold value of 4 to separate low-grade from anaplastic tumours produced a high degree of sensitivity (92.85%) and specificity 93.75%) (Youden Index J=4.395) (Figure 4.10).

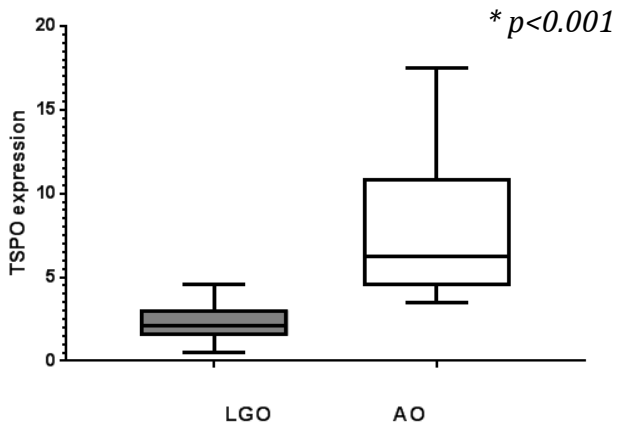

Figure 4.9 Boxplot demonstrating higher TSPO expression in anaplastic oligodendrogliomas.

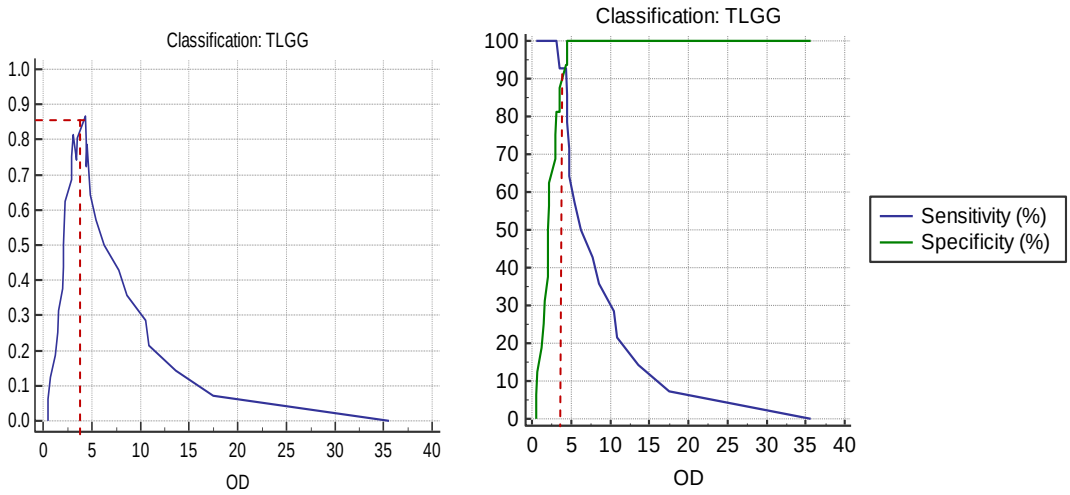

Figure 4.10 Optimal threshold defined by highest Youden Index and relative sensitivity/specificity (intersection point).

4.5 Discussion

This study builds upon our previous work to specifically evaluate the capacity of TSPO expression measured using PET or IHC to act as a biomarker of progression in LGG. The novelty relies on the direct quantification of TSPO in extended tissue analysis as compared to the PET imaging in the same cohort of glioma patients. Our previous study from *Su et al.* [65] showed an increasing uptake with grade confirmed to correlate with tissue measurements. The presented data still demonstrate this relationship is valid and true in gadolinium non-enhancing gliomas with presumed intact BBB.

A simple threshold method was demonstrated to provide highly accurate discrimination of WHO grade II and III tumours particularly for tumours of an

oligodendroglial type. WHO grading of gliomas is dependent upon several morphological features and it is highly unusual to be able to differentiate tumours based upon a single imaging or pathological parameter. A binding potential threshold value of over 1.4 produced 100% specificity in identifying anaplastic tumour with PET from a series of 26 $IDH1^{R132}$ mutant gliomas. Similarly, an OD threshold of 4 yielded 92.85% sensitivity and 93.75% specificity in a series of 30 consecutive oligodendrogliomas used as a validation cohort to evaluate the earlier established threshold. The thresholds of 1.4 (BP) and 4 (IHC) were selected as the ones with the highest predictive accuracy based on the final histologies reviewed independently by an experienced neuropathologist.

Our data demonstrated better accuracy in the oligodendroglial tumours, although in the PET imaging cohort there were only three anaplastic oligodendrogliomas, accuracy was further validated in a larger consecutive cohort with proportionate grade II and grade III oligodendroglial tumours with confirmed 1p19q codeletion. As has been previously hypothesised, in numerous amino acid PET studies, oligodendrogliomas might exhibit a higher tracer uptake due to their more prominent vasculature. Endothelium binding of TSPO tracers has already been described previously in neuro-inflammation studies to account up to 16.8% of the signal [147]and input functions with an additional class to account for the endothelium binding have been suggested [148]. Although, from our previous results of double immunofluorescence in glioma patients, we showed that TSPO binding was due predominantly to neoplastic cells rather than GAMMs or endothelium [65]. In the present study we improved the tissue quantification method using 3D reconstructions of tissue microarrays with TSPO double-IHC for microglia (Iba1), endothelium (CD31) and neoplastic cells ($IDH1^{R132}$). The results appear to re-enforce our previous findings showing the majority of contribution to TSPO binding being from neoplastic cells whether grade II or grade III gliomas [65, 149].

From a PET imaging perspective, no correlation with blood brain barrier breakdown as exemplified by contrast enhancement or cerebral blood volume was identified. Two reference tissue approaches were again evaluated in the application of the simplified reference tissue model due to concerns of the potential influence of infiltrating tumour cells or immune cell activation within the reference region[148]. No significant difference was identified between the reference tissue methods

building upon our previous finding and suggesting the analysis using cerebellum SRTM still to be robust [119]. Despite concerns of possible underestimation of BP in patients with intracranial disease or overestimation in the elderly cohort [150], using cerebellum as a reference region remains an established method [118, 119], and the only possible way to precisely evaluate its consistency would be through an arterial input function.

Within the study [11C]-(R)PK11195 outperformed contrast enhancement or rCBV in discriminatory accuracy for WHO grade II and III tumours. Although, our study power is limited to draw any conclusions, especially with a very low number of anaplastic tumours where the DSC data was available. A previous multi-centre study has shown that a significant difference of rCBV between low grade and anaplastic tumours [151]. Simlarly, relative blood volume derived from DSC MRI has been shown to anticipate transformation areas before contrast enhancement [26, 27]. Despite, there is a large overlap of grading in multiple studies and predictive accuracy varies consistently. Apart from the poor prediction accuracy of transformation (AUC 0.56, 95% CI 0.324 – 0.777), our results showed a poor spatial correlation of peak rCBV and [11C]-(R)PK11195 BP.Whilst other studies have shown that gadolinium enhancement solely or commonly used MR brain tumour protocols could possibly underestimate malignancy grading in diffuse glioma[152, 153].

Other PET tracers including amino acid tracers such as 11C-MET, 11C-AMT, 18F-FET, and 18F-FDOPA are more widely used for the characterisation and grading of gliomas. All have demonstrated very good and promising results in identifying most malignant target areas and increasing uptake with grading, although there is a greater overlap between low grade and anaplastic tumours particularly with simple threshold analyses [85, 154, 155]. This may result at least in part from a lack of specific binding and heavy influence from transport of the tracer at the vascular endothelium for amino acid tracers. The majority of this overlap is mainly noted in the oligodendroglial group, which has largely been attributed to the vascularity. TSPO PET imaging may have a higher benefit specifically in this category of previously confirmed 1p19q codeleted gliomas for disease monitoring and early identification of transformation.

Quantifying the contribution of tumour cells, vessels and inflammatory cells to PET signal using 3D reconstruction and double immune-staining, showed that neoplastic

cells' TSPO expression contributes to over 60% of PET signal. Regions with BPNDmax as high as 1.4 were found to be representative of high grade transformation in both astrocytomas and oligodendrogliomas with an increase in expression in neoplastic cells and also an increase in signal due to increased cellularity. In the previous study published by our team [65] our results were very similar, although the previous cohort included also WHO grade IV gliomas which might have contributed to more significant results but also making the cohort more heterogeneous due to the different histopathogenesis and different tumour microenvironment. Considering the previous results in addition to the present findings from the low and anaplastic grade tumours, there appears to be an overall quiescent state of the TSPO expression within the tumour when still in the low grade phase but with increased TSPO expression in the surrounding margins of the tumour which could represent a state of neuro-inflammation, although this might be seizure driven inflammation. Subsequently in the transforming areas of the anaplastic tumours microglia and neoplastic tissue starts to exhibit an increase of the TSPO expression which is predominantly driven by the neoplastic cells. In the primary GBMs though the contribution of neoplastic and GAMMs in TSPO expression becomes almost equal.

In seven patients of our cohort who underwent repeat surgery for suspected radiological progression and tumour enlargement, six patients were confirmed to have progressed and one had remained unchanged. In all six patients that had progressed repeat TSPO OD showed increased values. The cellular pathways driving the upregulation of TSPO in transforming low grade glioma could represent complex mechanisms requiring further studies to elucidate, though presently tissue TSPO OD measurement could be a potential surrogate marker of protein content and thus offer an objective quantification and ease diagnosis where PET imaging is not available. Further limitation of [11C]-(R)PK11195 PET imaging in clinical settings due to the short half-life of the tracer, could be overcome from newer generations of fluorinated TSPO tracers.

Numerous preclinical and clinical studies have demonstrated prognostic implications associated with elevated TSPO expression in multiple tumour types. TSPO might offer in the future the possibility of a directly therapeutically targeted protein which can also be imaged.

4.6 Conclusion

TSPO PET imaging can offer advantages in identifying transformation in low grade glioma with better accuracy in oligodendrogliomas compared to other imaging modalities including rCBV and amino acid PET imaging. Measurement of TSPO binding with immunohistochemistry remains a reliable surrogate which correlates to the PET imaging. TSPO is predominantly expressed by the neoplastic cells and does not correlate spatially with areas of increased rCBV.

Chapter 5 – Intra-tumoural correlation and co-localization of peak [11C]-methionine uptake with MRI perfusion and diffusion parameters in gliomas

5.1 Abstract

Introduction: Previous studies have shown that positron emission tomography (PET) with amino acid tracers can localize active glioma areas for targeted biopsies to provide accurate histological grading. Relative cerebral blood volume (rCBV) and flow (rCBF) maps obtained by dynamic susceptibility contrast-enhanced magnetic resonance imaging (DSC-MRI) and diffusion tensor imaging (DTI) is more widely available and may potentially provide closely related information.

Methods: Forty-one patients with suspected or proven gliomas (WHO grade I to IV) were recruited and underwent high resolution [^{11}C]-methionine PET in addition to a comprehensive MRI protocol including perfusion and diffusion sequences. Peak uptake values were recorded using an automated method and inter-modality correlation coefficients were calculated for the resulting values. The distances between the regions of "greatest malignancy" defined by each modality as putative biopsy targets were also calculated. Time activity curves were compared for intermodality peak areas of rCBV and MetPET in the different histological groups.

Results: Significant increasing methionine uptake was seen with increasing histological grade ($p<0.001$). A trend of increased uptake was noted in the oligodendroglial tumours compared to the same grade astrocytomas, although this failed to reach statistical significance ($p=0.46$). Peak MetPET ratio of 3 or above correlated to a significantly shorter progression time ($p=0.002$). Significant positive linear and rank correlations were identified between peak methionine uptake ratios and peak values for both rCBV ($p=0.004$) and rCBF ($p=0.036$), as well as trough values for FA ($p<0.001$).For the trough MD, an inverse correlation was found in relation to the methionine peak uptake ($p=0.001$). Correlation of peak MetPET with rCBV is maintained for oligodendrogliomas ($p=0.02$) but is lost in the other histotypes. More than half of the measured distances between peak and trough VOIs (56.8%) were greater than 15mm making them clinically relevant differences in the context of biopsy and intervention targeting. Smoothed time-activity curves of methionine uptake showed a significant difference between the Peak MetPET and rCBV VOIs in the oligodendrogliomas ($p=0.029$), but not in the low and high grade astrocytic tumours.

Conclusion: This data suggests that although closely correlated, neither CBV/CBF nor diffusivity mapping can directly replace amino acid PET for targeting of biopsies particularly in low-grade or low-uptake tumours.

5.2 Introduction

In the first part of this study we noticed a correlation of increased uptake in the transforming glioma using TSPO PET imaging which was more accurate in 19/19q codeleted oligodendrogliomas. This correlation was weaker in astrocytomas due to false negatives. We also noted increased rCBV values in oligodendrogliomas compared to same grade astrocytomas, although this did not co-localise indicating different pathological processes highlighted by [11C]-R-PK11195 PET imaging. In this experimental chapter we investigate different biomarkers in low and high grade gliomas with the aim to explore further discrepancies between astocytic and oligodendrolial tumours as well as evaluate with a multi-biomarker approach grading and prognostication in glioma.

Primary brain tumours continue to present specific imaging challenges, in particular related to grading and progression, from initial diagnosis, through surveillance and treatment planning, to response assessment and prognostication. Even histopathological confirmation of the final diagnosis as the ultimate "gold standard" demonstrates significant inter-observer variability between neuropathologists [156]. That variability is increased if only a small tumour sample, such as that obtained from a stereotactic biopsy, is available for histological diagnosis. There is often considerable heterogeneity of histopathological characteristics within gliomas. Thus, if a sample does not represent the most malignant tumour component it may falsely suggest a lower grade of malignancy or rather treatment related changes instead of tumour progression.

Imaging-based biomarkers offer clear benefits in that they can be applied longitudinally, allowing not only for characterization of a tumour at presentation but also for the identification of any change in the imaging characteristics over time. Several MRI and nuclear medicine techniques have been evaluated with respect to their potential utility in neuro-oncology [141] although relatively few have entered clinical practice even in specialist centers. Dynamic MRI techniques for deriving perfusion and permeability metrics have been of particular interest with T2* dynamic susceptibility contrast (DSC) enhanced MRI being the most widely available. Derived parameters include relative cerebral blood flow (rCBF) and relative cerebral blood volume (rCBV), which has been shown to correlate with microvessel density [32] in human gliomas. Increasing rCBV values have been found in higher grade tumours

[26] and perhaps more importantly increases in rCBV have been noted to precede the appearance of contrast enhancement by up to 12 months [27]. Peak rCBV has also been used to determine appropriate targets for biopsy particularly in non-enhancing gliomas that would otherwise pose a challenge [33]. Diffusion-weighted imaging can be used to derive information reflecting changes in the microcellular environment both of the tumour and of the surrounding brain. Diffusion characteristics within an individual tumour can be used to differentiate solid tumour from cystic or necrotic areas and tumour core from peri-focal edema [157]. A trend towards decreasing apparent diffusion coefficients (ADC) with increasing tumour grade has been demonstrated in astrocytomas [37], equating to a greater restriction in the free diffusion of water in malignant tumours. This has been suggested to correlate with increasing cellularity in high grade tumours [38] although attempts to confirm the relationship between ADC and cell density have yielded both positive [41] and negative [40] results. This inconsistency may reflect the influence of changes in the extra-cellular space whose constituents and physical characteristics also vary with histological grade in-line with the measured decrease in local diffusivity [42]. Few other studies have suggested that MD (or the equivalent ADC), can be used to differentiate between normal white matter and enhancing tumour margin or vasogenic oedema in HGG [43]. It has also been suggested that FA values of the tumour core can be used to discriminate between LGG and HGG [44].

Positron emission tomography (PET) with [18F]-fluoro-deoxyglucose (FDG) is the most widely used nuclear medicine technique in oncological practice but the high glucose consumption of normal cortex limits its usefulness in neuro-oncology. Amino acid tracers overcome this problem by demonstrating low uptake in normal brain and high uptake in the most active parts of gliomas, including non-enhancing LGG [140]. [11C]-methionine is perhaps the best-evidenced tracer and has been applied to differential diagnosis [80], biopsy targeting [81], resection [82] and radiotherapy planning [83] in gliomas. The clinical utility of [11C]-methionine PET (MetPET) is limited by the short half-life of the tracer, which necessitates on-site production. However, amino acid tracers with more practicable half-lives such as [18F]-fluoroethyl-tyrosine (FET) [84] and [18F]-fluoro-DOPA [85] are increasingly available and yield similar results [86]. An increase in methionine uptake has been demonstrated with increasing tumour grade [140] which is robust within gliomas of a specific histological type [90]. The relatively high sensitivity and specificity of the

technique in delineating tumour extent [91] combined with correlation between peak uptake and histological grade makes MetPET well suited to tumour surveillance and evaluation of treatment response [92]. Methionine uptake has also been shown to correlate with microvessel density [93] and tumour cell density [158] on previous histopathological studies in addition to correlating with tumour cell proliferative activity [95, 158].

Amino acid PET has proven diagnostic utility for guiding stereotactic biopsy [81, 85, 96, 97] and a similar role has been proposed for perfusion-weighted MRI [33], which has the potential to be much more readily available. A better understanding of the relationship between the findings obtained by these different approaches would enable diagnostic strategies to be rationalized, particularly with respect to the role of amino acid PET given its cost and relative lack of availability. Intra-tumoural variability in the extent to which the results different modalities correlate may also yield further insights into tumour behavior in vivo. However, the current evidence base describing multi-modal investigation of individual tumours with PET and extended MRI is limited, in part due to the technical challenges in correlating results from different modalities with differing spatial and statistical characteristics. The increasing availability of high field strength MRI and improved spatial resolution in PET imaging also allows more detailed study of the intra-tumoural distribution of imaging changes and for the location of high-signal areas, as indicators of tumour regions with the "highest malignancy" and as potential biopsy targets. We have, therefore, undertaken a prospective multi-modal neuroimaging study with high resolution MetPET and a comprehensive MRI tumour protocol in a cohort of patients with gliomas of different grades to investigate the correspondence of findings between the two techniques.

5.3 Materials and Methods

5.3.1 Patient selection

Study participants were identified through the weekly Neuro-Oncology Multi-Disciplinary Team Meeting at the Greater Manchester Neurosciences Centre (Salford

Royal NHS Foundation Trust, UK). Patients with solitary intra-cranial space occupying lesions consistent with gliomas on diagnostic MRI, in whom neurosurgical intervention (biopsy or debulking) was being considered, were reviewed. Specific exclusion criteria included known extra-cranial malignancy, age less than 16 years, poor performance status (Karnofsky performance score < 70 or WHO performance status > 2), high (>16mg / 24 hours) or unstable corticosteroid dose, or specific contra-indications to MRI or PET imaging. All study participants gave written informed consent to undergoing the imaging investigations and to extended analysis of any tissue specimens obtained. Patients underwent routine follow-up according to their tumour type and adjuvant treatments. Participants were recruited in two separate cohorts approved by Salford and Trafford Local Research Ethics Committee (07/Q1404/50) and North West - Greater Manchester South Research Ethics Committee (16/NW/0548). Both studies were also approved by the Administration of Radioactive Substances Advisory Committee of the Health Protection Agency (RPC 595/3586/21886 and RPC 595/3586/35328 respectively).

5.3.2 High Resolution 11C-MetPET Acquisition

PET scans were performed on an ECAT High Resolution Research Tomograph (HRRT) (CTI / Siemens Molecular Imaging Inc., TN, USA) [108]. This is a dedicated PET brain scanner which incorporates depth-of-interaction information obtained from a dual-layer scintillator to provide a spatial resolution of approximately 2.5mm full-width half maximum (FWHM). Subjects were fasted for a minimum of six hours prior to the scan, which was performed in a quiet room with dimmed lighting and a regulated ambient temperature. A 6.5 minute transmission scan was performed for attenuation correction prior to injection of the tracer using a 137Caesium transmission point source. A target dose of 740MBq of [11C]-methionine was injected manually over 20 seconds followed immediately by a 10ml 0.9% saline flush injected at the same rate. Emission data was acquired for 40 minutes from injection and reconstructed to give a static frame from 20-40 minutes post-injection for this analysis. Image reconstruction was performed using an iterative algorithm, Ordinary Poisson Ordered-Subset Expectation Maximization (OP-OSEM) (12 iterations, 16 subsets) [112], with corrections applied for random events [113], attenuation [114] and scatter [115]. Images were calibrated against a phantom with known radioactivity

and smoothed with a 2.5mm FWHM Gaussian filter corresponding to the resolution of the scanner.

5.3.3 MRI Acquisition

All participants underwent a standardized brain tumour protocol performed on a Philips Achieva 3.0 or 1.5 tesla scanner (Philips Healthcare, The Netherlands). Anatomical sequences included an axial T1 inversion recovery (TI=1150ms, pixel size(PS)=0.94x0.94mm, slice thickness (ST)=1.8mm on the 3T scanner and TI=1000ms, PS=1.19x1.19mm, ST=1.25mm on the 1.5T scanner), high resolution axial T2 (3T acquisition PS=0.26x0.26mm, ST=3.0mm and 1.5T PS=0.45x0.45mm, ST=6mm) and coronal FLAIR (3T acquisition PS=0.45x0.45mm, ST=3.0mm and 1.5T PS=1.07x1.07mm, ST=1.25mm). Diffusion tensor images (DTI) were acquired with 6 non-collinear gradient directions on both scanners (B=0 and 1000 s/mm2, PS=1.8x1.8mm, ST=5mm on the 3T scanner and PS=1.8x1.8mm, ST=1.8mm on the 1.5T respectively). Perfusion and permeability sequences were acquired as an oblique sagittal block incorporating the tumour along with the ipsilateral middle cerebral and internal carotid arteries. This acquisition is planned to optimize temporal and spatial resolution whilst facilitating input function calculation. T2* weighted dynamic contrast-enhanced data were acquired similarly on either 3T or 1.5T scanners using a multislice 2D T2*W-FEEPI (field echo-EPI) multi-shot sequence (3T acquisition TR 440ms, TE 30ms, PS=1.8x1.8mm, ST=3.5mm, and 1.5T acquisition TR 16ms, TE 24ms, PS=1.8x1.8mm, ST=3.5mm). Further details on DSC acquisition is described earlier in chapter 3 section 3.2 .

DTI data was processed using FDT (FMRIB's Diffusion Toolbox) from FSL version 3.3 [127]. Eddy current and motion correction was performed prior to fitting of the diffusion tensors. Processing of the DSC data was performed using both Phillips proprietary software for treatment planning and using MIStar (Apollo Medical Imaging Technology Pty. Ltd., Melbourne, Australia) for further analysis. The model employed was Singular Value Decomposition Deconvolution with Weiskoff correction for contrast extravasation [124]. A manually defined input function was utilized, defined as 2-5 voxels from 1-3 contiguous slices through a transverse section of the middle cerebral artery ipsilateral to the tumour being studied. Voxels adjacent to and

not within the artery were selected to optimize measurement of the susceptibility effect [125].

5.3.4 Image Analysis

Individual PET and MRI sequences were co-registered to the T1 Inversion Recovery data, re-sliced to give isotropic 1mm3 voxels, using a hierarchical rigid-body registration algorithm [116] implemented in Vinci version 2.53 (Max-Planck Institute for Neurological Research, Cologne, Germany). For the DTI and DSC data, B0 and pre-injection T2* images respectively were co-registered using an initial manual pre-fitting followed by a constrained 2-level rigid-body registration process with the resulting transformations subsequently applied to the derived parametric images. Co-registered anatomical images were segmented using the "New Segment" tool [123] in Statistical Parametric Mapping version 8 (SPM, Wellcome Trust Centre for Neuroimaging, University College London, UK). White and grey matter masks for intensity normalization were prepared using a threshold value of 95%. A brain mask was also derived from summed white and grey matter segments with a low threshold (10%) to ensure that the tumour was not excluded from this mask.

5.3.5 Determination of Peak Uptake Values

A tumour volume of interest (VOI) was manually defined on the FLAIR images with co-registered post-contrast T1 and MetPET images available to clarify any regions of uncertainty. All abnormal regions were included in the VOI and visualized blood vessels were manually excluded to improve the quantitative assessment of cerebral blood volume (CBV) and flow (CBF). Excluding the blood vessels from the perfusion parametric maps has been shown to correlate closely to the absolute values of CBV and CBF acquired through PET imaging as well as correlate better to histological grading in LGGs [151, 159]. This technique could also avoid false peak CBV and CBF, or even peak tracer values which could be the result of increased influx rate from the vessel signal. Voxels with a calculated blood flow on DSC of greater than 2.5 times the median for non-tumour voxels within the brain mask were defined as representative of large vessels [160] and were excluded. Regions of the tumour VOI that lay beyond the brain mask or for which valid results were not available for every modality were further excluded. The final VOI was eroded by up to 5 voxels (5mm) to minimize the

confounding effect of perivascular voxels and relatively normal cortex at the edge of the VOI. The erosion process was constrained to prevent the final tumour VOI containing less than 1000 valid voxels for evaluation wherever possible. Peak uptake was determined using the mean of a spherical VOI with a 7mm diameter (179 voxels), every voxel in the final tumour VOI was evaluated to determine which yielded the peak value using an automated analysis performed in R statistics (R Foundation for Statistical Computing, Vienna, Austria). Trough values were also calculated for the DTI metrics. MetPET uptake values are presented as the ratio to normal appearing cortex. DSC values are presented as the ratio to normal appearing white matter defined as the mean of the white matter segment after exclusion of the tumour VOI as data for mirrored controlateral regions was not consistently available. Fractional anisotropy (FA) and mean diffusivity (MD) are presented as the calculated values. Pearson product moment and Spearman rank correlation coefficients between peak and trough uptake values were calculated in GraphPad Prism version 8.1.2 (GraphPad Software, San Diego). The effects of tumour grade and group were analyzed by two-way ANOVA (general linear model). Kaplan-Meiers curves were generated based on progression-free estimates and compared in the different Peak MetPet groups using Log-rank test of variance (Mantel-Cox). Distances between the peak and trough VOIs for each modality were calculated and are reported in millimeters.

5.4 Results

Forty-two patients were recruited in the study; one patient was excluded following final diagnosis of CNS lymphoma leaving forty-one participants for the final analysis. The mean age at the time of the PET scan was 51 years (range 16.4-76.2 years) with 24 male and 17 female participants. The mean interval between PET and MR studies was 7.4 days (range 0-53 days).

Table 5.1 Study participant characteristics, histological diagnoses and multi-modal peak / trough values.

ID	Age	WHO Grade	Histological Type	Peak Values (Ratio)				Trough Values	
				MetPET	rCBV	rCBF	MTT	MD (mm^2/s)	FA (0-1)
1	35	I	Ganglioglioma	1.43	3.68	4.29	1.86	0.002267	0.059
2	37	I	Pilocytic Astrocytoma	1.89	1.08	1.55	2.26	0.001427	0.096
3	39	Likely LGG[1]	Unknown	1.10	3.31	2.56	2.14	0.001924	0.086
4	16	Likely I[2]	Likely Pilocytic Astrocytoma	1.29	3.15	3.86	4.54	0.001219	0.081
5	39	II	Oligodendro-glioma *	3.00	3.40	4.00	1.73	0.002127	0.050
6	31	II[3]	Oligodendro-glioma *	5.34	4.10	2.98	3.66	0.001517	0.074
7	46	II	Oligodendro-glioma *	3.11	3.27	3.32	2.34	0.001715	0.068
8	45	II[d]	Oligodendro-glioma *	2.76	3.38	3.00	2.59	0.002376	0.045
9	32	II	Oligodendro-glioma **	1.98	3.29	3.99	1.80	0.002804	0.045
10	45	II	Oligodendro-glioma	1.96	2.84	3.38	3.38	0.001448	0.073
11	46	II[d]	Oligodendro-glioma *	2.73	2.79	2.52	2.84	0.001795	0.046
12	34	II	Diffuse Astrocytoma	3.16	4.82	3.23	3.22	0.001713	0.047
13	41	II[d]	Diffuse Astrocytoma	1.33	2.95	3.11	1.77	0.002164	0.053
14	44	II	Diffuse Astrocytoma	2.04	2.79	2.98	1.88	0.002224	0.045
15	30	II	Diffuse Astrocytoma	1.33	4.51	5.04	1.68	0.002513	0.053
16	32	II	Diffuse Astrocytoma	1.60	2.39	2.47	1.33	0.002002	0.050
17	37	III[4]	Anaplastic Astrocytoma	3.11	3.60	4.17	2.07	0.001985	0.086
18	48	III[5]	Anaplastic Astrocytoma	3.74	6.10	5.16	3.55	0.001758	0.069
19	62	III	Anaplastic Astrocytoma	5.51	3.43	2.59	1.96	0.00176	0.087

ID	Age	WHO Grade	Histological Type	Peak Values (Ratio)				Trough Values	
				MetPET	rCBV	rCBF	MTT	MD (mm^2/s)	FA (0-1)
20	43	III	Anaplastic Astrocytoma	4.05	4.40	3.10	1.81	0.001297	0.070
21	28	III	Anaplastic Astrocytoma	6.13	6.63	9.86	1.40	0.001347	0.161
22	57	IV	GBM	4.32	1.70	2.43	2.16	0.000771	0.297
23	66	IV	GBM	8.17	3.82	4.33	1.57	0.001097	0.144
24	76	IV	GBM	5.40	5.97	2.76	1.25	0.000933	0.225
25	67	IV	GBM	4.58	3.44	3.26	1.25	0.001147	0.153
26	71	IV	GBM	6.33	4.52	4.94	2.79	0.000788	0.216
27	30	IV	GBM	7.94	3.38	8.97	1.59	0.0009	0.235
28	60	IV	GBM	5.35	2.40	9.09	1.96	0.001052	0.134
29	27	IV	GBM	5.20	4.76	16.33	2.20	0.002345	0.061
30	72	IV	GBM	4.96	2.96	3.78	1.74	0.001269	0.131
31	54	IV	GBM	4.25	2.54	3.49	2.29	0.001189	0.186
32	60	IV	GBM	5.59	3.68	4.56	1.50	0.001335	0.050
33	71	IV	GBM	2.61	3.45	4.35	0.98	0.001345	0.040
34	67	IV	ptxGBM	2.38	1.90	0.88	1.56	0.001568	0.185
35	73	IV	ptxGBM	2.41	1.88	0.11	2.14	0.001717	0.139
36	73	IV	ptxGBM	2.88	5.53	5.12	1.28	0.001854	0.029
37	65	IV	ptxGBM	2.26	0.99	0.77	0.65	0.000505	0.067
38	58	IV	ptxGBM	1.67	2.09	2.48	0.98	0.002019	0.042
39	65	IV	ptxGBM	2.03	3.52	4.46	1.94	0.001475	0.026

ID	Age	WHO Grade	Histological Type	Peak Values (Ratio)				Trough Values	
				MetPET	rCBV	rCBF	MTT	MD (mm^2/s)	FA (0-1)
40	45	IV	ptxGBM	4.17	4.87	2.30	0.94	0.00098	0.066
41	70	IV	ptxGBM	2.54	2.18	5.68	0.86	0.000646	0.003

* = 1p19q co-deleted, ***= 19q deleted 1p inconclusive, d* = delayed histological diagnosis (see text) *GBM* = Primary Glioblastoma Multiforme, *ptxGBM* = post-treatment Glioblastoma Multiforme (scans performed at least 3 months post-completion of Stupp protocol)

Participants without contemporary histological diagnosis: [1]radiologically stable lesion in eloquent location elected to continue surveillance imaging, [2]likely pilocytic astrocytoma in patient with neurofibromatosis type II, [3]initial biopsy inconclusive – histology confirmed on delayed re-do surgery, [4]previously operated low-grade astrocytoma with conclusive radiological features of progression elected to proceed direct to chemo-radiotherapy, [5]stereotactic biopsy (grade II astrocytoma) determined to be non-representative by MDT.

Neuropathological diagnoses were obtained in thirty-eight participants (88.3%) (see Table 5.1 above), conform with the molecular panel required for the WHO 2016 classification. For each patient IDH status and 1p/19q codeletion were assessed (in some cases restrospectively from tissue stored), and diagnosis was adjusted to the latest WHO classification. One participant had an initial inconclusive biopsy with WHO grade II features confirmed at later re-do surgery, one tissue sample was felt to be non-representative and the remaining three were not biopsied / re-biopsied after completion of their diagnostic investigations. Three participants had a period of surveillance between their initial investigations and proceeding to surgery (delay of 342-457 days) but all remained WHO grade II at the time of surgery and so these were not excluded from the analysis. Twenty patients were histologically confirmed GBMs WHO IV, of whom eight patients underwent PET and MR imaging at least 3 months after the completion of standard treatment (surgery and radio-chemotherapy protocol).

Follow-up data was recorded until radiological progression confirmed on the MDT discussion or the most recent stable MR scan on routine follow-up. One patient died of an early post-operative complication leaving 40 patients with a mean follow-up of 3.1 years. 9 patients underwent early radiotherapy and/or chemotherapy including 4

low-grade and 5 proven or suspected high-grade gliomas. Eleven of the 20 histologically confirmed high-grade tumours progressed during follow-up (with mean progression time 10.3 months). The remaining 20 grade II and III tumours underwent radiological surveillance with 13 patients demonstrating radiological progression (mean progression time 39.85 months) requiring further intervention within the duration of the study. Radiological progression was defined according to RANO criteria [130], following review of follow up MR images in the Neuro-oncology MDT.

Significant increasing methionine uptake was seen with increasing histological grade ($F=13.26$, $df=5$, $n=41$, $p<0.001$) (Figure 5.1). A trend of increased uptake was also noted in the oligodendroglial tumours compared to the same grade astrocytomas, although this failed to reach statistical significance ($F=2.198$, $df=1$, $n=12$, $p=0.46$). A similar pattern of increasing rCBV with increasing grade was also seen across the whole group of study, and in same grade astrocytomas compared to tumours with an oligodendroglial component but this was not significant.

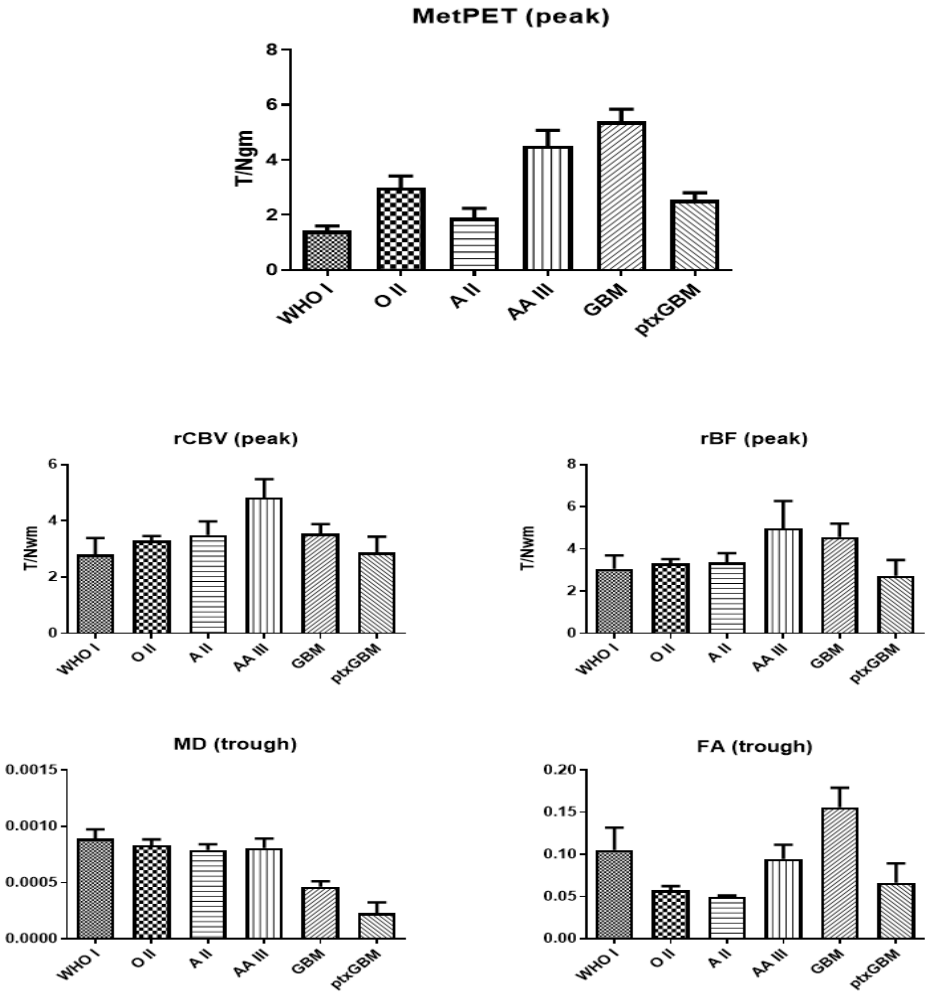

Figure 5.1 Peak and Trough mean values of MetPET and MR parameters according to histotype (O=Oligodendroglioma, A=Astrocytoma, AA=Anaplastic Astrocytoma, GBM=Glioblastoma Multiforme, ptxGBM=post-treatment Glioblastoma Multiforme).

In 24 patients that had radiologically progressed during the study time, 14 subjects had a peak MetPET ratio of 3 or above showing a significantly shorter progression time (two tailed t=2.63, p=0.015), despite differing histological grades. No significant correlation and no difference in the mean progression time were found when comparing patients with a peak rCBV above than 2. Review of the DTI data with respect to outcome yielded conflicting results, both tumours that progressed following adjuvant therapy and the tumour that remained stable without additional treatment all demonstrated low trough MD values. Although GBMs showed significantly lower trough MD values compared to the lower grade tumours (mean trough MD $1.247x10^{-3}$nvs $1.875x10^{-3}$ $mm^2.s^{-1}$, two-tailed unpaired t=4.47, p<0.001). MetPET remained the best predictor of outcome showing that survival rates were

inversely proportional to MePET updake. Patient's with MetPETpeak value above 3 were found to have the lowest progression free survival rates compared to the other groups with lower peak uptake values (Logrank X^2=13.79, p=0.002) (Figure 5.2).

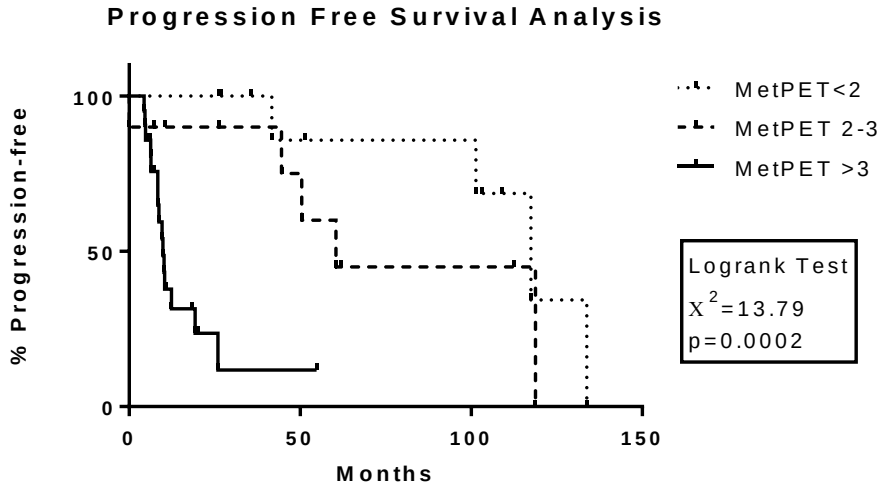

Figure 5.2 Kaplan-Meier progression-free estimates according to peak methionine uptake.

Significant positive linear and rank correlations were identified between peak methionine uptake ratios and peak values for both rCBV (Pearson's r=0.364, n=41, p=0.008, Spearman's ρ=0.413, n=41, p=0.004) and rCBF (Pearson's r=0.440, n=41, p=0.003, Spearman's ρ=0.285, n=41, p=0.036), as well as trough values for FA (Pearson's r=0.585, n=41, p<0.001, Spearman's ρ=0.585, n=41, p<0.001). Whilst for the trough MD, an inverse correlation was found in relation to the methionine uptake (Pearson's r=-0.463, n=41, p=0.001, Spearman's ρ=-0.482, n=41, p=0.001) (please see Table 5.2).

Table 5.2 Inter-modality correlation between peak uptake values for MetPET and DSC parameters and trough values for DTI parameters.

Comparator Modality	Correlation Statistic	rCBV	rCBF	MD (trough)	FA (trough)
MetPET	Pearson's (*r*)	.359** (p=0.008)	.440** (p=0.003)	-.463** (p=0.001)	.585** (p<0.001)
	Spearman's (ρ)	.413** (p=0.004)	.285* (p=0.036)	-.482** (p=0.001)	.524** (p<0.001)
rCBV	Pearson's (*r*)		.445** (p=0.002)	-.117	-.020
	Spearman's (ρ)		.480** (p=0.001)	.081	-.037
rCBF	Pearson's (*r*)			-.125	.126
	Spearman's (ρ)			-.047	-.066
MD (trough)	Pearson's (*r*)				-.510** (p<0.001)
	Spearman's (ρ)				-.515** (p<0.001)

Pearson's product moment and Spearman's rank correlation coefficients and p-values (1-tailed). [* = p<0.05, ** = p<0.01]

On group analysis, the correlation with rCBV is maintained for oligodendrogliomas (*r*=0.694, n=7, p=0.02) but is lost for diffuse and anaplastic astrocytomas (*r*=0.359, n=10, p=0.07), and treatment naïve or post-Stupp protocol GBMs (*r*=0.158, n=20, p=0.08) (Figure 5.3). The correlation between peak MetPET ratio and trough FA also varies with histological type (p=0.0076 and 0.16 for astrocytomas and oligodendrogliomas respectively). Whereas no significant difference was found between the correlation of trough MD and MetPET peak values, which remained significant in all the different histological groups.

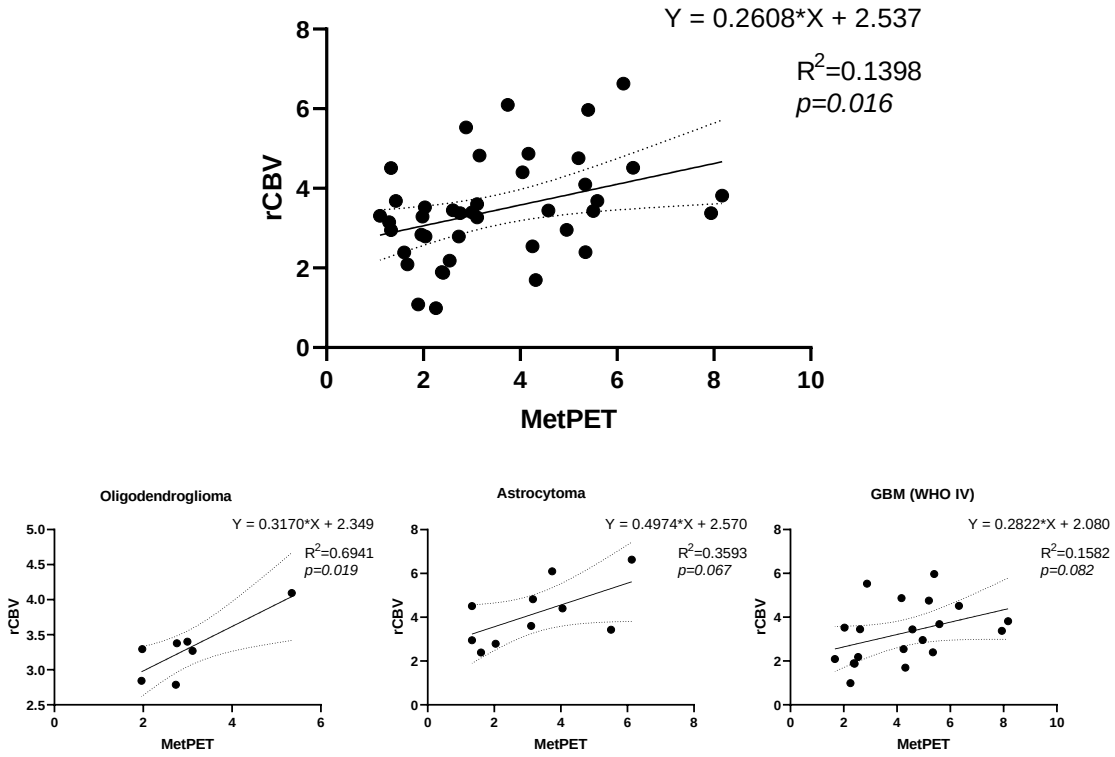

Figure 5.3 Peak MetPET and rCBV correlation in the different grades and types.

The median distance between MetPET and rCBV peak uptake VOIs was 15.1mm (standard deviation = 10.09, range = 1.0-34.9mm). Median distances between the trough MD VOI and peak MetPET and rCBV were slightly greater at 16.7 and 20.8mm respectively (Table 5.3).

Table 5.3 Distances between peak and trough uptake VOIs.

Comparator Modality	rCBV	rCBF	MD (trough)	FA (trough)
MetPET	15.1	16.55	16.67	17.35
	[1.0-34.93]	[1.1-53.27]	[1.0-52.24]	[3.16-54.27]
rCBV		4.9	20.8	14.2
		[1.0-51.9]	[3.2-35.2]	[3.3-46.5]
rCBF			21.9	13.6
			[1.4-47.5]	[1.0-42.0]
MD (trough)				17.4
				[1.0-39.7]

Distances presented as median and range in millimeters (n=41).

Table 5.4 Distances between peak rCBV and MetPET VOIs according to histotype group.

Comparator Modality	WHO I	O II	A II	A III	GBM	ptxGBM
Median	24.44	20.81	15.13	17.49	8.09	18.71
Mean	21.52	18.96	11.33	14.25	10.84	15.33
Range	10.05-33.17	4.24-34.93	1.0-19.72	1.0-25.26	1.22-27.86	2.23-25.85

Distances presented as median and range in millimeters (n=41).

High inter-subject variability was seen for all of the distance measurements with a mean coefficient of variance of 62.6% across the 10 comparisons (range 37.2-98.3%). More than half of the measured distances between peak and trough VOIs (163/287, 56.8%) were greater than 15mm making them clinically relevant differences in the context of biopsy and intervention targeting (Figure 5.4). Higher grade, treatment naïve tumours with higher peak values for both MetPET and rCBV, particularly where neither peak value was less than 3, demonstrated lower variability and significantly smaller distances between peak uptake VOIs (Mann Whitney U p=0.005, see Table 5.4 and Figure 5.5).

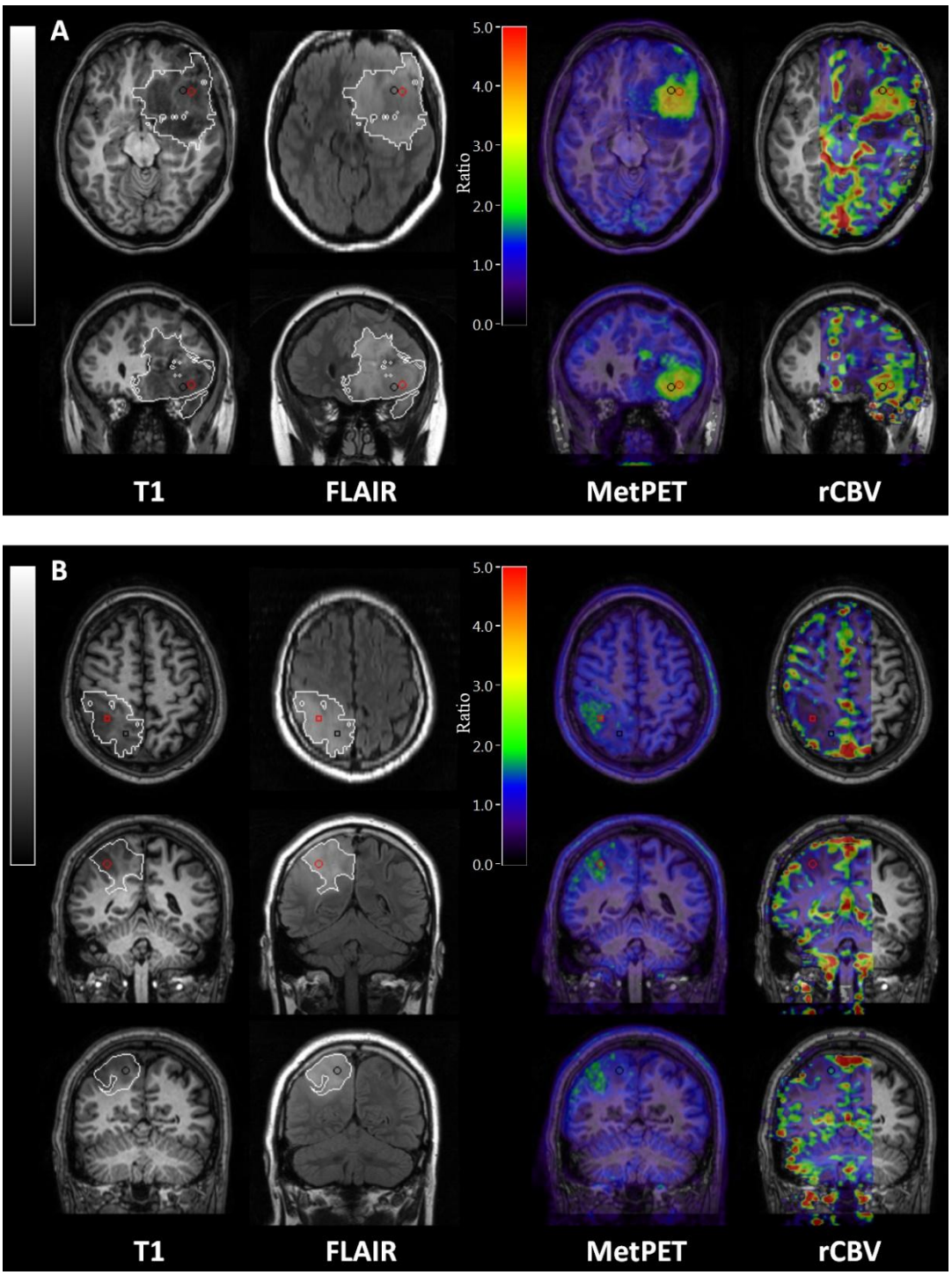

Figure 5.4 Different locations within the FLAIR delineated tumour mask of the peak MetPET (red) and rCBV (blue) VOIs. A. Axial (top row) and coronal sections of a subject with anaplastic astrocytic glioma, (from left to right) T1, FLAIR, fused T1/MetPET and T1/rCBV registered maps with the tumour mask delineated in white showing closer proximity of peak MetPET (red) to peak rCBV (blue) in comparison to the lower grade oligodendroglioma in B. (top row) Axial views of T1, FLAIR, fused T1/MetPET and T1/rCBV of a patient with oligodendroglioma 1p/19q codeleted showing the peak MetPET (red) and rCBV (blue) within the tumour mask in white. As noted in same patient's coronal views peak MetPET and rCBV are clearly apart not correlating in either values or localisation.

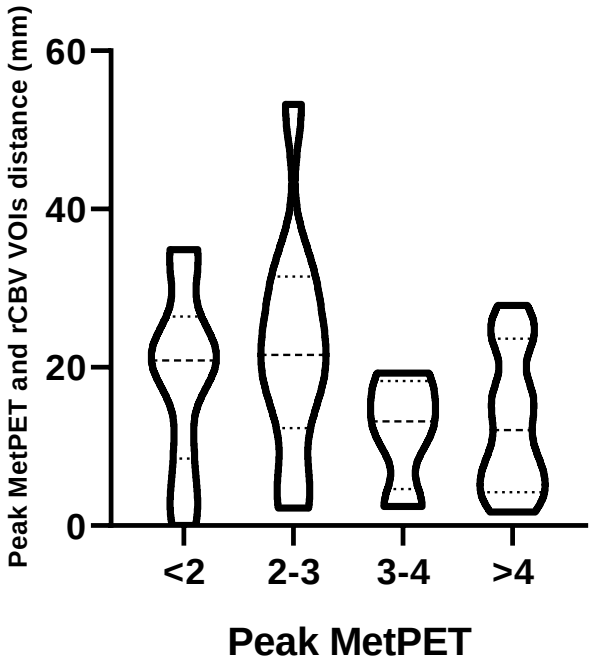

Figure 5.5 Violin chart showing mean distances of peak rCBV and peak MetPET VOIs stratified by their tracer uptake.

Smoothed time-activity curves (TACs) of methionine uptake showed a significant difference between the Peak MetPET and rCBV VOIs in the oligodendroglial tumours (comparison of Savitzky–Golay smoothed mean TACs slopes F=10.32, p=0.029), but despite the different morphologies the smoothed TACs did not differ in the astrocytic and GMB groups (Figure 5.6).

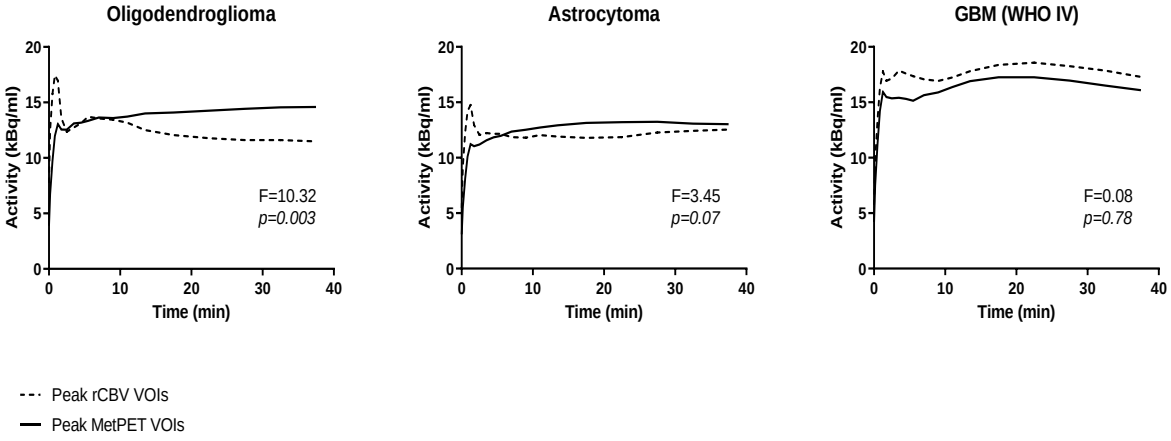

Figure 5.6 Savitzky–Golay smoothed TACs of the peak rCBV compared to the peak MeTPET VOIs.

5.5 Discussion

Several neuroimaging techniques have demonstrable benefit at different points in the treatment pathway for patients with primary brain tumours but as yet no single approach can answer all clinical questions. Improved understanding of tumour biology and the introduction of novel therapeutic targets also means that the demands placed upon neuroimaging are likely to continue to increase over time. This study was designed to investigate the relationship between the results obtained with currently available techniques at a spatial resolution appropriate to imaging the intratumoural distribution of tracer uptake and of MRI derived measurements. PET with amino acid tracers and MetPET in particular have a substantial evidence base in the context of gliomas [80, 139]. However, the resolution of all but the most recent clinical PET scanners is an order of magnitude lower than that of the HRRT limiting the ability of previous studies to account for intratumoural heterogeneity. This study demonstrates increasing methionine uptake with tumour grade, confounded to an extent by overlap between high-grade astrocytic and low-grade oligodendroglial tumours as previously described. However, it provides novel details on how these MetPET results relate to MRI parameters in the same patients and in particular details variation in the spatial co-localization of PET and MRI findings.

A significant inter-modality correlation was identified between peak methionine uptake and rCBV for oligodendrogliomas (r=0.83). This is in-keeping with previous studies suggesting that results for both modalities are correlated with microvessel density [32, 93]. Although this correlation also reached statistical significance for the whole group (r=0.36), that was not the case for the purely astrocytic tumours (r=0.28). Additionally, the oligodendrogliomas showed a significantly different TAC of the regions with peak rCBV and MetPET uptake. Previous studies have confirmed histologically that microvessel density is greater in low-grade oligodendroglial tumours than in astrocytomas [161] suggesting a morphological difference underlying the imaging finding. However, in contrast to earlier studies suggesting an association between methionine uptake and microvessel density for all gliomas, MetPET has also been shown to correlate with tumour cell density or proliferation rates in astrocytomas in studies that segregated histological types [161] or recruited

only astrocytic and mixed tumours [158]. The finding of a difference in the relationship between MetPET and rCBV in tumours of different histological types in this study would suggest that the predominant pathological change influencing MetPET uptake also differs between types being more dependent upon vascular proliferation in oligodendrogliomas. Overlap between the typical findings for low-grade oligodendrogliomas and high-grade astrocytic tumours is a major limitation upon the interpretation of MetPET findings in a newly diagnosed tumour. Adding data with respect to whether the methionine uptake is in concordance with the rCBV of the tumour may give an indication as to the histological type and provide an opportunity to facilitate this interpretation.

Disparity between the findings for rCBV and MetPET in astrocytomas is further highlighted with the apparent loss from the rCBV data of the trend towards rising peak values with histological grade that is seen in the methionine results. Another recent study of DSC and DTI in gliomas also reported very similar peak rCBV values for grade II and III astrocytomas but noted that ADC was conversely more effective at segregating low-grade and anaplastic astrocytomas than oligodendrogliomas [162]. The authors proposed that non-invasive grading could therefore be improved by incorporating both peak rCBV and trough ADC results. We have demonstrated an inverse correlation between MD (equivalent to ADC) with PET peak values ($r=-0.46$, $p=0.001$). This correlation was again notably diminished in astrocytomas where rCBV appears to be less discriminatory. The changing relationship between the PET, perfusion and diffusion findings with histological type reflects differences in the efficacy of the different modalities in characterizing tumours of different types. This supports multi-modal approaches that incorporate rCBV and either DTI or amino acid PET, particularly for tumours at presentation where the histology is not known. It may then be possible to rationalize the choice of modality used for surveillance imaging once the histology is known. The different location of peak and trough ROIs of each modality reflects also possible underlying different pathological processes or cellular subgroups.

The distances between the locations of the peak and trough VOIs within the current study are significant in the context of understanding how the selection of imaging modality impacts upon treatment planning. Commercial neuro-navigation systems such as that employed in the current study can achieve accuracy in target delineation

for biopsy planning in clinical practice of better than 5mm [163] and in laboratory studies targeting errors of less than 1mm are achievable [164]. Despite the strong correlation between peak MetPET and rCBV ratios, the distances between the locations of the peak uptake VOIs are more than double the reasonably achievable accuracy of tissue sampling such that effectively different biopsy targets would be defined depending upon which modality is used for targeting. The measured distances are not directly dependent upon histological type but are influenced by the absolute peak uptake values with significantly smaller inter-modality distances and lower variability being recorded for tumours in which both the peak MetPET and rCBV ratios are greater than 2. This suggests that in high-grade tumours MetPET and rCBV are more likely to yield concordant biopsy targets than in low-grade or low uptake tumours. Given the limited availability and cost of amino acid PET this is of relevance in defining the cases in which it is most likely to result in a direct change in the treatment plan.

This study employed an automated system for positioning of the peak and trough uptake VOIs within a manually outlined tumour volume in an effort to minimize operator bias and improve reproducibility. The relative ease with which this approach can be applied has some dependence upon the characteristics of the different imaging modalities and of the individual tumour. MetPET is well suited to tumour delineation, with the majority of even low-grade gliomas demonstrating increased methionine uptake the algorithm is required to find only the region of highest uptake with little confounding data. The images can also be analyzed by comparison to population normal data to account for inherent variability in uptake according to anatomical location to further facilitate this process although with a risk of introducing errors in susceptible locations depending upon the registration process employed [165]. Identifying peak rCBV is complicated by the presence of vessels within or adjacent to the tumour VOI and the potential for relatively normal cortex at the edge of the VOI to have a higher rCBV than a low-grade tumour. The effect of the periphery of the VOI is also particularly important in the identification of trough VOIs for the DTI measures where the most restricted diffusion can otherwise be seen in relatively normal brain. Exclusion of large vessels from the tumour VOI has been previously demonstrated to increase the discriminatory power of rCBV [151] with several methods employed to achieve this including manual exclusion of vessels [166], multi-parameter segmentation [167] and blood flow based methods

such as that employed in this study which has previously been utilized to investigate correlation of MRI and nuclear medicine perfusion measurements [160]. This was augmented in the current study by erosion of the tumour VOI to minimize any influence from peri-vascular tissue and relatively normal brain at the edges of the VOI particularly for the MD images. These measures minimize potential confounding effects on VOI placement for the MRI derived parameters although the PET data remains the most technically straightforward to employ automated techniques to segment abnormal regions.

This study presents prospectively acquired high resolution multi-modal imaging data in a cohort of gliomas that is intended to represent a "real-world" group of consecutive patients with suspected low-grade or transforming gliomas. It is limited primarily by the sample size and the multiplicity of tumour types recruited. The follow-up data enables confirmation that the tumours behaved phenotypically in accordance with the histological diagnoses and helps to exclude sampling errors beyond the case identified. None of the measured parameters were directly predictive of time to progression although the tumours with the highest methionine uptake (>3.0x normal appearing cortex) progressed despite adjuvant therapy and those with the lowest peak rCBV (<1.6x normal appearing white matter) remained stable with or without additional treatments. This lack of predictive value in time to progression may be influenced by the very marked effect of early radiotherapy with 3/5 high-grade tumours remaining stable after adjuvant therapy as compared to only 1/6 low-grade tumours managed with surgical resection alone. None of the 5 grade II tumours receiving early adjuvant therapy showed features of progression within the study period (mean follow-up 3.9 years).

5.6 Conclusion

None of the currently available diagnostic neuro-imaging modalities in isolation can comprehensively characterize and grade a suspected glioma at presentation although the use of multimodal techniques has advantages upon standard clinical approaches. Our study proved highly significant overall correspondence between amino acid uptake and rCBV as measured with DSC-MRI. However, correspondence of the

location of the respective maxima was highly variable, suggesting that DSC-MRI cannot currently replace amino acid PET particularly in low-grade or low-uptake tumours. Multimodal imaging studies with targeted biopsies and assessment of local vascularity and cellularity are required to ultimately clarify the differences and provide the basis for comprehensive non-invasive tumour characterization.

Funding

This work was supported in part by a grant from the Oglesby Charitable Trust.

Acknowledgments

The authors thank Jose Anton-Rodriguez and Julian Matthews for their assistance with reconstruction of the PET images and PET methodology support.

Blank page

Chapter 6 – Normal brain structures show widespread microglial activation in patients with gliomas

6.1 Abstract

Introduction: Animal and human post-mortem studies have demonstrated activated microglia both within gliomas and, interestingly, in the normal brain tissue remote from the tumours. Translocator protein (TSPO) is over-expressed mainly in activated microglia under disease conditions. Previously we have found upregulated TSPO in neoplastic cells and its correlation with malignant transformation in human gliomas. In this study we investigated the level and extent of TSPO expression and microglial activation *in vivo* in normal-appearing brain structures of patients with different types of brain tumours.

Methods: 93 patients with brain tumours and 19 controls were examined using positron emission tomography (PET) with [^{11}C]-(*R*)PK11195 to assess TSPO expression as a marker of microglial activation. Diagnosis was confirmed by *post hoc* tumour biopsy and/or resection. Binding potential (BP_{ND}) of [11C]-(R)PK11195 was calculated using the simplified reference tissue model and correlated to cerebellar SUV derived from 10-60 minutes summed images. BP_{ND} of normal-appearing brain in patients was compared with controls. Post-mortem brains with treatment-naive low-grade glioma were assessed for TSPO and microglia in normal-appearing brain tissue by immunohistochemistry.

Results: We found increased microglial activation, in both cerebral hemispheres (tumour regions excluded) in glioma patients compared to controls. This was most prominent in the tumour-bearing hemisphere ($p<0.0001$) but was also evident in the controlateral hemisphere ($p=0.0078$). Interestingly the metastasis group showed in both hemispheres significantly lower uptake values compared to the controls and other groups. Patients presenting with epileptic seizures (n=38) showed a positive correlation between extra-tumoural microglial activation in the cerebrum and the duration of epilepsy ($\rho=0.0194$ ipsilateral hemisphere and $\rho=0.0108$ controlateral). No significant correlation was found between the cerebellar SUVs and BP values. Post-mortem brain tissue showed a 10-fold increase in microglia and elevation in TSPO-expressing microglia in the gyri adjacent to the tumour and in the tissue of controlateral hemisphere compared with normal brains.

Conclusion: [^{11}C]-(*R*)PK11195 PET demonstrates widespread microglial activation in normal-appearing cerebral structures of patients with high- and low-grade gliomas whilst a suppression was noticed on the metastasis group. The magnitude of activation correlates with the duration and type of epilepsy, suggesting that modulation of microglial activation could represent a novel potential target for seizure control in this patient group. TSPO PET provides an in-vivo demonstration of this inflammatory response, which is undetectable by structural MRI.

6.2 Introduction

In the previous two chapters we studied gliomas with a multi-tracer approach correlating to perfusion and diffusion MR imaging. During our analysis as well in the previous work from our group [149], we noticed an increased uptake in areas distant from the tumour, in multiple occasions going beyond the ipsilateral hemisphere where tumour was located. According to our knowledge there have not been any previous studies, focused on the normal appearing brain and how the tumour affects the brain as a whole. Our hypothesis was that a degree of neuro-inflammation might have been triggered by the tumour or its microenvironment. Hence, in this chapter we decided to investigate further the increased inflammation in the normal appearing brain in glioma, comparing to a diseased control group (secondary metastatic lesions or vestibular schwanommas) and a healthy control group.

Gliomas account for approximately 75% of primary intrinsic brain tumours in adults [1]. They are associated with a high mortality rate and the highest individual cancer burden (average years of life lost) compared with other cancers [168]. This results from the relatively young onset of the disease, the invasive growth pattern of the tumour, and the resistance to existing therapies.

Several neuroimaging studies have investigated in detail the patterns of glioma infiltration [169-171]. In contrast, only one post-mortem study examined the involvement of the whole brain in subjects with diffuse glioma [172]. Using whole brain coronal sections of four subjects with $IDH1^{R132H}$ mutant anaplastic diffuse gliomas (aDGs) they found single or small clusters of tumour cells in normal appearing areas that otherwise showed normal cellularity. It has long been known that gliomas are infiltrative lesions with indistinct borders from the surrounding brain. Before the discovery of IDH1/2 mutations as the hallmark of 80% of aDGs and the introduction of the specific antibody to detect the mutant R132H protein in tissue, the assessment of the extent of infiltration was based on neuroimaging features. The possibility to discriminate isolated or small groups of neoplastic cells from reactive of normal glial cells allows now for an accurate microscopic assessment of infiltration and multifocality. Nevertheless, gliomas can impair the normal brain connectivity in areas distant from the tumour epicentre suggesting widespread involvement irrespective of the extent of invasion [173].

Microglial cells are the main effectors of the brain immune system. In the normal brain, they form a network of surveillance that responds to any insult to the tissue, with their cytoplasmic processes continuously scanning the surrounding microenvironment [174]. Upon detection of biochemical changes, they undergo morphological, molecular and functional changes (activation) that result in the synthesis of a myriad of pro-inflammatory molecules, including the translocator protein 18 kDa (TSPO) [56]. This process mainly localises to the site of pathology, but also occurs along the anatomically connected anterograde and retrograde axonal pathways [58]. Microglial activation is commonly seen in gliomas, and the extent of microglial infiltrate increases with the grade of malignancy [65, 175, 176]. Studies using rodent glioma models documented an increase of activated microglia not only within tumour tissue and its periphery but also in the controlateral hemisphere [100, 177]. This evidence suggests that the neuro-inflammatory response is not restricted to the tumour itself but can involve the whole brain.

Positron emission tomography (PET) is widely used to image microglial activation *in vivo* with ligands that selectively target the TSPO. In particular, [^{11}C]-(*R*)PK11195 is commonly utilised in acute and chronic neurological disorders [58, 178-180], because of its elevated binding in areas of neuroinflammation and only minimal binding in healthy brain. Hitherto, a few TSPO PET studies have been performed in a small number of glioma patients [181-186], and none of them investigated microglial activation outside the tumours. Previously we have reported the methodology validation of [^{11}C]-(*R*)PK11195 PET as well as its application in glioma patients [65, 119], and also documented the preliminary finding of increased microglial activation in normal-appearing brain structures of patients with low-grade gliomas [149]. In the current study we sought to characterise this neuroinflammatory response in a larger population of patients with brain tumours, specifically investigating normal-appearing brain structures.

6.3 Methods

6.3.1 Participants

Glioma Cohort

With the aim to investigate the neuroinflammation in the ipsi- and controlateral normal-appearing brain regions, we analysed the datasets obtained from 66 patients with different histotype gliomas (mean age 47.8 years, age range 19-76 years, with a prevalence of the male gender M/F=43/23; demographic, imaging and medical history summarized in Table 6.1). The glioma cohort included 25 diffuse glioma WHO grade II, 9 anaplastic WHO grade III gliomas and 32 WHO grade IV gliomas (10 patients with WHO IV glioblastoma were scanned at least 3 months post their standard Stupp protocol treatment following surgery). Twenty-seven patients were on Dexamethasone, but this medication had been discontinued in three of them for at least two weeks prior to the PET scanning. Clinical information was obtained via clinical interview and case note review. None of the patients were treated with benzodiazepines.

The subjects for this cohort were recruited through two different studies approved by the University of Manchester, Wrightington, Wigan and Leigh (reference 109/H1014/41), and Greater Manchester South Ethics Committees (reference 16/NW/0548). Permission to administer radioisotopes was granted for all the studies by the Administration of Radioactive Substances Advisory Committee (ARSAC) of the Department of Health, UK.

Disease Control Cohort

As disease controls, we included 19 patients with vestibular schwannoma and 8 with brain metastasis (Table 6.2 and 6.3). Mean age for the VS patients was 57.8 years(range 26 -81), F/M=11/8. For the metastasis group mean age was 63.1 years (range 47-71), F/M=5/3. Two of the eight patients with brain metastasis were on systemic treatment for their primary disease, patient 67 treated with immunotherapy for metastatic melanoma and patient 74 on chemotherapy for triple negative breast adenocarcinoma.

These studies were approved by Central Manchester (reference 14/NW/0071) and West Manchester (reference 14/NW/0429) Ethics Committees, in addition to the University of Manchester Ethics Committee. Permission to administer radioisotopes was granted for both studies by the Administration of Radioactive Substances Advisory Committee (ARSAC) of the Department of Health, UK.

Healthy Control Cohort

Nineteen healthy volunteers (mean age 44.6 ys, age range 20-72 ys, M/F=10/9) were also scanned (Table 6.4). Written informed consent was obtained from all participants.

The study was approved by the West Manchester (reference 14/NW/1255), and the University of Manchester Ethics Committees. Permission to administer radioisotopes was granted by the Administration of Radioactive Substances Advisory Committee (ARSAC) of the Department of Health, UK.

6.3.2 Image acquisition and processing

All subjects underwent a structural MRI scan on 3·0 Tesla or 1·5 Tesla scanners (Philips Achieva, Philips Medical System, Best, NL) for diagnostic classification and co-registration purposes within one month prior to the PET. Dynamic PET scans were acquired on the High Resolution Research Tomograph (HRRT, Siemens/CTI, Knoxville, TE, US) at the Wolfson Molecular Imaging Centre, University of Manchester. In brief, a 7-min transmission scan using a ^{137}Cs point source was acquired for subsequent attenuation and scatter correction. After the start of the emission scan, [^{11}C]-(*R*)PK11195 was injected intravenously as a slow bolus over approximately 15 seconds. The injected dose was 631.6±131MBq, with a target radioactivity of 740MBq. Radiochemical purity was always greater than 97%. Emission data were then acquired over 60 min as 18 frames (one background frame of variable length, followed by 1×15s, 1×5s, 1×10s, 1×30s, 4×60s, 7×300s and 2×600s frames) and reconstructed using an ultra-fast iterative ordered-subset expectation maximisation (OSEM) 3D method [187]. Parametric maps of binding potential (BP_{ND}, representing the ratio of specifically bound radioligands over non-displaceable ones in tissue at

equilibrium) were calculated using the simplified reference tissue model (SRTM) [117] with the cerebellar cortex as the reference tissue input function [58].

After the reconstruction of PET images, individual MRI was co-registered to the summed PET image, and the T1-weighted inversion recovery images were segmented into grey matter and white matter probability maps. The inverse transformation parameters from segmentation were used to warp a maximum probability brain atlas [188] into individual space. The quality of co-registration, segmentation and individualised normalisation was visually inspected. On observation, the warped brain atlas was distorted regionally in the tumours and their margin as expected, but matched the extra-tumoural structures well, especially in the cerebral hemispheres controlateral to the tumours and in the cerebellum. Mismatch in normal structures was manually edited. Each tumour (including visible oedema, if present) was manually delineated using the co-registered T2- and T1-weighted MRI, and mirrored to the un-affected hemisphere. They were applied to the brain atlas for masking out the tumour and its mirror region when necessary. The individualised brain atlas, was used to derive the cerebellar GM input function in order to generate the BP_{ND} parametric maps. WM and GM segmentation maps together with the tumour and tumour mirror masks, were projected to the BP_{ND} parametric map for sampling regional BP_{ND} values (Figure 6.1). Due to the different location and size of each tumour, we focused our extra-tumoural analysis on the cerebral hemispheres and the entire forebrain rather than specific regions defined by the atlas. Therefore, all non-tumour regions belonging to each hemisphere or the forebrain were combined, and a weighted mean BP_{ND} was calculated. Cerebellar SUVs were calculated from the summed add images from 10 to 60 minutes of the emission scan [189]. Cerebellar SUVs values were correlated to the normal appearing brain tracer uptake to search for any possible correlation or implications affecting the cerebellar GM SRTM generated BPND maps. This analysis was also performed in the healthy control cohort. Cerebellar TSPO could be affected by whole brain neuro-inflammation but also by age and other conditions like depression or diabetes[150, 190]. Patients presenting with seizures were classified according to the latest classification from the International League Against Epilepsy according to their clinical notes and Epilepsy Clinic reviews [191]. Good epilepsy control was defined as complete seizure control for at least 6 months. Seizure duration was calculated in months from the first seizure onset to the most recent clinical follow up.

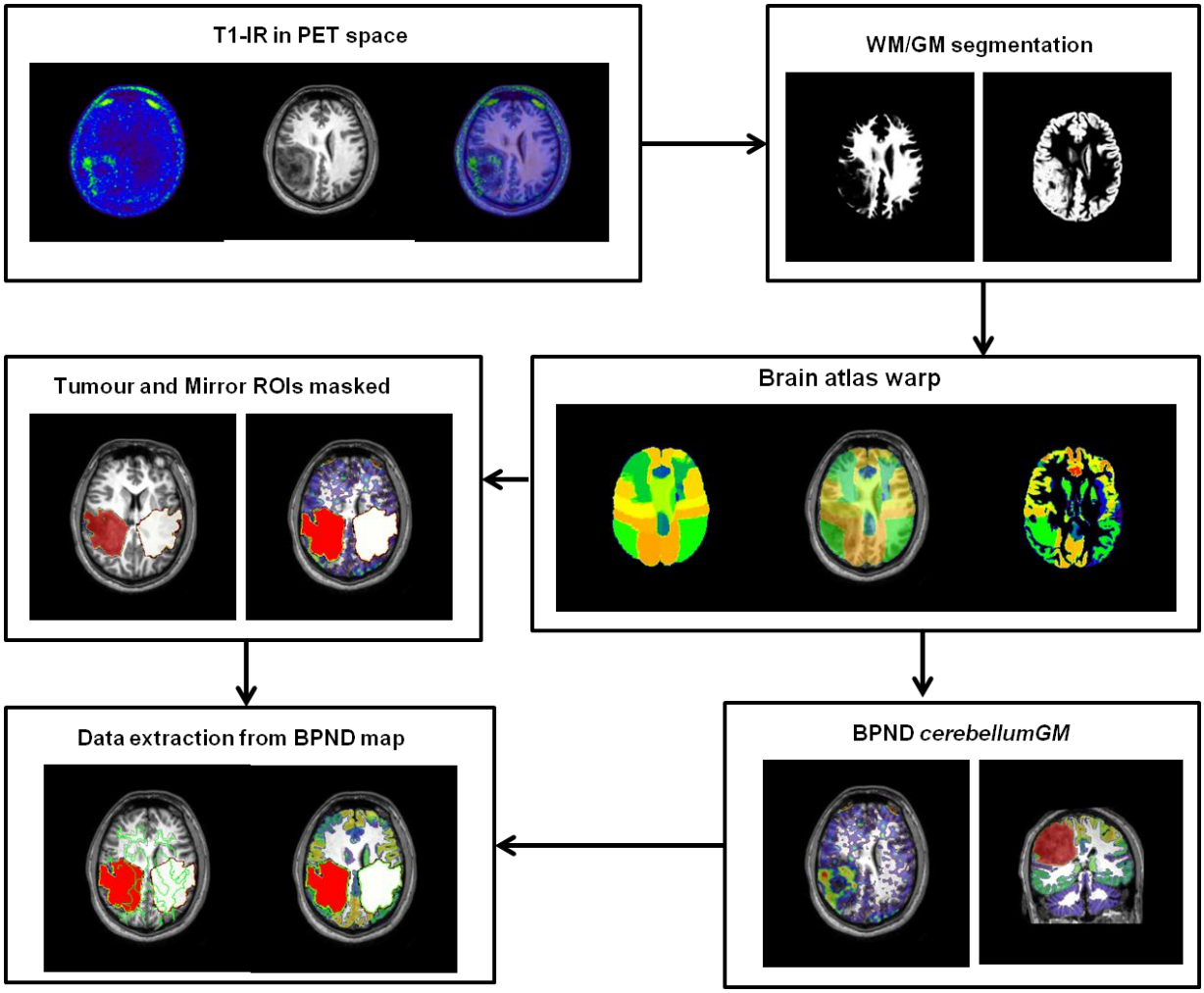

Figure 6.1 Flowchart representing image processing. Initially T1-Inversed Recovery images were registered in PET space with a rigid coregistration in FSL, WM/GM segmentation was performed consecutively in SPM. Hammersmith brain atlas regions were warped in individual space and applied to the WM/GM probability masks generated earlier. Cerebellum GM was used to extract input function for the BPND parametric maps, in parallel tumour and mirror mask were generated and excluded from the WM/GM masks in order to extract the statistics of each hemisphere's WM and GM normal appearing brain.

6.3.3 Statistical analysis

All data are expressed as Mean ± one Standard Deviation (SD). BP_{ND} of normal-appearing cerebral structures was compared with controls (average BP_{ND} in homologous structures of both hemispheres) using the Wilcoxon rank sum test with the p plot graphical method [192] to correct for multiple comparisons. The comparison between ipsilateral and controlateral hemispheres in patients was conducted using the Wilcoxon signed-rank test. Further comparisons of the mean uptake between the different histotypes and patient groups were performed using one-way Anova test with Dunett's correction for multiple comparisons. Correlations

of BP_{ND} with clinical parameters and cerebellar SUVs were assessed using the Spearman rank correlation coefficient. A probability of $p<0.05$ was considered statistically significant.

6.3.4 Examination of post-mortem brains

Three post-mortem brains of treatment-naïve patients (two males and one female, aged 30, 30 and 35 years) with temporal WHO grade $IDH1^{R132H}$ mutant oligodendroglioma (one patient) and astrocytoma (two patients) were identified among over 64,000 cases available in the MRC BrainUK database [193].

For each tumour case, macrosections from the right and left temporal lobe including hippocampus, and the frontal, parietal and occipital lobes were examined. Five aged matched control brains in patients without neurological diseases were obtained from the Semmelwise Brain Tissue Bank in Budapest, Hungary [194]. For control brains, small sections from the same regions as tumour brains were available. Regions distant from the tumour were selected and evaluated with $IDH1^{R132H}$ to exclude any possible distant tumour microinfiltration. Microglial and TSPO expression were evaluated as an indirect marker of neuroinflammation with antibodies agains Iba1 and TSPO respectively.

The sections of both tumour and normal brains were stained with haematoxylin-eosin. Immunohistochemistry was performed on the macrosections using antibodies directed against $IDH1^{R132H}$ (Dianova, Germany, monoclonal H09, dilution 1:200), Iba1 (WAKO, Neuss, Germany, polyclonal rabbit anti-Iba1, dilution 1:500), NeuN (Millipore, monoclonal, MAB377, 1:500) and TSPO (Abnova, goat polyclonal; dilution 1:500). The sections were deparaffinised in xylene3 x 10 min, 2 x 10 min in 100 Ethanol, 5 min in 90% ethanol, 5 min in 70% ethanol and 2 x 10 min in water. For antigen retrieval, the sections were immersed 20 minutes in steam heated sodium citrate buffer (10mM Sodium Citrate, 0.05% Tween 20, pH 6). Sections for NeuN immunostain were incubated in 1mM EDTA at pH8. Quenching of endogenous peroxidase was performed in PBS and 1% hydrogen peroxide for 15min. The sections were thereafter incubated with the primary antibody overnight. After incubation with the primary antibody, the sections were carefully washed in PBS and then incubated with the SuperSentitive IHC detection system from BioGenex (Fremon, CA, USA) following the manufacturer's instructions. Nuclear counterstaining was performed

with Mayer's Haemalum. Finally, the sections were dehydrated and coverslipped. Immunoreactions with omission of the primary antibody were performed as negative controls and positive control were included in each batch.

6.3.5 Quantification on tissue sections

For the quantification of $IDH1^{R132H}$ positive neoplastic cells, TSPO positive cells Iba1-positive GAMMs, five random images were captured with a x20 objective using a Nikon SMZ microscope (Nikon UK, Kingston upon Thames), a QImaging micropublisher 3.3 RTV camera and the QCapture Pro software (Version 6.0.0.412). For the grey matter, the field of focus was aimed in layer IV and a series of consequential images around a gyrus or a sulcus were taken (15-25 fields with equal number on either side) and a series of 10 images of the adjacent white matter. For the macrosections of the temporal lobe, a series of images were taken counter clockwise in the grey matter around the superior, medial and inferior/fusiform gyri. For the white matter each white matter gyri including the temporal lobe stem were counted separately. Counts were performed using the Kurt de vos cell counter within the Image J program [195]. Only Iba1 positive cells bodies with at least one process were considered. Density of microglia was used rather than the average of a region of interest and the density was determined by dividing the number of cells with the total area of visual fields [196]. Counting of a series of random pictures were duplicated by a second observer and correlated. Microglia density was determined for each case (n = 20), disease (n = 5), brain region (n = 4) and grey and white matter (n = 2). A final mean of microglia density (s.e.m) was given for each condition and for each brain region.

6.4 Results

Clinical data and individual [^{11}C]-(*R*)PK11195 BP_{ND} in the non-tumoural regions of the entire forebrain and cerebellar SUVs are summarised in Table 6.1 for patients

with glioma, Table 6.2 patients with brain metastasis, Table 6.3 VS patients and Table 6.4 for healthy controls cohort.

After excluding the tumour region, increased extra-tumoural [^{11}C]-(*R*)PK11195 binding was revealed in the ipsilateral hemisphere of the patients with glioma when compared with controls (0.06110 ± 0.009826 N=66 vs. -0.01582 ± 0.01553 N=19, $p<0.001$; this remained significant after correction for multiple comparisons; Figure 6.2).

Vestibular schwannomas and mestastasis showed no difference in the ipsilateral hemisphere uptake compared to the controls, although the metastatic patients had consistently negative values except from the 2 patients on systemic treatment for their primary disease (patient 67 and 74). A similar pattern of increased [11C]-PK11195 uptake in glioma patients was present in the controlateral hemisphere when comparing to the whole brain of the controls (0.02954 ± 0.008613 N=66 vs. -0.01582 ± 0.01553 N=19, p=0.0071, Figure 6.1), but also in Vestibular Schwannomas (0.02784 ± 0.01048 N=19 vs. -0.01582 ± 0.01553 N=19, p=0.0127).

Table 6.1 Demographic, clinical and imaging data of subjects with different histotype gliomas.

ID	*Diagnosis*	*Gender*	*Age*	$BPND_{ipsi}$	$BPND_{contro}$	$SUV_{cerebellum}$	*Comorbidities*
1	A II	F	25	0.019463	-0.01175	0.54	Nil
2	A II	M	33	0.089309	0.073172	0.86	Nil
3	A II	F	47	0.20726	0.183904	0.84	Nil
4	A II	M	33	0.030467	0.045633	0.98	Nil
5	A II	M	42	0.042377	0.024156	0.6	Nil
6	A II	F	40	0.089554	0.06687	0.41	Nil
7	A II	M	38	0.008227	-0.00587	0.59	Nil
8	A II	M	32	0.010097	0.020765	0.86	Nil
9	A II	M	36	-0.0356	-0.062	0.86	Nil
10	O II	M	41	0.062304	0.012314	0.71	Nil
11	O II	M	45	0.141081	0.123332	1.45	Nil
12	O II	F	24	0.054454	-0.03181	0.63	Nil
13	O II	M	40	0.200664	0.146961	0.5	Nil
14	O II	M	30	0.052369	0.037495	0.45	Nil
15	O II	M	24	0.033554	0.011417	0.66	Nil
16	O II	F	50	0.074614	0.033804		Nil
17	O II	F	52	0.042058	0.024429	0.79	Nil
18	O II	M	37	-0.06233	-0.04601	1.38	Nil
19	O II	F	48	-0.11235	-0.1116	0.59	Nil
20	O II	F	45	0.016142	-0.02947	0.63	HTN, DM II
21	O II	M	46	0.174924	0.13713	0.58	Personality disorder
22	O II	M	49	-0.04444	-0.04318	1.92	HTN
23	AA III	M	37	0.234815	0.177372	0.91	Nil
24	AA III	F	63	0.061716	0.012734	0.74	Nil
25	AA III	M	42	0.002961	-0.00596	1.08	Nil
26	AA III	M	46	0.09491	0.092395	0.62	Nil
27	AA III	F	54	0.022347	-0.01117	0.67	Nil
28	AA III	M	19	0.045922	-0.01287	1.21	Nil
29	AA III	M	43	0.140519	0.052349	0.62	Orchidectomy
30	AA III	M	63	0.011344	0.015457	0.76	HTN
31	AO III	M	22	0.039322	0.009155	0.79	Nil
32	AO III	M	24	0.082589	0.056344	1.05	Nil
33	AO III	M	24	0.095719	0.136779	0.54	Nil
34	GBM	F	73	0.117419	0.109009	0.52	Nil
35	GBM	M	26	0.056589	0.055569	1.53	Nil
36	GBM	M	57	-0.00833	0.017712	0.99	Nil
37	GBM	M	41	0.079242	0.043123	0.76	Nil

ID	*Diagnosis*	*Gender*	*Age*	$BPND_{ipsi}$	$BPND_{contro}$	$SUV_{cerebellum}$	*Comorbidities*
38	GBM	M	52	0.046216	0.030939	0.95	Nil
39	GBM	F	52	0.200002	0.103775	0.82	Nil
40	GBM	F	24	0.058601	0.008742	0.53	Nil
41	GBM	M	66	0.126209	0.052247	0.91	Nil
42	GBM	M	57	0.028402	-0.00629	0.92	Nil
43	GBM	M	66	0.017007	-0.0268	2.03	Nil
44	GBM	F	76	0.249967	0.086397	0.4	Nil
45	GBM	M	67	0.078894	-0.06289	0.94	Nil
46	GBM	M	71	-0.02521	-0.06573	1.34	Nil
47	GBM	M	30	0.114702	0.051172	0.44	Nil
48	GBM	M	60	0.059321	-0.03177	1.61	Nil
49	GBM	F	27	0.034005	0.000305	0.62	Nil
50	GBM	M	72	0.063852	-0.0015	0.62	Nil
51	GBM	M	54	0.010314	-0.04798	0.74	Nil
52	AA III	M	28	0.004992	-0.02549	1.07	Nil
53	GBM	M	54	0.043875	-0.00803	0.74	Nil
54	GBM	F	39	0.083424	0.076951	0.68	DM II, HTN, COPD
55	GBM	M	60	0.012244	-0.05702	0.83	Nil
56	GBM	M	70	0.058667	0.065498	0.6	TIA, HTN, BPH
57	ptxGBM	F	67	0.01868	0.039392	0.61	Nil
58	ptxGBM	F	73	0.152427	0.119325	0.75	Nil
59	ptxGBM	F	48	0.083251	0.092112	0.39	Nil
60	ptxGBM	M	74	0.088301	0.06582	0.95	Nil
61	ptxGBM	M	73	-0.11893	-0.09684	0.9	Nil
62	ptxGBM	F	65	0.331959	0.258211	0.75	Nil
63	ptxGBM	M	58	0.051	0.022998	0.79	Nil
64	ptxGBM	F	66	-0.04389	-0.05254	0.94	Nil
65	ptxGBM	F	46	-0.02826	-0.04948	0.88	Nil
66	ptxGBM	F	70	0.061146	0.060178	0.68	Nil

Table 6.2 Demographic, clinical and imaging data of subjects with brain metastasis

ID	*Diagnosis*	*Gender*	*Age*	$BPND_{ipsi}$	$BPND_{contro}$	$SUV_{cerebellum}$	*Comorbidities*
67	Melanoma	F	70	0.165444	0.182949	0.35	HTN
68	Renal	F	68	-0.01524	-0.05036	0.63	OA
69	Unknown	M	67	-0.16743	-0.13994	0.47	Dyslipidaemia
70	Renal	M	64	0.013406	-0.05018	1.03	HTN, Depression
71	NSCC	M	57	-0.11759	-0.11813	0.84	COPD
72	NSCC	F	61	-0.0323	-0.06096	1.03	HTN, RA
73	Breast	F	47	0.018863	0.00517	0.54	Asthma
74	Breast	F	71	0.03536	-0.07996	0.64	Nil

Table 6.3 Demographic, clinical and imaging data of subjects with Vestibular Schwannomas.

ID	*Diagnosis*	*Gender*	*Age*	$BPND_{ipsi}$	$BPND_{contro}$	$SUV_{cerebellum}$	*Comorbidities*
75	VS	F	67	0.182592	0.15832	0.71	HTN, DM II, CKD
76	VS	M	32	-0.00477	0.02686	0.68	Nil
77	VS	M	26	0.041204	0.0418	0.53	Nil
78	VS	F	59	0.042237	0.014873	0.87	HTN, DM II
79	VS	F	69	-0.0291	0.000289	0.91	OA, Anxiety
80	VS	F	56	-0.02319	-0.031	0.91	Depression
81	VS	F	61	-0.0015	0.004206	1.25	Nil
82	VS	F	76	0.020136	0.037815	0.8	Nil
83	VS	M	27	-0.06261	-0.01935	0.79	Nil
84	VS	F	61	0.033819	0.057753	1.28	OA, Hypothyroidism
85	VS	M	75	0.053567	0.024246	0.65	DM II
86	VS	F	65	0.042293	0.054872	0.8	Nil
87	VS	F	74	0.016664	0.043303	0.71	Hypothyroidism
88	VS	M	81	0.012093	0.029009	0.73	BPH
89	VS	M	63	-0.0433	-0.01284	0.81	Asthma
90	VS	M	58	-0.06003	-0.0532	0.92	HTN
91	VS	M	54	-0.01213	0.051559	0.61	HTN
92	VS	F	55	0.020174	0.024054	0.66	DM II
93	VS	F	39	0.086994	0.076424	0.71	Nil

Table 6.4 Demographic and imaging data for the healthy control cohort.

Subject	*Gender*	*Age*	$BPND_{brain}$	$SUV_{cerebellum}$
1	F	70	-0.10424	0.68
2	F	60	-0.09965	0.64
3	M	63	0.018554	0.51
4	F	69	-0.0611	0.75
5	F	43	0.009372	0.63
6	F	50	-0.02796	0.85
7	F	44	0.012915	0.26
8	F	63	0.06089	0.73
9	M	46	-0.00501	0.35
10	M	68	-0.09022	0.52
11	M	24	0.015959	0.37
12	M	34	0.039989	0.74
13	M	41	0.029024	0.54
14	M	22	0.054062	0.81
15	F	22	0.066994	0.78
16	F	23	0.015361	0.62
17	M	35	-0.13583	1.01
18	M	26	0.038728	0.87
19	M	45	-0.13839	0.35

In the glioma patients, extra-tumoural BP_{ND} was higher in ipsilateral than controlateral hemispheres (tumour-mirrored regions excluded) (0.061±0.009 vs. 0.029±0.008, p=0.017 respectively, Figure 6.2). An increasing pattern of microglial activation was noticed with higher grade glioma and most prominent in the post-treatment subjects compared to the treatment naive patients, although this failed to reach statistical significance.

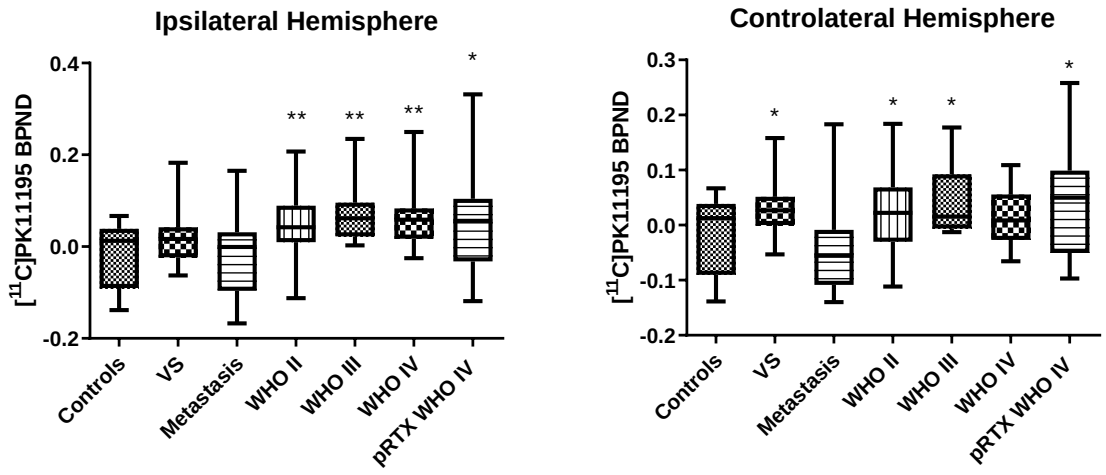

Figure 6.2 BP of the normal appearing brain in the ipsilateral and controlateral hemisphere compared to whole brain of controls (*p<0.05, **p<0.01). VS=Vestibular Schwannoma, pRTX=post-radiotherapy.

The normal-appearing brain of the hemisphere ipsilateral to the tumour of the 38 patients with seizures (Table 6.5) showed significantly higher tracer uptake when compared to the healthy control subjects (mean BPND 0.067 vs. -0.015, p<0.001). In the controlateral hemisphere instead, the uptake was only higher in patients with seizures and it was significantly higher than the controlateral uptake in patients without any seizures (mean BPND 0.039 vs. -0.015, p=0.0064) (Figure 6.3).

Patients with epilepsy demonstrated a higher trend of tracer uptake compared to non-seizure ones on each histological group, although not all the groups were significantly different from controls (Figure 6.4). Furthermore, patients with poor control of seizures demonstrated a higher extra-tumoural [^{11}C]-(*R*)PK11195 binding in their cerebral cortex compared to the ones with good control (two tailed ttest=2.073, p=0.045), this difference persisted on each histological type and through the ipsilateral and controlateral brain separately when compared to controls (Figure 6.5 and 6.6).

Table 6.5 Characteristics of patients with seizures.

ID	Diagnosis	Seizure Type	Duration (months)	Control	Antiepileptics
2	A II	Focal motor	8	Good	VAL
3	A II	Focal motor	21	Poor	PHEN
4	A II	Generalized motor	3.5	Poor	LAM
5	A II	Generalized non-motor	24	Poor	CMZ
6	A II	Generalized motor	1	Good	VAL
8	A II	Focal non-motor	4	Good	LEV
9	A II	Generalized motor	1	Good	LEV
10	O II	Generalized non-motor	30	Poor	CMZ
11	O II	Generalized non-motor	18	Good	VAL
12	O II	Focal motor	1.5	Good	VAL
13	O II	Generalized non-motor	12	Good	LAM
15	O II	Focal motor	0.5	Good	VAL
17	O II	Generalized motor	2	Good	LEV, CMZ
18	O II	Generalized motor	2	Good	LEV
20	O II	Generalized non-motor	2	Good	LEV
21	O II	Generalized motor	3	Poor	LEV, VAL
22	O II	Generalized motor	5	Good	LEV
23	AAIII	Generalized motor	2	Poor	LEV, VAL
25	AAIII	Generalized motor	1	Poor	VAL
26	AAIII	Generalized motor	1	Good	VAL
27	AAIII	Focal non-motor	14	Good	VAL
28	AAIII	Focal motor	3	Good	LEV
29	AA III	Generalized motor	3	Good	LEV
32	AOIII	Focal motor	3	Good	LAM
33	AOIII	Generalized non-motor	2	Good	LEV
34	GBM	Generalized motor	20	Poor	LAM
35	GBM	Focal motor	18	Good	VAL
36	GBM	Generalized motor	3	Good	CMZ
38	GBM	Focal motor	1.5	Good	PHEN
39	GBM	Generalized motor	1	Poor	VAL
42	GBM	Generalized non-motor	1	Poor	VAL
47	GBM	Focal motor	1	Good	VAL

ID	Diagnosis	Seizure Type	Duration (months)	Control	Antiepileptics
54	GBM	Focal motor	5	Good	LEV
55	GBM	Focal motor	1	Good	LEV
56	GBM	Generalized non-motor	2	Good	LEV
70	M	Focal motor	1	Good	LEV
73	M	Generalized motor	1	Poor	LEV
74	M	Generalized motor	1	Good	LEV

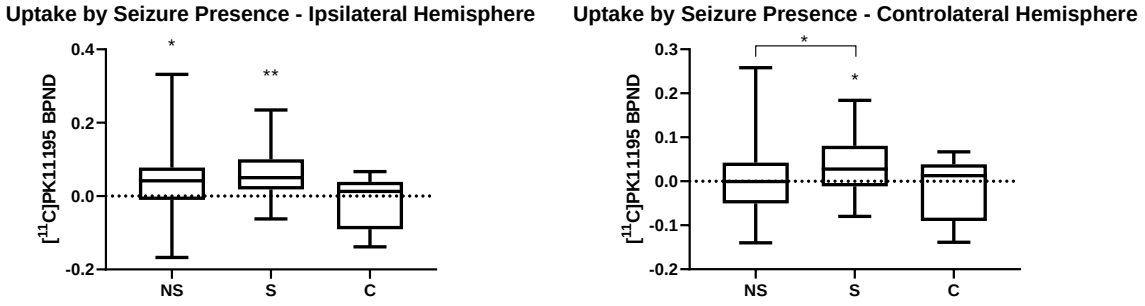

Figure 6.3 Boxplot of BPND in patients with seizures and without for each normal appearing brain hemisphere compared to controls (*p<0.05, **p<0.01). NS=Patients with No Seizures, S=Patients with Seizures, C=Controls.

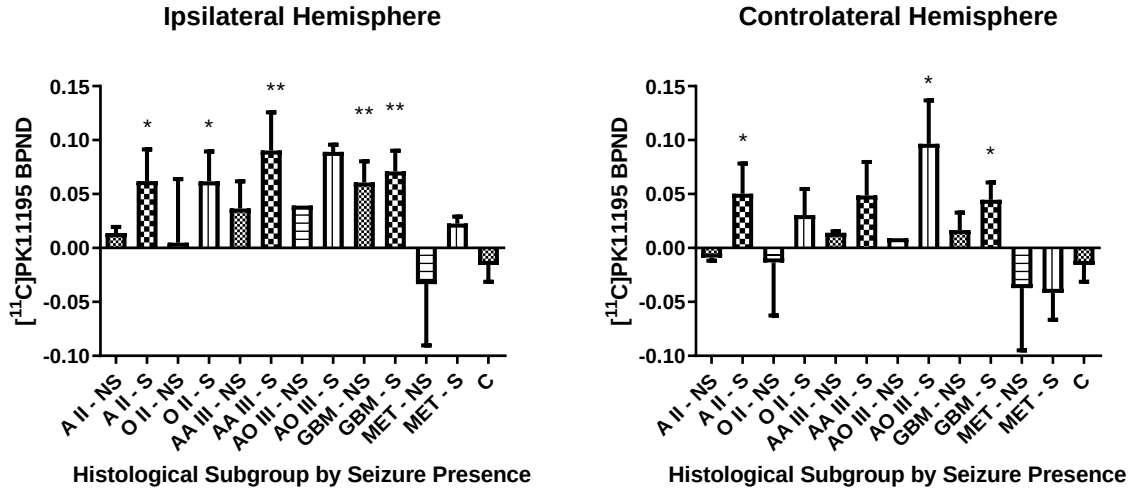

Figure 6.4 Ipsilateral and controlateral hemisphere BPND in extratumoural forebrain in each group according to seizure presence or absence, uptake compared to the control group (*p<0.05, **p<0.01). A II=Astrocytoma WHO II, O II = Oligodendroglioma WHO II, AA III=Anaplastic Astrocytoma WHO III, AO III= Anaplastic Oligodendroglioma WHO III, GBM=Glioblastoma Multiforme WHO IV, MET=Metastasis, NS=No Seizures, S=Seizures Present.

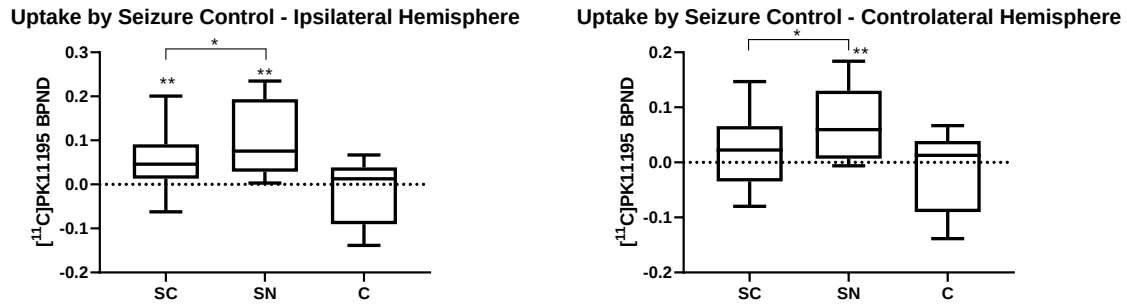

Figure 6.5 Mean BPND in epileptic patients according to their seizure control compared to healthy volunteers (*p<0.05, **p<0.01). SC=Good Seizure Control, SN=Seizures Not-controlled, C=Controls.

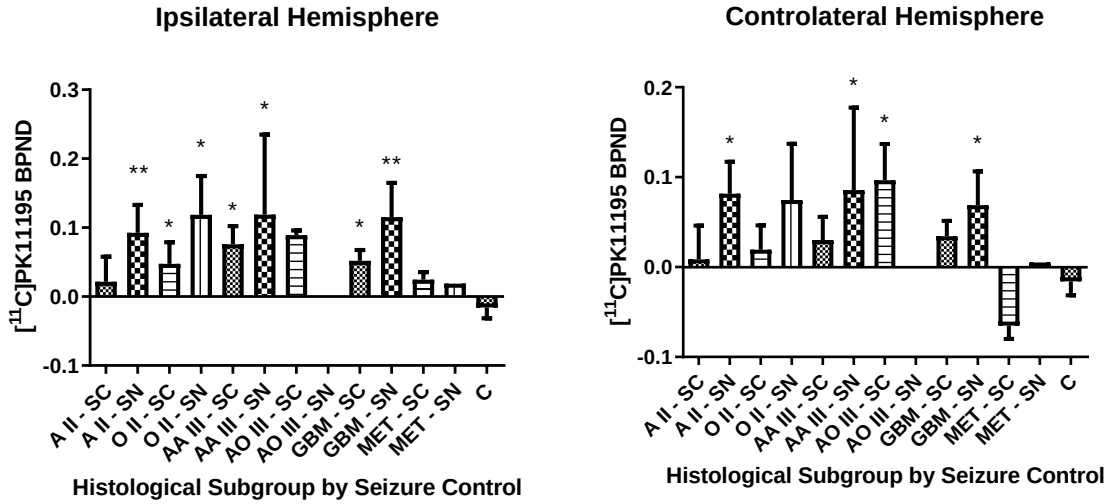

Figure 6.6 [11C]PK11195 uptake in each histological type of patients presenting with seizures according good vs. poor control of epilepsy, mean uptake compared to controls (*p<0.05, **p<0.01). SC=Good Seizure Control, SN=Seizures Not-controlled, C=Controls.

The duration of epilepsy history also, correlated positively with extra-tumoural BP_{ND} in the normal-appearing brain, particularly, the controlateral hemisphere (Spearman's ρ=0.428, p=0.007; Figure 6.7) but also significant in the ipsilateral hemisphere (Spearman's ρ=0.332, p=0.041). These findings suggest an association of microglial activation with not only seizure control but also duration. Meanwhile, no difference in the extra-tumoural binding of [11C]-PK11195 was noted when comparing patients with partial seizures vs those with generalised seizures (Figure

6.7) and we did not observe any correlation between extra-tumoural BP_{ND} and tumour size.

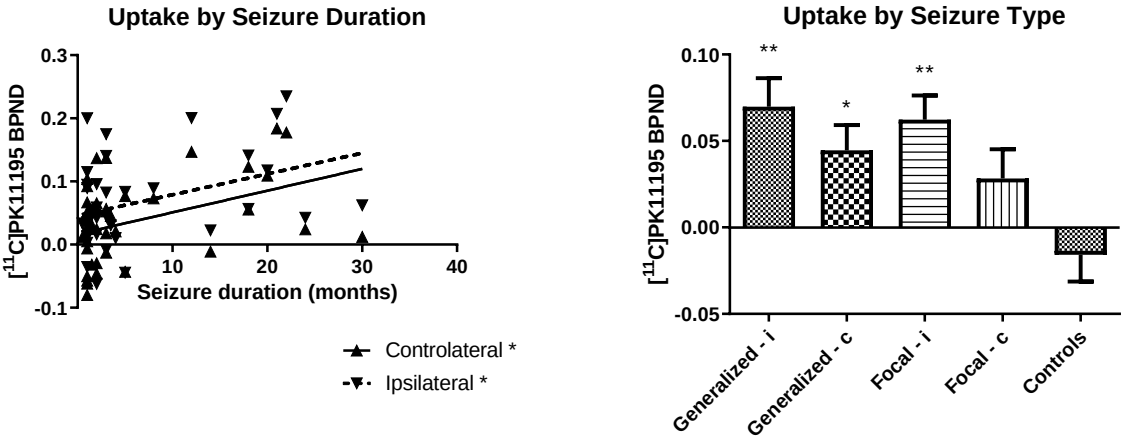

Figure 6.7 Correlation of NAB uptake to duration of epilepsy and in relation to seizure type (generalized *vs* focal).

The most used antiepileptic in our cohort was Levetiracetam followed by Sodium Valproate. Patients using Levetiracetam showed a better control of their seizures and the lowest tracer uptake compared to the other groups. Except patients on Lamotrigine, all the other groups with poorly controlled seizures showed higher uptake values in comparison to the well controlled ones (Figure 6.8).

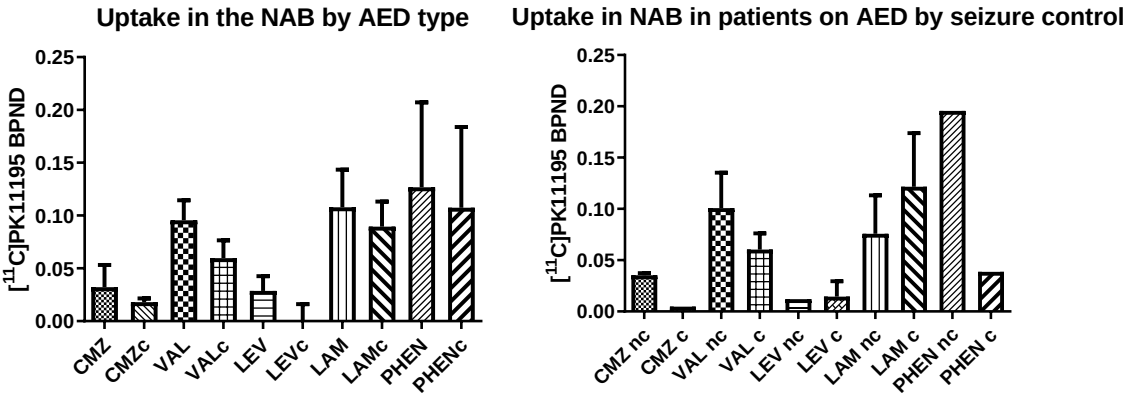

Figure 6.8 Tracer uptake in the normal appearing brain in patients with seizures according to their antiepileptic type and seizure control.

Finally, we observed a weak inverse correlation of the normal appearing brain and cerebellar SUVs in patients with glioma which was significant only with respect to the controlateral hemisphere (R^2= -0.26, p=0.031) (Figure 6.9). In the healthy and disease control cohorts we did not find any correlation between cerebellum SUVs and normal brain.

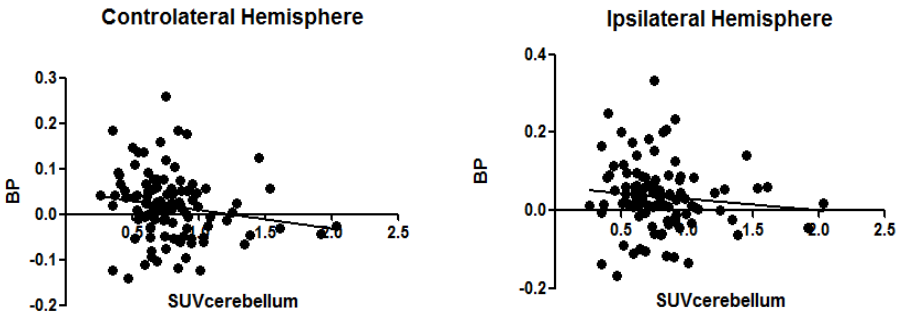

Figure 6.9 Correlation of cerebellar SUVs (10-60mins) to NAB uptake

Post-mortem brain tissue analysis

Expression of the mutant $IDH1^{R132}$ protein allowed for accurate mapping of neoplastic cells in all the regions examined. The areas selected for Iba1 and TSPO quantification in the ipsilateral brain were free of tumour cells and none of the samples from the brain controlateral to the tumour site showed neoplastic infiltration (Figure 6.10). Microglia cells in the ipsi- and controlateral, tumour-free grey matter of subjects with glioma were significantly higher than control subjects (Figure 6.11) with an average density in tumour bearing brains ranging between 450 and 100 cells per mm2 and a density below 200 cells per mm2 in control tissue (Figure 6.11). Neuronal density in the controlateral cortex was reduced in subject with glioma compared to normal controls (Figure 6.12).

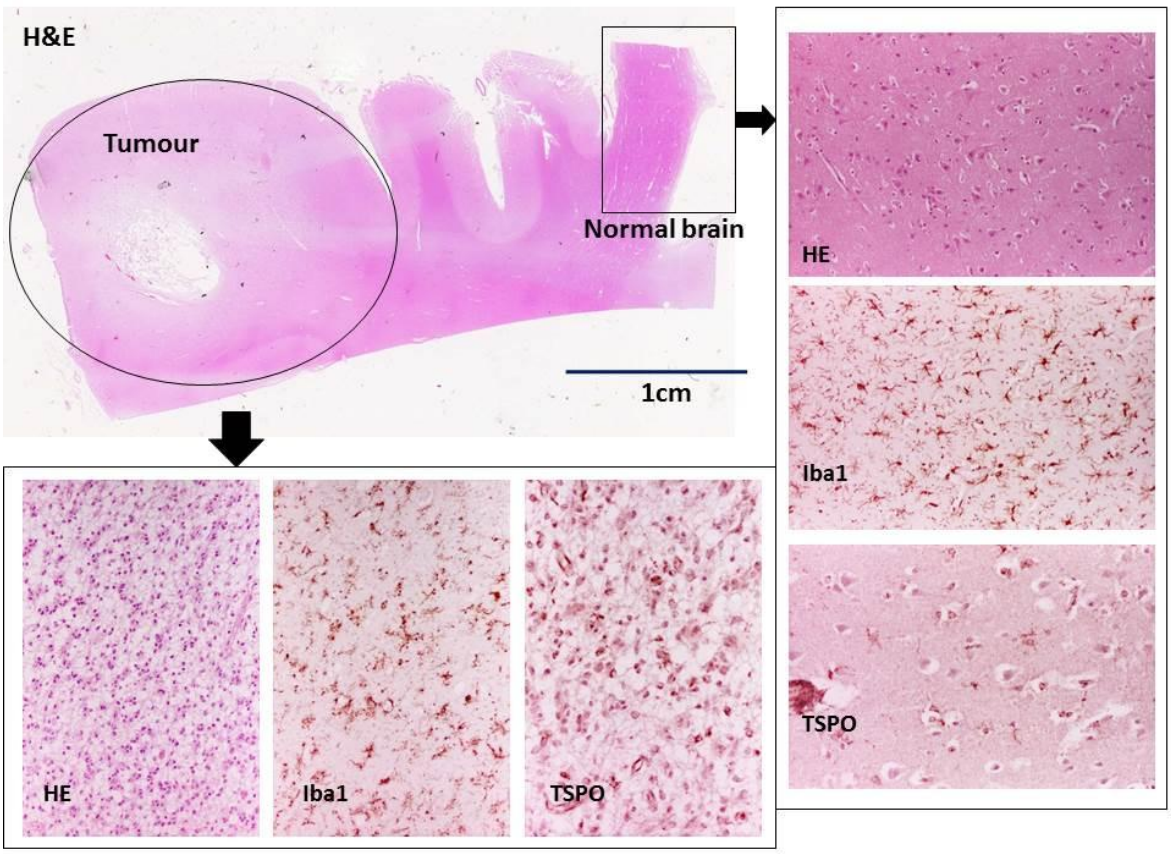

Figure 6.10 WHO grade II oligodendroglioma infiltrating the temporal lobe (haematoxylin-eosin, whole mount). Tumour and Normal tissue sections stained with haematoxylin-eosin (HE, x20), immunoperoxidase for microglial density (Iba1) and TSPO expression (both immunoperoxidase, x20).

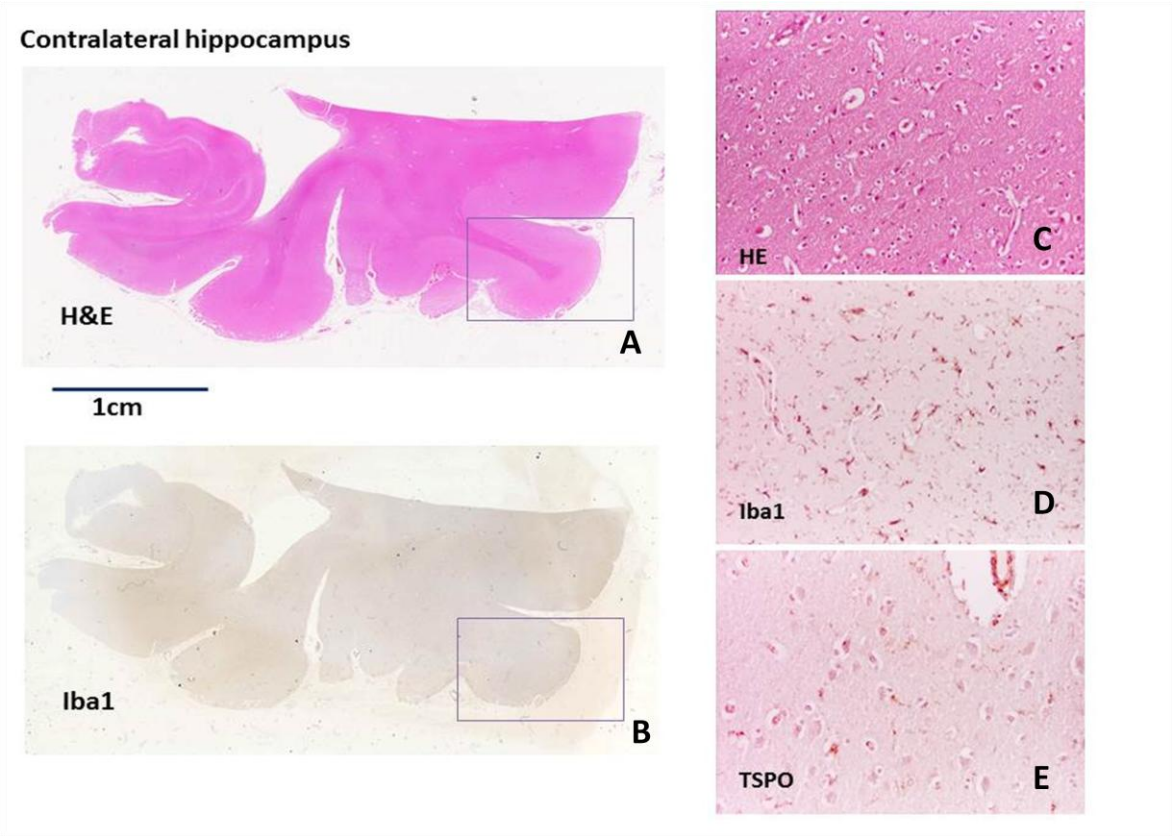

Figure 6.11 The controlateral hippocampus, fusiform gyrus and inferior temporal lobe of the same patient are documented in A (haematoxylin-eosin, whole mount). The same whole mount macrosection is stained for the microglial marker Iba1 (B, immunoperoxidase, whole mount). Figure C shows the normal appearing cortex (haematoxylin-eosin, x20); microglial density is represented in figure D (immunoperoxidase, x20) and TSPO expression in figure E (immunoperoxidase, x20).

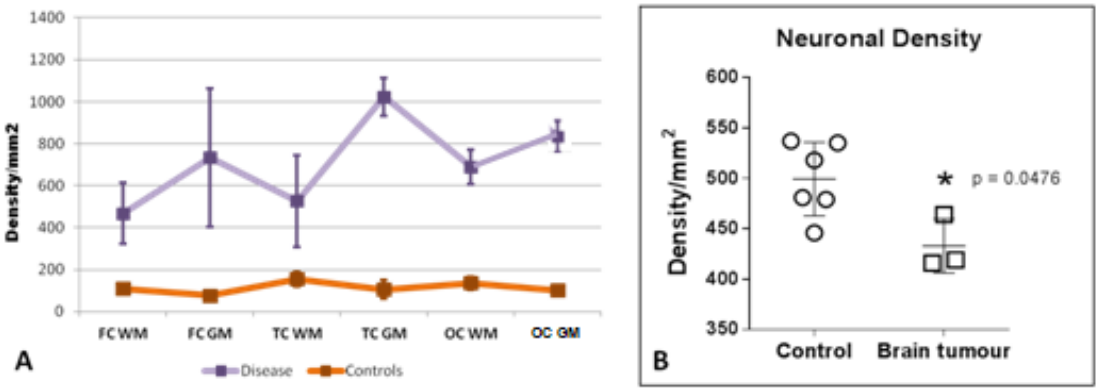

Figure 6.12 Quantification of microglial density in the controlateral temporal cortex of subjects with glioma against control subjects is represented in figure A. Figure B shows the differences in neuronal density in the same regions. FC=Frontal Cortex, TC=Temporal Cortex, OC=Occipital Cortex, WM=White Matter, GM=Grey Matter, TC.

6.5 Discussion

We have documented significantly increased [11C]-(R)PK11195 binding in the normal-appearing grey and white matter of patients with hemispheric gliomas indicating diffuse microglial activation in areas that are unaffected by the primary tumour. [11C]-(R)PK11195 binding was evaluated through cerebellar GM SRTM which has been shown to be robust [119]. In our study we noticed a minor insignificant correlation of the NAB uptake to the cerebellar SUV in patients with brain tumours only. This could infer a possible increased global inflammation in the whole brain including cerebellum which could potentially affect the BPND parametric maps using cerebellar reference. Although the accuracy of the SUV measurements is still doubtful in tracers with specific binding like [11C]-(R)PK11195 [57, 118, 147, 149]. Additionally no correlation was noticed in the healthy cohort and subjects with vestibular schwanommas. Given previous results of direct voxel-by-voxel comparison of supervised cluster analysis and cerebellar SRTM have yielded similar values comparable to literature[57, 58] we continued to use our established method[119].

Analysis of post-mortem brains confirmed widespread neuroinflammation and TSPO expression in GAMMs in the ipsi- and controlateral brain distant from tumour epicentre and free from neoplastic infiltration. Sections of normal appearing brain distant from the tumour were assessed via immunohistochemistry staining for IDH status to avoid any areas of distant tumour infiltration. These areas were also stained for Iba1 expression showing an increased microglial activation coinciding with the raised TSPO expression.

To our knowledge, this is the largest PET imaging study using TSPO as a biomarker of neuro-inflammation in glioma patients, and the first to show widespread neuro-inflammatory response in cerebral regions distant from the tumour site.

In our study we additionally compared the neuroinflammatory response of two different types of intracranial tumours, metastastic lesions and vestibular schwannomas. Although a slight increased tracer uptake was noticed in the controlateral hemisphere of the VS group, this was not significantly different from the controls in the ipsilateral hemisphere instead. One explanation could be the

possibility VS can cause neuronal degeneration locally in the cochlear hair cells [197], followed by an upstream activation of microglia in the controlateral brain along the axons. Less probable would be a downregulation of microglial activation in the cerebellum affecting the input function and resulting in higher BPND of both hemispheres. Meanwhile, patients with metastatic lesions showed the lowest binding potential values in the normal appearing brain. This could represent an immunosupressed state initially which sets the environment for metastatic invasion. The two highest BP values in the metastatic group belonged to patients 67 and 74, representing a haemorrhagic melanoma secondary lesion and a triple negative breast metastasis under active immunotherapy at the time of the scan. In both cases this could represent more likely an increased inflammatory state from the bleed or from the systemic treatment rather than from the metastasis itself, although this should be investigated in a larger homogeneous cohort.

In our glioma group, none of our patients suffered from other neurological or psychiatric disorders, or had systemic diseases, suggesting that the increased microglial activation in their brains was related to the tumour. Several factors associated with the tumour (e.g. epilepsy, neuronal and trans-synaptic damage due to neoplastic infiltration, and neoplastic spread itself) could have contributed to the PET abnormalities. Of these we regard epileptic seizures - the most common feature presented in 38 out of 93 patients - to be the most likely cause of increased microglial activation in brain areas remote from the tumour. This interpretation is supported by the evidence of the highest extra-tumoural BP_{ND} in patients suffering from long-lasting or refractory seizures with generalisation (patient 3 and 23, Table 1), and the positive correlation between epilepsy duration and extra-tumoural BP_{ND} increase. In addition, patients who had generalised seizures showed increased microglial activation in both cerebral hemispheres, compared to the patients who had focal seizures. It therefore is possible that the observed microglial activation is the consequence of neuronal damage caused by seizures.

Previous studies support our hypothesis. *In vitro* experiments have shown that neuroinflammation can be induced by seizures [198]. Microglial activation has also been demonstrated *in vivo* in refractory epilepsy [199] and epileptogenic cortical dysplasia using [^{11}C]-(*R*)PK11195 PET, and confirmed on histological examination on the surgical specimens [199]. High uptake of [^{11}C]-PBR28, another PET tracer for

microglial activation, was found ipsilateral to the seizure focus in the hippocampus, parahippocampal gyrus, amygdala, and fusiform gyrus of patients with temporal lobe epilepsy [200]. Gershen *et al*. [201] also reported elevated binding of [^{11}C]-PBR28 both ipsi- and controlateral to seizure foci in patients with temporal lobe epilepsy, suggesting ongoing inflammatory responses. Furthermore, examinations of brain tissue resected from patients with idiopathic or secondary refractory epilepsy showed activated microglia prevalent in the cortex and/or subcortical white matter and associated up-regulation of pro-inflammatory molecules [202, 203].

These studies suggest that active neuroinflammation is a common feature of epilepsy of diverse etiologies, in which gliomas could be no exception. Our results of bilateral but ipsilateral-dominant increase of extra-tumoural [^{11}C]-(*R*)PK11195 binding is in keeping with the findings that brain tumours not only enhance the epileptogenicity of peritumoural tissue but also influence the entire brain [173]. Brain inflammation could also contribute to the occurrence, duration and recurrence of seizures [198, 204], where the prominent immune response may play a role in neuronal damage and epileptogenesis, due to merely phenotypic changes of microglia [204], and/or substances released by activated microglia, such as interleukins, tumour necrosis factor-α, free radicals, nitric oxide, proteinases and eicosanoids [56, 173]. Nowak *et al*. documented an astrocytoma patient with severe epilepsy who showed dramatic reduction in seizure frequency following treatment with minocycline, an agent known to suppress microglial activation [205]. However, to what extent microglial activation represents primary neuroinflammation to trigger seizures or a secondary response to neuronal damage caused by the epilepsy remains to be established. It is possible that a vicious cycle of seizure-induced inflammation and inflammation-induced seizures is initiated during the disease process.

Accumulating clinical and experimental evidence advocates the relevance of neuroinflammation and epilepsy, indicating several crucial aspects of inflammatory processes in the pathophysiology of epilepsy: 1) neuroinflammation is induced by recurrent seizures; 2) it is long-lasting, persisting for days after the termination of seizures; 3) microglia are likely to play a pivotal role in perpetuating this response by secreting several inflammatory molecules [206]. All these may apply to our patients. It is possible that the continual abnormal electroactivity is driving the widespread

neuroinflammatory process. In addition, our limited longitudinal data also supported the hypothesis that the PET finding is related to seizure activity.

In three patients who underwent a pre-operative follow-up MRI/PET scan, different levels of decrease in extra-tumoural BP_{ND} between the baseline and the follow-up scan were seen in patients 2 and 23. Patient 2 had become seizure-free during the 6-month interval and demonstrated a BP_{ND} decrease in both hemispheres, whereas patient 23 who was not entirely seizure-free during the interval showed a BP_{ND} decrease in the ipsilateral hemisphere and static binding in the controlateral side. Chronically activated microglia as a source of neurotoxins have been hypothesised to exacerbate neuronal injury [207], a potential reason that might underpin the unsatisfactory seizure control and/or even tumour progression in patient 23. In contrast, patient 14 had no seizures throughout the investigation and showed no changes between the two scans, indicating relatively constant microglial activity over the 8-month period. When interpreting this result, it is important to note that the BP_{ND} changes in the follow-up scans of the former two patients may still well be within test-retest variability as compared to the control subject. Although the number of patients assessed longitudinally is small, the results suggest a trend of reduced microglial activity following seizure control. The BP_{ND} changes over time in these 3 patients also confirm our PET finding in the normal brain to be genuine.

Additionally, we observed an inverse correlation between extra-tumoural [^{11}C]-(*R*)PK11195 binding and the most commonly used antiepileptic drug in our cohort, levetiracetam. So far no clinical studies have addressed the association between extra-tumoural [^{11}C]-(*R*)PK11195 binding and antiepileptic drugs regimens, although experimental work has revealed an anti-inflammatory effect of valproic acid and phenytoin, both of which suppress microglial activation [208, 209]. Should such an effect exist in our patients who were taking these medications, it would have led to under- rather than overestimation of the extra-tumoural [11C]-(R)PK11195 binding. In our cohort we noticed even lower values in patients on Levetiracetam, for which currently there are no studies to relate with neuroinflammation. Interestingly patients on Levetiracetam on our cohort also exhibited better control of their seizures compared to other antiepileptics.

Of note, 36 of the 93 patients without documented seizures also showed relatively high extra-tumoural [^{11}C]-(*R*)PK11195 binding in ipsilateral (0.0385±0.095 vs. -

0.0158±0.0676, p=0.02) and controlateral hemisphere compared with controls (0.0048±0.0805 vs. -0.0158±0.0676, p=0.32). As a group, extra-tumoural binding in their ipsilateral hemisphere did not differ significantly from that in epileptic patients, although the group mean value of extra-tumoural BP_{ND} tended to be higher in the latter (Figure 6.2). Whilst with regard to the controlateral hemisphere uptake was borderline higher in patients with epilepsy compared to ones without seizures (0.0386±0.068 vs 0.0048±0.0805, p=0.05). This finding further supports the suggestion that multi-factorial mechanisms contribute to the remote microglial activation. Brain tumours influence the whole brain neural networks [173]. For this reason, distant trans-synaptic microglial activation associated with functional connectivity could also contribute to the increased extra-tumoural [^{11}C]-(*R*)PK11195 binding. Trans-synaptic activation has been documented in several conditions that cause focal brain damage and result in glial responses in regions connected to the lesion site. In stroke for instance, an increased [^{11}C]-(*R*)PK11195 uptake in areas remote from the primary lesion without obvious structural damage was documented independently by two groups [178, 179]. As a persistent pathological stimulus, gliomas could cause damage to neighbouring neurons and their connecting fibres [173], thus inducing microglial activation in the projection pathways. It may not herald overt destructive pathology but rather, indicates active tissue responses to potential degeneration or disconnection in retrograde and/or anterograde projection areas. It is possible that such secondary microglial responses, beyond the primary lesion, could influence important nodal points of the affected anatomical pathway in proximity as well as distant to the tumour. This possibility is supported by our observation of increased [^{11}C]-(*R*)PK11195 binding in both the ipsilateral (but distant from the tumour) and controlateral hemispheres when compared with controls.

Although the clinical significance of widespread microglial activation remains uncertain, at this stage our results indicate that gliomas are associated with diffuse brain inflammation, which may represent a novel target to improve glioma therapy and seizure control. Glioma infiltrating microglia have been reported to show both anti- and pro-tumourigenic effects, with the majority of studies now favouring the latter [210-212]. Extra-tumoural activated microglia might still exert a defensive attempt to limit neoplastic growth, but could also be manipulated by the tumour to facilitate tumour cell invasion [212]. Correspondingly, there is growing interest in testing medications that modulate immune processes, e.g. nonsteroidal anti-

inflammatory drugs and minocycline, as anti-tumour agents [213]. Our study highlights the need for non-invasive methods to identify appropriate patient populations who may benefit from anti-inflammatory or immunomodulatory therapies. However, definition of specific neuroinflammatory biomarkers for this purpose remains a challenge, since currently there are none available with proven clinical utility for patients with glioma and/or epilepsy. [^{11}C]-(*R*)PK11195 PET may provide a surrogate marker in assessment of those therapeutic approaches as well as stratification of patients according to their individual neuroinflammatory patterns.

Our *in vivo* finding in the normal-appearing brain areas would require a correlation with histopathology. However, for obvious ethical reasons it was not possible to sample tissue from normal-appearing brain regions in patients for research purposes,

Previously a few pathological and experimental studies on gliomas had observed increased microglia in normal brain tissue [175, 177], but did not investigate the association with epilepsy. In particular, Roggendorf *et al*. [175] documented diffuse microglial activation in post-mortem brains of patients with malignant glioma, but the microglial response could also have been induced by chemo- and/or radiotherapy these patients had been exposed to. In contrast, our *in vivo* finding prior to any surgical intervention or chemo- and radiotherapy is more supportive of on-going inflammatory changes in the brain, which is related to the presence of gliomas.

Several novel TSPO ligands with improved affinity and better signal-to-noise ratio than [^{11}C]-(*R*)PK11195 have recently been developed. Clinical application of those ligands is hampered by the dependency of binding to a TSPO polymorphism [214, 215]. All novel ligands tested in human so far display a tri-modal distribution in binding affinity (high, low and mixed). Variation in affinity of novel ligands and its diverse distribution from subject to subject would confound the interpretation of PET data. We therefore chose [^{11}C]-(*R*)PK11195 for our study because this well established and characterised TSPO tracer seems not to be influenced by such a polymorphism.

In conclusion, we have shown an increase of [^{11}C]-(*R*)PK11195 binding in otherwise normal-appearing brain structures of patients with gliomas, indicating widespread microglial activation especially in subjects with poor control of epilepsy. [^{11}C]-(*R*)PK11195 PET provides an *in vivo* demonstration of this inflammatory response

which is not detectable with structural imaging such as MRI. The clinical significance of our findings remains uncertain. Further studies are required to evaluate the impact of widespread inflammation on generalisation of epilepsy and seizure control.

Acknowledgments

This work was funded in part by the European Union's Seventh Framework Programme (FP7/2007-2013) under grant agreement INMiND (HEALTH-F2-2011-2788500), the Engineering and Physical Science Research Council UK grant MIMIT (EP/G041733/1), and the Astro Fund charity. We thank the patients and volunteers who participated in this study, and the staff involved in the scanning, especially Michael Green for radioligand synthesis, Jose Anton for image reconstruction, Dr Christopher Kobylecki for scanning of volunteers, Dr Pinkham and Dr Quartuccio for the recruitment in the "Brain Metastasis" cohort, Dr Lewis for the recruitment in the "Vestibular Schwannoma" cohort, and the radiographers Eleanor Duncan-Rouse and Gerrit Helms Van Der Vegte. Mr Ajit Sofat, Mr James Leggate, Dr Ioannis Trigonis, Dr Gerard Thompson, Dr Calvin Soh, Dr Kumar Das and Dr Daniel Crooks provided clinical support and/or helped with patient identification.

Chapter 7 – Summary, General Discussion and Future Directions

In this study we demonstrated the TSPO expression in gliomas and extension of the microglial activation in the normal appearing brain beyond the tumour defined on FLAIR sequence. In the first experimental chapter we compared our results with two different kinetic approaches for the [11C]-(R)PK11195 binding, supervised cluster analysis and cerebellum grey matter reference. Given our similar results, as well as previous literature, we continued to use only the cerebellar input function for the rest of the analysis. Our radiological data, confirmed with the histology showed a very good accuracy of [11C]-(R)PK11195 uptake in identifying transformation in glioma. Our results were even more accurate in the oligodendroglial tumours where other PET tracers have shown higher false positive rates and overlap between grade II and III tumours. To consolidate our findings we investigated a cohort of thirty oligodendrogliomas and demonstrated significantly higher TSPO expression in anaplastic tumours. TSPO was mainly expressed in the neoplastic cells, rather than microglia or endothelium.

In the second part of our study we investigated the correlation of [11C]Methionine with perfusion and diffusion MR markers. Our results demonstrated an increasing uptake of Methionine with grade, although the areas with the highest uptake did not correlate spatially with the areas of increased relative cerebral blood volume and flow, and neither with the trough fractional anisotropy or mean diffusivity. In most of the cases these areas were more than 1cm apart, making amino acid PET tracers to be considered a valuable guide in the biopsy of tumours involving eloquent areas and cannot therefore be resected. [11C]Methionine also proved accurate in predicting patients' outcome.

Finally, the [11C]-(R)PK11195 PET imaging revealed widespread microglial activation in the normal appearing brain in patients with glioma and vestibular schwannoma whilst an overall suppression of microglia was noted in patients with brain metastasis. Increased neuroinflammation was strictly correlated to the seizure activity and duration. The novelty of the present work lies in the correlation of in vivo and tissue analysis of TSPO expression, the unique series of oligodendrogliomas in comparison with astrocytomas, the investigation into the normal appearing brain structures, and the combination of two advanced imaging modalities – high

resolution PET and perfusion MRI – in an attempt to apply them in guiding tumour biopsy. This work provides important insights into the neuroinflammatory response in the commonest type of brain tumours, and is likely to have beneficial impacts on type stratification, dedifferentiation detection, biopsy planning, symptom control, therapeutic development and prognosis prediction. Extended discussion pertinent to our findings and the study is presented in this chapter, with plans of future work outlined.

7.1 Summary of findings

In this project we used a multi-biomarker approach to further characterise gliomas and the surrounding brain with two different PET tracers in addition to MRI perfusion and diffusion metrics.

Initially we investigated the TSPO PET imaging with [11C]-R-PK11195 as a potential tracer to identify transformation. Our results, in keeping with the previous findings from our group [65] showed an increase of tracer uptake in the anaplastic gliomas which was more accurate in the oligodendroglial type with 1p/19q codeletion according to the latest WHO classification. These results matched the increased TSPO expression in tissue evaluated by optical density on TSPO antibody immunohistochemical staining. After noticing a higher accuracy in oligodendrogliomas predominantly, and matching imaging with tissue data, we extended analysis of TSPO in tissue from further 30 consecutive patients diagnosed with oligodendrogliomas 1p/19q. The tissue analysis confirmed once more the increased TSPO expression in anaplastic WHO grade III tumours. Representative tissue with low and high TSPO expression has been sent for further analysis with RNA-sequencing, but unfortunately has not been available to include in this thesis.

Contrast enhancement alone was a poor predictor of anaplastic transformation according to our data, this has also been confirmed in additional literature as discussed earlier. Oligodendrogliomas showed additionally raised rCBV values compared to similar grade astrocytomas, as previously has been described in literature, but in our study rCBV peak values failed to discriminate accurately higher grade gliomas. As discussed previously in chapter 4, other larger multi-centric studies have shown different results from ours. One of the reasons for the lower accuracy of rCBV in our study could be the low study power, which was primarily designed as a

PET imaging study; hence the number of recruited participants would be quite satisfactory for such a technically complex protocol.

We additionally hypothesised that the higher tracer uptake in oligodendrogliomas compared to the same grade astrocytomas could have been mainly due to the increased and prominent "chicken-wire" vasculature in oligodendrogliomas. This could have an impact on the endothelial binding of TSPO causing an increased uptake. Though, our data showed that regions of increased rCBV did not co-localise with the peak [11C]-R-PK11195 uptake. Furthermore, we extended our analysis by performing an innovative 3D histological assessment derived from immunohistochemical staining of the tissue for endothelial (CD31), microglial (Iba1), neoplastic (IDH) and TSPO expressing cells. Similarly we could not find visually co-localisation of TSPO and endothelial cells, but noticed that most of the TSPO was expressed by the neoplastic cells instead. The physipathological mechanisms for which oligodendrogliomas express higher TSPO remain still a puzzle from our study and will need further investigation in the future. RNA sequencing could potentially answer part of this question by detecting protein transcription and identifying mechanisms involved at cellular level.

One of the other objectives of our study was to identify a potential threshold for [11C]-R-PK11195 PET images which could identify safely tumour regions and serve as a cut-off for biopsy targeting. According to our data we identified through Youden's index, the best threshold to be the BPND greater than 1.4 . This threshold had a 100% specificity in identifying anaplastic transformation in both astrocytomas and oligodendrogliomas. Despite our results, this threshold will need to be validated further in larger cohort studies, but at present could be an indication to define tumour ROIs and select target regions.

In the second part of our study we investigated a different successful radiotracer in comparison to the MR perfusion and diffusion metrics. We noticed a very close correlation of [11C]Methionine peak uptake with peak rCBV and rBF values. Although, similar to the [11C]-R-PK11195 data in Chapter 4, the peak MetPET and rCBV/rBF did not colocalise. This was evident also from the different time-activity curves of dynamic [11C]Methionine in the different peak ROIs. This phenomena highlights the different possible underlying physiopathological processes and makes less probable the PET signal being generated only from the tracer's flow. In future

this will be further investigated by our group on tissue data collected through targeted biopsies. Dynamic [11C]Methionine data also showed good accuracy in separating higher grade gliomas and stratifying patients with poorer prognosis. In relation to the diffusion metrics, MetPET data correlated significantly to the trough mean diffusivity and fractional anisotropy, although these regions did not co-localise. In lower grade gliomas these regions appeared even more distant than the higher grades, raising potential questions on the most appropriate modality for biopsy targeting which can be challenging in tumours involving eloquent areas. Identifying most "active" or "malignant" areas within the tumour is important on these occasions to avoid downgrading resulting in undertreatment. The discrepancies between the peak MetPET and MD/FA ROIs is another example of tumour heterogeneity.

Finally, in the last chapter of this thesis, we investigated how the normal appearing brain is affected by gliomas. Previous research from our group hinted a possible higher uptake even in the controlateral hemisphere of the patients with glioma. This was also evident on visual inspection of our TSPO PET scans suggesting an inflammatory response of the whole brain rather than just focal disease. The results of our analysis in fact confirmed a significantly raised expression of TSPO measured by the [11C]-R-PK11195 uptake in the ipsilateral and controlateral brain of our glioma patients compared to a cohort of healthy subjects. This rise was also evident when compared to a diseased cohort consisting of intracranial supratentorial metastatic lesions and vestibular schwanommas. In fact the mestastatic group, showed almost a "suppression" of the TSPO expression in the normal appearing brain with significantly negative values when compared to the normal cohort. Whilst the vestibular schwanomma group showed an increased uptake only in the controlateral hemisphere which was hard to explain but a possibility could be retrograde axonal neuro-inflammation. We searched to find the cause of this rise in the inflammation of the whole brain in patients with glioma. Excluding other confounders we noticed that seizure activity was an independent predictor of increased inflammation. The longer the history of seizure and poor control, the higher was the [11C]-R-PK11195 uptake. Obviously there are limitations in defining control of seizures despite our tentative to minimize this into minimum relying on neurology clinic follow up appointments and reviews documented in epilepsy clinic. Certainly the connection of seizure activity and neuro-inflammation was quite evident, but difficult to determine which one came first . In one of the patients with metastasis who was the only with a history of

seizures in this group, the tracer uptake was significantly higher in comparison to the others in the same group, re-enforcing the earlier link. We also looked for any effects from the type of antiepileptic used, noticing that newer generation levetiracetam was associated with lower tracer uptake compared to other types of drugs used. Whether this is due to reduced inflammation or better control of seizures in this subgroup is yet difficult to ascertain.

7.2 Other Methodology considerations

7.2.1 Tumour delineation and generation of ROIs

Tumour delineation can be challenging in glioma, especially in lower grade gliomas with no contrast enhancement. In our study we defined the tumour regions initially on FLAIR sequence using a semiautomatic method on itkSNAP [129]. The tumour masks generated were then manually corrected to include any methionine areas above the threshold of 1.4, which has been previously described in literature [91, 216], as well as any other abnormal tissue on T1 and T2. Whilst in high grade gliomas, all the enhancing rim, excluding the necrotic core, and any abnormal methionine uptake areas above 1.4 T/N ratios were defined as the tumour ROI. For the final chapter, instead, any visible T2 abnormal areas, including oedema were excluded from the normal appearing brain.

Vasogenic oedema is a common feature in all brain tumours, especially high grade and metastatic lesions. The mechanisms triggering the oedema could activate microglia in proximity. This has been previously demonstrated in a preclinical study showing reactive microglia and increased inflammatory cytokines within the oedematous areas of a rodent glioma model although infiltrative tumour cells were also found within the same perifocal oedema zone, which might have concomittantly triggered microglial activation [217].

A correlation between degree of peritumoural oedema and tumour-associated inflammatory cells, namely activated microglia and macrophages, has long been reported in human gliomas, suggestive of a possible role of inflammatory cells in the pathogenesis of peritumoural oedema [218].

The possibility of oedema-induced adjacent microglial activation could also explain why the extra-tumoural [11C]-(R)PK11195 uptake is higher in the ipsilateral than the controlateral hemisphere, but is insufficient to underpin the increase in the latter, because peritumoural oedema is usually restricted to one hemisphere as seen in most of our patients.

7.2.2 Estimation of [11C]-PK11195 binding potential

The estimation of [11C]-(R)PK11195 binding is dependent on the kinetic model chosen for the analysis. Different choices of reference regions result in different BPND estimates. The BPND values in our control subjects are similar with those presented in previous studies using the same model (SRTM with either cerebellar GM or total cerebellum as reference tissue input function), suggesting that we produced BPND results consistent with other literature [58, 65, 118, 119, 189]. The BPND values of controlateral hemisphere in our patients are also comparable with those studies, albeit in different pathological conditions [57, 58, 180, 219]. Moreover, the TACs in normal brain structures of our patients appear similar (in terms of their shape) with controls as well as those reported in the literature [118, 185]. Taken together, these results confirm the feasibility of the kinetic modelling and the suitability of [11C]-(R)PK11195 PET in glioma imaging.

According to our findings in Chapter 6, glioma may be viewed as a disease with widespread neuroinflammation extending beyond the tumour in the entire brain. The cerebellum might also be affected, thus demonstrating a certain level of specific [11C]-(R)PK11195 binding which might affect the reference modelling. This fact may be reflected further on our findings of the inverse correlation of cerebellum SUVs and normal appearing brain uptake. In our study we compared our results with SVCA method which yielded similar results but lower BP values.

Finally, vascular binding of TSPO has been described in previous literature [118]. Although in our previous collaboration we emphasise the importance of including a vascular compartment in the SRTM equation, in glioma we found most of the PET signal is derived from the neoplastic cells, hence our results still should remain unchanged.

7.2.3 11C-Methionine dynamic PET imaging

In our study we demonstrated an increasing methionine uptake with tumour grade. The previously described overlap between high-grade astrocytic and low-grade oligodendroglial tumours [139, 161] was improved with the new WHO classification and implementation of the molecular markers [131]. Despite the significant correlations we found in the peak MetPET with perfusion and diffusion MRI values, the regions of interest in different modalities appeared to be significantly apart. These findings highlight the heteregoneity within the tumour microenvironment, even in the low grade gliomas, which is in an important factor not only for surgical planning but also for delivering an efficient adjuvant therapy.

Dynamic [^{11}C]Methionine PET smoothed TACs showed a significant difference between the peak MetPET and highest rCBV regions in the oligodendrogliomas, but not in the astrocytomas. Although our results might not be sufficiently powered, and we lack any tissue correlation, this is a novel finding which underlines the biological differences between the two histotypes. Of note is also our observation in higher grade gliomas, where regions of interest from different modalities appeared to be closer in comparison to lower grade tumours. This potentially could be due to the BBB damage in higher grade gliomas, where passive diffusion of the tracer could also contribute to the total uptake of methionine [220]. Although, it has been reported that the amino acid transport system, is mainly dependent on the proliferative activity of the human glioma cells [221] and several studies have shown increased uptake of methionine in most low-grade gliomas despite the absence of damage to the BBB [80, 93, 95, 145].

7.2.4 Imaging data and correlation to histopathology

In this study, we tried to implement such PET/MRI-guided sampling using the neuronavigation system, with biopsy targets chosen from areas of contrast enhancement, highest rCBV and/or [11C]-(R)PK11195 BPND approachable. However,

due to the fact that the majority of biopsies were conducted under open procedures prior to tumour debulking, most of the targets were not precisely hit, indicated by post hoc registration of the recorded biopsy sites back to the BPND and rCBV maps. Such inaccuracy was caused by subtle brain shift following CSF loss and deformation of the brain anatomy after dural opening. This limited number of cases precluded an in-depth investigation of detailed PET-pathology correlation site-by-site. Such a correlate may be achievable incorporating the specimens obtained from open biopsies that still contain tissue from high, moderate and low BPND areas, provided that the effect of brain shift can be corrected (by intraoperative ultrasound). To make the most of the imaging-based guidance and improve the accuracy in open biopsy, I would suggest a minor modification of the procedure: before the usual wide durotomy and full exposure of the cortex, a small slit durotomy and corticotomy could be performed to pass the biopsy needle into the targets through the trajectories where the tissue is to be resected afterwards. This approach is necessary to minimise brain shift during the targeted biopsies for accurate co-registration and subsequent local correlation.

In future studies, a larger set of data points from a larger cohort of patients should permit multivariate regression analysis in search for relations between regional histopathological features and imaging characteristics, which is also useful for determining the within individual variances in such heterogeneous tumours.

Nevertheless, one should bear in mind that even with accurate targeted biopsy, the tissue sample assessed represents the pathological status of only a small portion of an often large and heterogeneous tumour. Likewise, even with complete removal, only a small part of the tumour tissue comes under microscopic investigation. There is thus some fear that such assessment may not be characteristic of the whole tumour. In vivo imaging could offer complementary information to the 'gold standard' and should also be taken into account in treatment planning and prognosis prediction.

7.3 Future work and applications

In the future [11C]-(*R*)PK11195 PET study on gliomas, a metabolite corrected plasma input function should be obtained and compared with the cerebellar input function

and the supervised cluster input function for further validation. This would generate a more accurate future input function accounting also for the vascular compartment which has been shown to have a significant specific binding.

Further studies would be needed to confirm our novel technique of TSPO quantification and use in glioma tissue. The refinement of this potential diagnostic tool would be of great value in clinical setting due to its easy and standardized application.

With respect to Methionine PET imaging, despite the technical difficulties and availability to be implemented in clinical routine, there are a variety of other amino acid tracers which could be of great use especially in patients where lesions are of difficult surgical access. In future I would suggest further work would be required to understand further the molecular transport system in the tumoural cells and relation to PET imaging.

Finally understanding the aetiology of the neuroinflammation in the normal appearing brain opens new horizons in the symptomatic treatment especially of patients with lower grade tumours and possibly in the understanding of the pathways of tumour invasion. Further work would be required combining DTI and TSPO imaging to identify the early changes in the white matter connected to the tumour and neuroinflammation of these tracts.

Appendices

Appendix 1 - TSPO 3D reconstruction in normal human brain

Veronese, et al. Kinetic modelling of [11C]PBR28 brain PET data with XBD173.

The stained slides were scanned at the University of Manchester (UoM) Bioimaging Facility under the supervision of trained imaging technicians competent in the use of a 3D Histech Pannoramic 250 Flash slide scanner (3DHISTECH Ltd. Budapest, HUNGARY). Once scanned, slides were stored on the UoM imaging database and were accessed from dedicated terminals using the Caseviewer software package (3DHISTECH Ltd). Caseviewer was used to set magnification and localise viewpoint to a specific and constant region of interest. Slides were converted manually from a .JPEG format into .TIFF files for upload into the ImageJ scientific image analysis and alteration tool. Regions of interest were converted manually from their native format ".mrcs" into .TIFF files using the bioformat plugin in ImageJ to facilitate further aligning and stacking.

Orientation of the slide stacks took place using the bioformat plugin in ImageJ with slides uploaded to the tool in a .TIFF format using the Bioimager plugin. Prior to stacking, RGB images were converted in ImageJ and were treated with colour deconvolution plugin (https://imagej.nih.gov/ij/) using the 'Fastred Fastblue DAB' setting in order to minimise interference from blue counterstaining. Generated images were further orientated and aligned automatically in ImageJ using the StackReg plugin with orientation a rigid approach. Whilst this approach was deemed the most appropriate, automatic orientation was not always accurate for this studies purpose and thus the TrackEM2 plugin was used to manually highlight regions of vascular similarity and finetune automatic orientation by hand.

It is worth noting that in order for stained regions to be visualised three dimensionally in the Imaris Biplane software (Bitplane AG Zurich, Switzerland), the stacks were altered from a red, green, blue channel format into greyscale following orientation. Imaris processed images as simply 'stained' and 'unstained' sections with background reduced at analyser's discretion. Stacks were uploaded in .TIFF, greyscale format and bitplane's Imaris 3D viewer was used to analyse the orientated slide

stacks and produce 3D images of baseline TSPO and CD31 distribution in healthy brain tissue.

An example of stacking and 3D reconstruction of vessels and vascular TSPO expression is reported below; eighty consecutive sections of frontal lobe including arachnoid (A), grey matter (GM) and white matter (WM) are first immunostained for CD31 (sections 1, 3, 5, …, 79) and TSPO (sections 2, 4, 6, …, 80). The sections are scanned and stacked using the Image J programme. This figure shows three dimensional reconstructions of a selected region of interested (ROI) in the cortex. Arbitrary colours are given to represent the vascular network in red and TSPO expression in green.

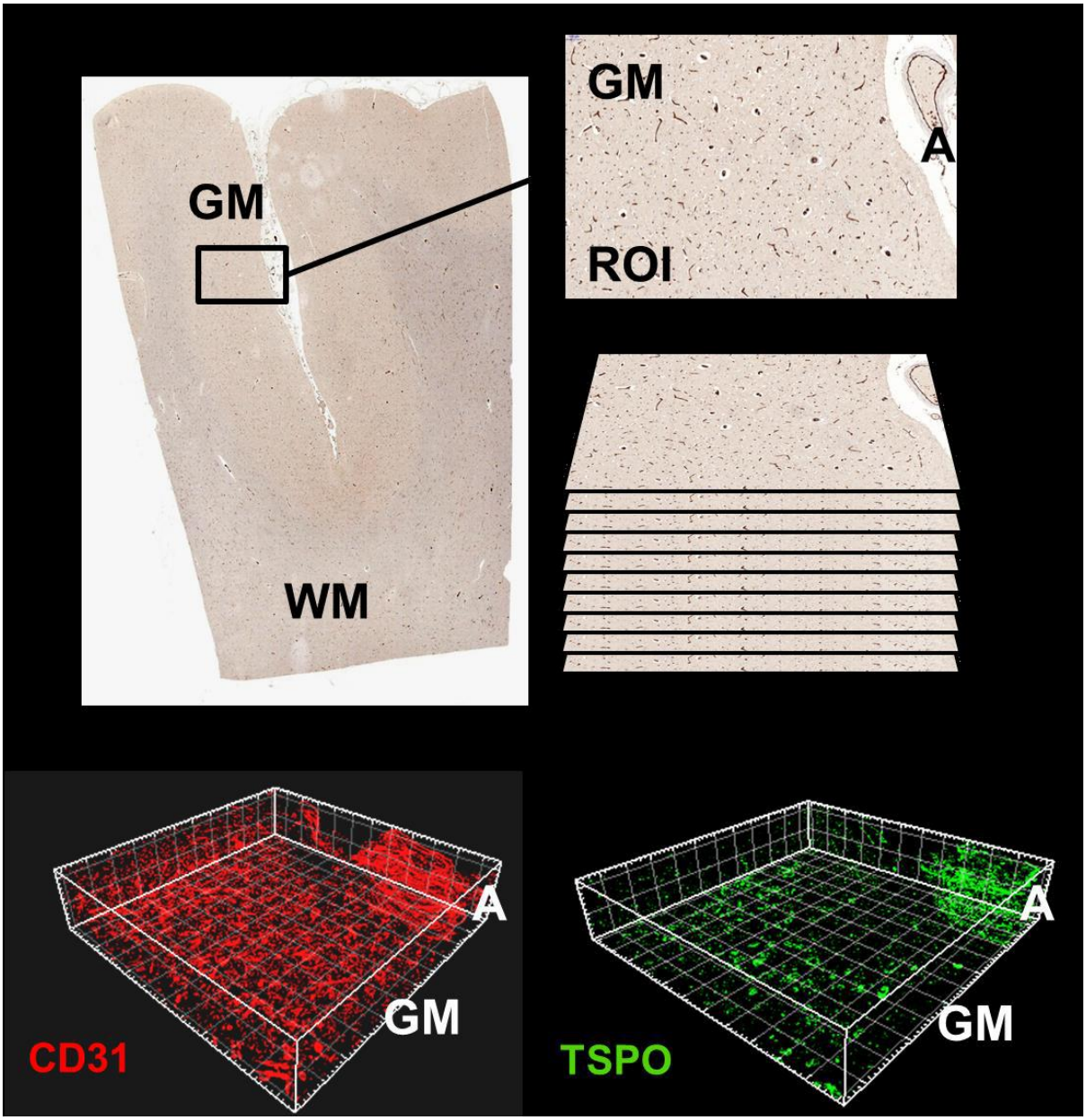

References

1. Lapointe, S., A. Perry, and N.A. Butowski, *Primary brain tumours in adults.* Lancet, 2018. **392**(10145): p. 432-446.
2. Louis, D.N., et al., *The 2016 World Health Organization Classification of Tumors of the Central Nervous System: a summary.* Acta Neuropathol, 2016. **131**(6): p. 803-20.
3. Eckel-Passow, J.E., et al., *Glioma Groups Based on 1p/19q, IDH, and TERT Promoter Mutations in Tumors.* N Engl J Med, 2015. **372**(26): p. 2499-508.
4. Jenkins, R.B., et al., *A t(1;19)(q10;p10) mediates the combined deletions of 1p and 19q and predicts a better prognosis of patients with oligodendroglioma.* Cancer Res, 2006. **66**(20): p. 9852-61.
5. van den Bent, M.J., et al., *Adjuvant procarbazine, lomustine, and vincristine chemotherapy in newly diagnosed anaplastic oligodendroglioma: long-term follow-up of EORTC brain tumor group study 26951.* J Clin Oncol, 2013. **31**(3): p. 344-50.
6. Guo, C., et al., *Isocitrate dehydrogenase mutations in gliomas: mechanisms, biomarkers and therapeutic target.* Current opinion in neurology, 2011. **24**(6): p. 648-652.
7. Takahashi, Y., et al., *Prognostic value of isocitrate dehydrogenase 1, O6-methylguanine-DNA methyltransferase promoter methylation, and 1p19q co-deletion in Japanese malignant glioma patients.* World J Surg Oncol, 2013. **11**: p. 284.
8. Tom, M.C., et al., *Malignant Transformation of Molecularly Classified Adult Low Grade Glioma.* Int J Radiat Oncol Biol Phys, 2019.
9. Nava, F., et al., *Survival effect of first- and second-line treatments for patients with primary glioblastoma: a cohort study from a prospective registry, 1997-2010.* Neuro Oncol, 2014. **16**(5): p. 719-27.
10. Stupp, R., et al., *Effects of radiotherapy with concomitant and adjuvant temozolomide versus radiotherapy alone on survival in glioblastoma in a randomised phase III study: 5-year analysis of the EORTC-NCIC trial.* Lancet Oncol, 2009. **10**(5): p. 459-66.
11. Koshy, M., et al., *Improved survival time trends for glioblastoma using the SEER 17 population-based registries.* J Neurooncol, 2012. **107**(1): p. 207-12.
12. van den Bent, M.J., et al., *Interim results from the CATNON trial (EORTC study 26053-22054) of treatment with concurrent and adjuvant temozolomide for 1p/19q non-co-deleted anaplastic glioma: a phase 3, randomised, open-label intergroup study.* Lancet (London, England), 2017. **390**(10103): p. 1645-1653.
13. Cairncross, G., et al., *Chemotherapy for anaplastic oligodendroglioma. National Cancer Institute of Canada Clinical Trials Group.* Journal of Clinical Oncology, 1994. **12**(10): p. 2013-2021.
14. van den Bent, M.J., et al., *Response rate and prognostic factors of recurrent oligodendroglioma treated with procarbazine, CCNU, and vincristine chemotherapy. Dutch Neuro-oncology Group.* Neurology, 1998. **51**(4): p. 1140-5.

15. Ghaffari-Rafi, A. and G. Samandouras, *Effect of Treatment Modalities on Progression-Free Survival and Overall Survival, in Molecularly Subtyped WHO Grade II Diffuse Gliomas: A Systematic Review.* World Neurosurg, 2019.
16. El-Hateer, H., et al., *Low-grade oligodendroglioma: an indolent but incurable disease?* 2009. **111**(2): p. 265.
17. Lebrun, C., et al., *Long-term outcome of oligodendrogliomas.* Neurology, 2004. **62**(10): p. 1783-1787.
18. Laws, E.R., et al., *Survival following surgery and prognostic factors for recently diagnosed malignant glioma: data from the Glioma Outcomes Project.* 2003. **99**(3): p. 467.
19. Curran, W.J., Jr, et al., *Recursive Partitioning Analysis of Prognostic Factors in Three Radiation Therapy Oncology Group Malignant Glioma Trials.* JNCI: Journal of the National Cancer Institute, 1993. **85**(9): p. 704-710.
20. Zhang, S., et al., *Texture analysis on conventional MRI images accurately predicts early malignant transformation of low-grade gliomas.* Eur Radiol, 2019. **29**(6): p. 2751-2759.
21. Bogdanska, M.U., et al., *A mathematical model describes the malignant transformation of low grade gliomas: Prognostic implications.* PLoS One, 2017. **12**(8): p. e0179999.
22. Pirzkall, A., et al., *Metabolic imaging of low-grade gliomas with three-dimensional magnetic resonance spectroscopy.* Int J Radiat Oncol Biol Phys, 2002. **53**(5): p. 1254-64.
23. Ohgaki, H. and P. Kleihues, *Population-based studies on incidence, survival rates, and genetic alterations in astrocytic and oligodendroglial gliomas.* J Neuropathol Exp Neurol, 2005. **64**(6): p. 479-89.
24. Gudinaviciene, I., D. Pranys, and E. Juozaityte, *Impact of morphology and biology on the prognosis of patients with gliomas.* Medicina (Kaunas), 2004. **40**(2): p. 112-20.
25. Walker, D.G. and A.H. Kaye, *Low grade glial neoplasms.* J Clin Neurosci, 2003. **10**(1): p. 1-13.
26. Law, M., et al., *Glioma grading: sensitivity, specificity, and predictive values of perfusion MR imaging and proton MR spectroscopic imaging compared with conventional MR imaging.* AJNR Am J Neuroradiol, 2003. **24**(10): p. 1989-98.
27. Danchaivijitr, N., et al., *Low-grade gliomas: do changes in rCBV measurements at longitudinal perfusion-weighted MR imaging predict malignant transformation?* Radiology, 2008. **247**(1): p. 170-8.
28. Fouke, S.J., et al., *The role of imaging in the management of adults with diffuse low grade glioma: A systematic review and evidence-based clinical practice guideline.* J Neurooncol, 2015. **125**(3): p. 457-79.
29. Murphy, E.S., et al., *Risk Factors for Malignant Transformation of Low-Grade Glioma.* Int J Radiat Oncol Biol Phys, 2018. **100**(4): p. 965-971.
30. Upadhyay, N. and A.D. Waldman, *Conventional MRI evaluation of gliomas.* The British journal of radiology, 2011. **84 Spec No 2**(Spec Iss 2): p. S107-S111.
31. Thust, S.C., et al., *Glioma imaging in Europe: A survey of 220 centres and recommendations for best clinical practice.* European radiology, 2018. **28**(8): p. 3306-3317.
32. Sugahara, T., et al., *Correlation of MR imaging-determined cerebral blood volume maps with histologic and angiographic determination of vascularity of gliomas.* AJR Am J Roentgenol, 1998. **171**(6): p. 1479-86.

33. Maia, A.C., Jr., et al., *Stereotactic biopsy guidance in adults with supratentorial nonenhancing gliomas: role of perfusion-weighted magnetic resonance imaging.* J Neurosurg, 2004. **101**(6): p. 970-6.
34. Minati, L. and W.P. Węglarz, *Physical foundations, models, and methods of diffusion magnetic resonance imaging of the brain: A review.* Concepts in Magnetic Resonance Part A, 2007. **30A**(5): p. 278-307.
35. Basser, P.J., J. Mattiello, and D. LeBihan, *Estimation of the effective self-diffusion tensor from the NMR spin echo.* J Magn Reson B, 1994. **103**(3): p. 247-54.
36. Basser, P.J., J. Mattiello, and D. LeBihan, *MR diffusion tensor spectroscopy and imaging.* Biophys J, 1994. **66**(1): p. 259-67.
37. Yang, D., et al., *Cerebral gliomas: prospective comparison of multivoxel 2D chemical-shift imaging proton MR spectroscopy, echoplanar perfusion and diffusion-weighted MRI.* Neuroradiology, 2002. **44**(8): p. 656-66.
38. Kono, K., et al., *The role of diffusion-weighted imaging in patients with brain tumors.* AJNR Am J Neuroradiol, 2001. **22**(6): p. 1081-8.
39. Fan, G., et al., *Usefulness of Diffusion/Perfusion-weighted MRI in Rat Gliomas: Correlation With Histopathology¹.* Academic Radiology, 2005. **12**(5): p. 640-651.
40. Sadeghi, N., et al., *Apparent diffusion coefficient and cerebral blood volume in brain gliomas: relation to tumor cell density and tumor microvessel density based on stereotactic biopsies.* AJNR Am J Neuroradiol, 2008. **29**(3): p. 476-82.
41. Gupta, R.K., et al., *Relationships between choline magnetic resonance spectroscopy, apparent diffusion coefficient and quantitative histopathology in human glioma.* J Neurooncol, 2000. **50**(3): p. 215-26.
42. Vargova, L., et al., *Diffusion parameters of the extracellular space in human gliomas.* Glia, 2003. **42**(1): p. 77-88.
43. Sinha, S., et al., *Diffusion Tensor MR Imaging of High-Grade Cerebral Gliomas.* American Journal of Neuroradiology, 2002. **23**(4): p. 520-527.
44. Inoue, T., et al., *Diffusion tensor imaging for preoperative evaluation of tumor grade in gliomas.* Clin Neurol Neurosurg, 2005. **107**(3): p. 174-80.
45. Papadopoulos, V., et al., *Translocator protein (18kDa): new nomenclature for the peripheral-type benzodiazepine receptor based on its structure and molecular function.* Trends Pharmacol Sci, 2006. **27**(8): p. 402-9.
46. Lacapère, J.J. and V. Papadopoulos, *Peripheral-type benzodiazepine receptor: structure and function of a cholesterol-binding protein in steroid and bile acid biosynthesis.* Steroids, 2003. **68**(7-8): p. 569-85.
47. Papadopoulos, V., *Structure and function of the peripheral-type benzodiazepine receptor in steroidogenic cells.* Proc Soc Exp Biol Med, 1998. **217**(2): p. 130-42.
48. Li, H. and V. Papadopoulos, *Peripheral-type benzodiazepine receptor function in cholesterol transport. Identification of a putative cholesterol recognition/interaction amino acid sequence and consensus pattern.* Endocrinology, 1998. **139**(12): p. 4991-7.
49. Li, F., et al., *Protein structure. Crystal structures of translocator protein (TSPO) and mutant mimic of a human polymorphism.* Science, 2015. **347**(6221): p. 555-8.
50. Batoko, H., V. Veljanovski, and P. Jurkiewicz, *Enigmatic Translocator protein (TSPO) and cellular stress regulation.* Trends Biochem Sci, 2015. **40**(9): p. 497-503.
51. Gavish, M., et al., *Enigma of the peripheral benzodiazepine receptor.* Pharmacol Rev, 1999. **51**(4): p. 629-50.

52. Li, F., et al., *Translocator Protein 18 kDa (TSPO): An Old Protein with New Functions?* Biochemistry, 2016. **55**(20): p. 2821-31.
53. Cosenza-Nashat, M., et al., *Expression of the translocator protein of 18 kDa by microglia, macrophages and astrocytes based on immunohistochemical localization in abnormal human brain.* Neuropathology and applied neurobiology, 2009. **35**(3): p. 306-328.
54. Kassiou, M., S.R. Meikle, and R.B. Banati, *Ligands for peripheral benzodiazepine binding sites in glial cells.* Brain Res Brain Res Rev, 2005. **48**(2): p. 207-10.
55. Black, K.L., K. Ikezaki, and A.W. Toga, *Imaging of brain tumors using peripheral benzodiazepine receptor ligands.* J Neurosurg, 1989. **71**(1): p. 113-8.
56. Venneti, S., B.J. Lopresti, and C.A. Wiley, *Molecular imaging of microglia/macrophages in the brain.* Glia, 2013. **61**(1): p. 10-23.
57. Banati, R.B., et al., *[11C](R)-PK11195 positron emission tomography imaging of activated microglia in vivo in Rasmussen's encephalitis.* Neurology, 1999. **53**(9): p. 2199-203.
58. Cagnin, A., et al., *In-vivo measurement of activated microglia in dementia.* Lancet, 2001. **358**(9280): p. 461-7.
59. Papadopoulos, V., J. Fan, and B. Zirkin, *Translocator protein (18 kDa): an update on its function in steroidogenesis.* J Neuroendocrinol, 2018. **30**(2).
60. Hirsch, J.D., et al., *Mitochondrial benzodiazepine receptors mediate inhibition of mitochondrial respiratory control.* Mol Pharmacol, 1989. **35**(1): p. 157-63.
61. Azarashvili, T., et al., *High-affinity peripheral benzodiazepine receptor ligand, PK11195, regulates protein phosphorylation in rat brain mitochondria under control of Ca(2+).* J Neurochem, 2005. **94**(4): p. 1054-62.
62. Scarf, A.M., et al., *Evidence for complex binding profiles and species differences at the translocator protein (TSPO) (18 kDa).* Curr Mol Med, 2012. **12**(4): p. 488-93.
63. Chauveau, F., et al., *Nuclear imaging of neuroinflammation: a comprehensive review of [11C]PK11195 challengers.* Eur J Nucl Med Mol Imaging, 2008. **35**(12): p. 2304-19.
64. Boche, D., A. Gerhard, and E. Rodriguez-Vieitez, *Prospects and challenges of imaging neuroinflammation beyond TSPO in Alzheimer's disease.* Eur J Nucl Med Mol Imaging, 2019.
65. Su, Z., et al., *The 18-kDa mitochondrial translocator protein in human gliomas: an 11C-(R)PK11195 PET imaging and neuropathology study.* J Nucl Med, 2015. **56**(4): p. 512-7.
66. Rechichi, M., et al., *TSPO over-expression increases motility, transmigration and proliferation properties of C6 rat glioma cells.* Biochimica et Biophysica Acta (BBA) - Molecular Basis of Disease, 2008. **1782**(2): p. 118-125.
67. Cornu, P., et al., *Increase in omega 3 (peripheral-type benzodiazepine) binding site densities in different types of human brain tumours. A quantitative autoradiography study.* Acta Neurochir (Wien), 1992. **119**(1-4): p. 146-52.
68. Miettinen, H., et al., *Expression of peripheral-type benzodiazepine receptor and diazepam binding inhibitor in human astrocytomas: relationship to cell proliferation.* Cancer Res, 1995. **55**(12): p. 2691-5.
69. Vlodavsky, E. and J.F. Soustiel, *Immunohistochemical expression of peripheral benzodiazepine receptors in human astrocytomas and its correlation with grade of malignancy, proliferation, apoptosis and survival.* J Neurooncol, 2007. **81**(1): p. 1-7.
70. Konigsrainer, I., et al., *Increased translocator protein (TSPO) mRNA levels in colon but not in rectum carcinoma.* Eur Surg Res, 2007. **39**(6): p. 359-63.

71. Katz, Y., A. Eitan, and M. Gavish, *Increase in peripheral benzodiazepine binding sites in colonic adenocarcinoma.* Oncology, 1990. **47**(2): p. 139-42.
72. Maaser, K., et al., *Overexpression of the peripheral benzodiazepine receptor is a relevant prognostic factor in stage III colorectal cancer.* Clin Cancer Res, 2002. **8**(10): p. 3205-9.
73. Sutter, A.P., et al., *Specific ligands of the peripheral benzodiazepine receptor induce apoptosis and cell cycle arrest in human esophageal cancer cells.* Int J Cancer, 2002. **102**(4): p. 318-27.
74. Mukherjee, S. and S.K. Das, *Translocator protein (TSPO) in breast cancer.* Curr Mol Med, 2012. **12**(4): p. 443-57.
75. Beinlich, A., et al., *Relation of cell proliferation to expression of peripheral benzodiazepine receptors in human breast cancer cell lines.* Biochem Pharmacol, 2000. **60**(3): p. 397-402.
76. Galiegue, S., et al., *Immunohistochemical assessment of the peripheral benzodiazepine receptor in breast cancer and its relationship with survival.* Clin Cancer Res, 2004. **10**(6): p. 2058-64.
77. Venturini, I., et al., *Increased expression of peripheral benzodiazepine receptors and diazepam binding inhibitor in human tumors sited in the liver.* Life Sci, 1999. **65**(21): p. 2223-31.
78. Fafalios, A., et al., *Translocator protein blockade reduces prostate tumor growth.* Clin Cancer Res, 2009. **15**(19): p. 6177-84.
79. Roncaroli, F., et al., *TSPO expression in brain tumours: is TSPO a target for brain tumour imaging?* Clin Transl Imaging, 2016. **4**: p. 145-156.
80. Herholz, K., et al., *11C-methionine PET for differential diagnosis of low-grade gliomas.* Neurology, 1998. **50**(5): p. 1316-22.
81. Pirotte, B., et al., *Comparison of 18F-FDG and 11C-methionine for PET-guided stereotactic brain biopsy of gliomas.* J Nucl Med, 2004. **45**(8): p. 1293-8.
82. Pirotte, B.J., et al., *Positron emission tomography-guided volumetric resection of supratentorial high-grade gliomas: a survival analysis in 66 consecutive patients.* Neurosurgery, 2009. **64**(3): p. 471-81; discussion 481.
83. Grosu, A.L., et al., *L-(methyl-11C) methionine positron emission tomography for target delineation in resected high-grade gliomas before radiotherapy.* Int J Radiat Oncol Biol Phys, 2005. **63**(1): p. 64-74.
84. Rapp, M., et al., *Diagnostic performance of 18F-FET PET in newly diagnosed cerebral lesions suggestive of glioma.* J Nucl Med, 2013. **54**(2): p. 229-35.
85. Pafundi, D.H., et al., *Biopsy validation of 18F-DOPA PET and biodistribution in gliomas for neurosurgical planning and radiotherapy target delineation: results of a prospective pilot study.* Neuro Oncol, 2013. **15**(8): p. 1058-67.
86. Grosu, A.L., et al., *An interindividual comparison of O-(2-[18F]fluoroethyl)-L-tyrosine (FET)- and L-[methyl-11C]methionine (MET)-PET in patients with brain gliomas and metastases.* Int J Radiat Oncol Biol Phys, 2011. **81**(4): p. 1049-58.
87. Watabe, T. and J. Hatazawa, *(18)F-FBPA as a tumor specific tracer of L-type amino acid transporter 1 (LAT1): PET evaluation in tumor and inflammation compared to (18)F-FDG and (11)C-methionine.* Hell J Nucl Med, 2015. **18 Suppl 1**: p. 149.
88. Yang, X., et al., *Preclinical evaluation of an 18F-trifluoroborate methionine derivative for glioma imaging.* European Journal of Nuclear Medicine and Molecular Imaging, 2018. **45**(4): p. 585-592.
89. Kido, Y., et al., *Molecular and functional identification of large neutral amino acid transporters LAT1 and LAT2 and their pharmacological relevance at the blood-brain barrier.* J Pharm Pharmacol, 2001. **53**(4): p. 497-503.

90. Derlon, J.M., et al., *Non-invasive grading of oligodendrogliomas: correlations between in vivo metabolic pattern and histopathology.* European Journal of Nuclear Medicine, 2000. **27**(7): p. 778-787.
91. Kracht, L.W., et al., *Delineation of brain tumor extent with [11C]L-methionine positron emission tomography: local comparison with stereotactic histopathology.* Clin Cancer Res, 2004. **10**(21): p. 7163-70.
92. Nuutinen, J., et al., *Radiotherapy treatment planning and long-term follow-up with [(11)C]methionine PET in patients with low-grade astrocytoma.* Int J Radiat Oncol Biol Phys, 2000. **48**(1): p. 43-52.
93. Kracht, L.W., et al., *Methyl-[11C]- l-methionine uptake as measured by positron emission tomography correlates to microvessel density in patients with glioma.* Eur J Nucl Med Mol Imaging, 2003. **30**(6): p. 868-73.
94. Saito, T., et al., *¹¹C-Methionine Uptake Correlates with Combined 1p and 19q Loss of Heterozygosity in Oligodendroglial Tumors.* American Journal of Neuroradiology, 2013. **34**(1): p. 85-91.
95. Chung, J.K., et al., *Usefulness of 11C-methionine PET in the evaluation of brain lesions that are hypo- or isometabolic on 18F-FDG PET.* Eur J Nucl Med Mol Imaging, 2002. **29**(2): p. 176-82.
96. Goldman, S., et al., *Regional methionine and glucose uptake in high-grade gliomas: a comparative study on PET-guided stereotactic biopsy.* Journal of nuclear medicine : official publication, Society of Nuclear Medicine, 1997. **38**(9): p. 1459-1462.
97. Pauleit, D., et al., *O-(2-[18F]fluoroethyl)-L-tyrosine PET combined with MRI improves the diagnostic assessment of cerebral gliomas.* Brain, 2005. **128**(Pt 3): p. 678-87.
98. Conde, J.R. and W.J. Streit, *Microglia in the aging brain.* J Neuropathol Exp Neurol, 2006. **65**(3): p. 199-203.
99. Dodel, R., et al., *Minocycline 1-year therapy in multiple-system-atrophy: effect on clinical symptoms and [(11)C] (R)-PK11195 PET (MEMSA-trial).* Mov Disord, 2010. **25**(1): p. 97-107.
100. Badie, B., et al., *Dexamethasone-induced abolition of the inflammatory response in an experimental glioma model: a flow cytometry study.* J Neurosurg, 2000. **93**(4): p. 634-9.
101. Kaur, C., S.T. Dheen, and E.A. Ling, *From blood to brain: amoeboid microglial cell, a nascent macrophage and its functions in developing brain.* Acta Pharmacol Sin, 2007. **28**(8): p. 1087-96.
102. Drew, P.D. and J.A. Chavis, *Inhibition of microglial cell activation by cortisol.* Brain Res Bull, 2000. **52**(5): p. 391-6.
103. Hu, L.S., et al., *Optimized Preload Leakage-Correction Methods to Improve the Diagnostic Accuracy of Dynamic Susceptibility-Weighted Contrast-Enhanced Perfusion MR Imaging in Posttreatment Gliomas.* American Journal of Neuroradiology, 2010. **31**(1): p. 40-48.
104. Shah, F., et al., *Synthesis of the enantiomers of [N-methyl-11C]PK 11195 and comparison of their behaviours as radioligands for PK binding sites in rats.* Nucl Med Biol, 1994. **21**(4): p. 573-81.
105. Cremer, J.E., et al., *The distribution of radioactivity in brains of rats given [N-methyl-11C]PK 11195 in vivo after induction of a cortical ischaemic lesion.* Int J Rad Appl Instrum B, 1992. **19**(2): p. 159-66.
106. Camsonne, R., et al., *Synthesis of N-(11C) methyl, N-(methyl-1 propyl), (chloro-2 phenyl)-1 isoquinoleine carboxamide-3 (PK 11195): A new ligand for peripheral*

benzodiazepine receptors. Journal of Labelled Compounds and Radiopharmaceuticals, 1984. **21**(10): p. 985-991.
107. Wager, C.A.B. and S.A. Miller, *Two robust, efficient syntheses of [phenyl ring-U-14C]indole through use of [phenyl ring-U-14C]aniline.* Journal of Labelled Compounds and Radiopharmaceuticals, 2006. **49**(7): p. 615-622.
108. Jong, H.W.A.M.d., et al., *Performance evaluation of the ECAT HRRT: an LSO-LYSO double layer high resolution, high sensitivity scanner.* Physics in Medicine and Biology, 2007. **52**(5): p. 1505-1526.
109. Sossi, V., et al., *The second generation HRRT - A multi-centre scanner performance investigation*. Vol. 4. 2005. 2195-2199.
110. Daghighiam, F., et al. *Evaluation of cerium doped lutetium oxyorthosilicate (LSO) scintillation crystals for PET*. in *IEEE Conference on Nuclear Science Symposium and Medical Imaging*. 1992.
111. Heiss, W.-D., et al., *Metabolic Rates in Small Brain Nuclei Determined by High-Resolution PET.* Journal of Nuclear Medicine, 2004. **45**(11): p. 1811-1815.
112. Michel, C., et al. *Reconstruction strategies for the HRRT*. in *2000 IEEE Nuclear Science Symposium. Conference Record (Cat. No.00CH37149)*. 2000.
113. Byars, L.G., et al. *Variance reduction on randoms from coincidence histograms for the HRRT*. in *IEEE Nuclear Science Symposium Conference Record, 2005*. 2005.
114. Sibomana, M., et al. *Simultaneous measurement of transmission and emission contamination using a collimated /sup 137/Cs point source for the HRRT*. in *IEEE Symposium Conference Record Nuclear Science 2004.* 2004.
115. Watson, C.C., *New, faster, image-based scatter correction for 3D PET.* IEEE Transactions on Nuclear Science, 2000. **47**(4): p. 1587-1594.
116. Cízek, J., et al., *Fast and robust registration of PET and MR images of human brain.* NeuroImage, 2004. **22**(1): p. 434-442.
117. Lammertsma, A.A. and S.P. Hume, *Simplified reference tissue model for PET receptor studies.* Neuroimage, 1996. **4**(3 Pt 1): p. 153-8.
118. Turkheimer, F.E., et al., *Reference and Target Region Modeling of [11C]-(R)-PK11195 Brain Studies.* Journal of Nuclear Medicine, 2007. **48**(1): p. 158-167.
119. Su, Z., et al., *[^{11}C]-(R)PK11195 tracer kinetics in the brain of glioma patients and a comparison of two referencing approaches.* European journal of nuclear medicine and molecular imaging, 2013. **40**(9): p. 1406-1419.
120. Bland, J.M. and D.G. Altman, *Measuring agreement in method comparison studies.* Stat Methods Med Res, 1999. **8**(2): p. 135-60.
121. Geistanger, A., et al., *Local regression: a new approach for measurement system comparison analysis.* Clinical chemistry and laboratory medicine, 2008. **46**(9): p. 1211-1219.
122. Lee, J., *Comparison of variance between correlated samples.* Bioinformatics, 1992. **8**(4): p. 405-406.
123. Ashburner, J. and K.J. Friston, *Unified segmentation.* Neuroimage, 2005. **26**(3): p. 839-51.
124. Boxerman, J.L., K.M. Schmainda, and R.M. Weisskoff, *Relative cerebral blood volume maps corrected for contrast agent extravasation significantly correlate with glioma tumor grade, whereas uncorrected maps do not.* AJNR Am J Neuroradiol, 2006. **27**(4): p. 859-67.
125. Bleeker, E.J., M.A. van Buchem, and M.J. van Osch, *Optimal location for arterial input function measurements near the middle cerebral artery in first-pass perfusion MRI.* J Cereb Blood Flow Metab, 2009. **29**(4): p. 840-52.

126. Wetzel, S.G., et al., *Relative cerebral blood volume measurements in intracranial mass lesions: interobserver and intraobserver reproducibility study.* Radiology, 2002. **224**(3): p. 797-803.
127. Smith, S.M., et al., *Advances in functional and structural MR image analysis and implementation as FSL.* Neuroimage, 2004. **23 Suppl 1**: p. S208-19.
128. Lewis, D., et al., *Inflammation and vascular permeability correlate with growth in sporadic vestibular schwannoma.* Neuro-oncology, 2019. **21**(3): p. 314-325.
129. Yushkevich, P.A., et al., *User-guided 3D active contour segmentation of anatomical structures: significantly improved efficiency and reliability.* Neuroimage, 2006. **31**(3): p. 1116-28.
130. van den Bent, M.J., et al., *Response assessment in neuro-oncology (a report of the RANO group): assessment of outcome in trials of diffuse low-grade gliomas.* Lancet Oncol, 2011. **12**(6): p. 583-93.
131. Wesseling, P. and D. Capper, *WHO 2016 Classification of gliomas.* Neuropathol Appl Neurobiol, 2018. **44**(2): p. 139-150.
132. Veronese, M., et al., *Kinetic modelling of [(11)C]PBR28 for 18 kDa translocator protein PET data: A validation study of vascular modelling in the brain using XBD173 and tissue analysis.* J Cereb Blood Flow Metab, 2018. **38**(7): p. 1227-1242.
133. Ondracek, A., et al., *CBTRUS Statistical Report: Primary Brain and Central Nervous System Tumors Diagnosed in the United States in 2006-2010.* Neuro-Oncology, 2013. **15**(suppl_2): p. ii1-ii56.
134. Forst, D.A., et al., *Low-grade gliomas.* The oncologist, 2014. **19**(4): p. 403-413.
135. Roberts, M., et al., *Diffuse low grade glioma after the 2016 WHO update, seizure characteristics, imaging correlates and outcomes.* Clin Neurol Neurosurg, 2018. **175**: p. 9-15.
136. Collins, V.P., *Brain tumours: classification and genes.* J Neurol Neurosurg Psychiatry, 2004. **75 Suppl 2**(Suppl 2): p. ii2-11.
137. Tang, B.N., et al., *Semi-quantification of methionine uptake and flair signal for the evaluation of chemotherapy in low-grade oligodendroglioma.* J Neurooncol, 2005. **71**(2): p. 161-8.
138. Price, S.J., et al., *Improved delineation of glioma margins and regions of infiltration with the use of diffusion tensor imaging: an image-guided biopsy study.* AJNR Am J Neuroradiol, 2006. **27**(9): p. 1969-74.
139. Herholz, K., *Brain Tumors: An Update on Clinical PET Research in Gliomas.* Semin Nucl Med, 2017. **47**(1): p. 5-17.
140. Herholz, K., et al., *Brain tumors.* Semin Nucl Med, 2012. **42**(6): p. 356-70.
141. Herholz, K., D. Coope, and A. Jackson, *Metabolic and molecular imaging in neuro-oncology.* Lancet Neurol, 2007. **6**(8): p. 711-24.
142. Albert, N.L., et al., *Response Assessment in Neuro-Oncology working group and European Association for Neuro-Oncology recommendations for the clinical use of PET imaging in gliomas.* Neuro Oncol, 2016. **18**(9): p. 1199-208.
143. la Fougere, C., et al., *Molecular imaging of gliomas with PET: opportunities and limitations.* Neuro Oncol, 2011. **13**(8): p. 806-19.
144. Yoo, M.Y., et al., *Prognostic Value of Metabolic Tumor Volume on (11)C-Methionine PET in Predicting Progression-Free Survival in High-Grade Glioma.* Nuclear medicine and molecular imaging, 2015. **49**(4): p. 291-297.
145. Galldiks, N., et al., *Volumetry of [(11)C]-methionine PET uptake and MRI contrast enhancement in patients with recurrent glioblastoma multiforme.* Eur J Nucl Med Mol Imaging, 2010. **37**(1): p. 84-92.

146. Dunn, K.W., M.M. Kamocka, and J.H. McDonald, *A practical guide to evaluating colocalization in biological microscopy.* American journal of physiology. Cell physiology, 2011. **300**(4): p. C723-C742.
147. Tomasi, G., et al., *Novel Reference Region Model Reveals Increased Microglial and Reduced Vascular Binding of 11C-(R)-PK11195 in Patients with Alzheimer's Disease.* Journal of Nuclear Medicine, 2008. **49**(8): p. 1249-1256.
148. Rizzo, G., et al., *Generalization of endothelial modelling of TSPO PET imaging: Considerations on tracer affinities.* J Cereb Blood Flow Metab, 2019. **39**(5): p. 874-885.
149. Su, Z., et al., *Microglial activation in normal-appearing brain regions of patients with cerebral glioma: a cross-sectional study.* The Lancet, 2017. **389**: p. S92.
150. Kumar, A., et al., *Evaluation of age-related changes in translocator protein (TSPO) in human brain using 11C-[R]-PK11195 PET.* Journal of Neuroinflammation, 2012. **9**(1): p. 232.
151. Caseiras, G.B., et al., *Inclusion or exclusion of intratumoral vessels in relative cerebral blood volume characterization in low-grade gliomas: does it make a difference?* AJNR Am J Neuroradiol, 2008. **29**(6): p. 1140-1.
152. Bagley, L.J., et al., *Gliomas: correlation of magnetic susceptibility artifact with histologic grade.* Radiology, 1997. **202**(2): p. 511-516.
153. Caulo, M., et al., *Data-driven Grading of Brain Gliomas: A Multiparametric MR Imaging Study.* Radiology, 2014. **272**(2): p. 494-503.
154. Yoon, J.H., et al., *Grading of cerebral glioma with multiparametric MR imaging and 18F-FDG-PET: concordance and accuracy.* Eur Radiol, 2014. **24**(2): p. 380-9.
155. Kunz, M., et al., *Hot spots in dynamic (18)FET-PET delineate malignant tumor parts within suspected WHO grade II gliomas.* Neuro Oncol, 2011. **13**(3): p. 307-16.
156. van den Bent, M.J., *Interobserver variation of the histopathological diagnosis in clinical trials on glioma: a clinician's perspective.* Acta Neuropathol, 2010. **120**(3): p. 297-304.
157. Tien, R.D., et al., *MR imaging of high-grade cerebral gliomas: value of diffusion-weighted echoplanar pulse sequences.* AJR Am J Roentgenol, 1994. **162**(3): p. 671-7.
158. Okita, Y., et al., *Stereotactic image-based histological analysis reveals a correlation between (11)C-methionine uptake and MGMT promoter methylation in non-enhancing gliomas.* Oncol Lett, 2018. **16**(2): p. 1924-1930.
159. Ostergaard, L., et al., *High resolution measurement of cerebral blood flow using intravascular tracer bolus passages. Part II: Experimental comparison and preliminary results.* Magn Reson Med, 1996. **36**(5): p. 726-36.
160. Ernst, T., et al., *Correlation of regional cerebral blood flow from perfusion MRI and spect in normal subjects.* Magn Reson Imaging, 1999. **17**(3): p. 349-54.
161. Nojiri, T., et al., *Contributions of biological tumor parameters to the incorporation rate of l-[methyl-11C] methionine into astrocytomas and oligodendrogliomas.* Journal of Neuro-Oncology, 2009. **93**(2): p. 233-241.
162. Hilario, A., et al., *The added value of apparent diffusion coefficient to cerebral blood volume in the preoperative grading of diffuse gliomas.* AJNR Am J Neuroradiol, 2012. **33**(4): p. 701-7.
163. Gumprecht, H.K., D.C. Widenka, and C.B. Lumenta, *BrainLab VectorVision Neuronavigation System: technology and clinical experiences in 131 cases.* Neurosurgery, 1999. **44**(1): p. 97-104; discussion 104-5.

164. Ringel, F., et al., *VarioGuide: a new frameless image-guided stereotactic system--accuracy study and clinical assessment.* Neurosurgery, 2009. **64**(5 Suppl 2): p. 365-71; discussion 371-3.
165. Coope, D.J., et al., *Evaluation of Primary Brain Tumors Using 11C-Methionine PET with Reference to a Normal Methionine Uptake Map.* Journal of Nuclear Medicine, 2007. **48**(12): p. 1971-1980.
166. Spampinato, M.V., et al., *Cerebral blood volume measurements and proton MR spectroscopy in grading of oligodendroglial tumors.* AJR Am J Roentgenol, 2007. **188**(1): p. 204-12.
167. Emblem, K.E., et al., *Automatic vessel removal in gliomas from dynamic susceptibility contrast imaging.* Magn Reson Med, 2009. **61**(5): p. 1210-7.
168. Burnet, N.G., et al., *Years of life lost (YLL) from cancer is an important measure of population burden--and should be considered when allocating research funds.* Br J Cancer, 2005. **92**(2): p. 241-5.
169. Verburg, N., et al., *Improved detection of diffuse glioma infiltration with imaging combinations: a diagnostic accuracy study.* Neuro Oncol, 2019.
170. Verburg, N., et al., *Accurate Delineation of Glioma Infiltration by Advanced PET/MR Neuro-Imaging (FRONTIER Study): A Diagnostic Study Protocol.* Neurosurgery, 2016. **79**(4): p. 535-40.
171. Durst, C.R., et al., *Multimodal MR imaging model to predict tumor infiltration in patients with gliomas.* Neuroradiology, 2014. **56**(2): p. 107-15.
172. Sahm, F., et al., *Addressing Diffuse Glioma as a Systemic Brain Disease With Single-Cell Analysis.* Archives of Neurology, 2012. **69**(4): p. 523-526.
173. de Groot, M., et al., *Epilepsy in patients with a brain tumour: focal epilepsy requires focused treatment.* Brain, 2012. **135**(Pt 4): p. 1002-16.
174. Norris, G.T. and J. Kipnis, *Immune cells and CNS physiology: Microglia and beyond.* The Journal of Experimental Medicine, 2019. **216**(1): p. 60-70.
175. Roggendorf, W., S. Strupp, and W. Paulus, *Distribution and characterization of microglia/macrophages in human brain tumors.* Acta Neuropathol, 1996. **92**(3): p. 288-93.
176. Graeber, M.B., B.W. Scheithauer, and G.W. Kreutzberg, *Microglia in brain tumors.* Glia, 2002. **40**(2): p. 252-9.
177. Badie, B. and J.M. Schartner, *Flow cytometric characterization of tumor-associated macrophages in experimental gliomas.* Neurosurgery, 2000. **46**(4): p. 957-61; discussion 961-2.
178. Pappata, S., et al., *Thalamic microglial activation in ischemic stroke detected in vivo by PET and [11C]PK1195.* Neurology, 2000. **55**(7): p. 1052-4.
179. Thiel, A., et al., *The temporal dynamics of poststroke neuroinflammation: a longitudinal diffusion tensor imaging-guided PET study with 11C-PK11195 in acute subcortical stroke.* J Nucl Med, 2010. **51**(9): p. 1404-12.
180. Cagnin, A., et al., *In vivo visualization of activated glia by [11C] (R)-PK11195-PET following herpes encephalitis reveals projected neuronal damage beyond the primary focal lesion.* Brain, 2001. **124**(Pt 10): p. 2014-27.
181. Unterrainer, M., et al., *Comparison of (18)F-GE-180 and dynamic (18)F-FET PET in high grade glioma: a double-tracer pilot study.* Eur J Nucl Med Mol Imaging, 2019. **46**(3): p. 580-590.
182. Unterrainer, M., et al., *Detection of Cerebrospinal Fluid Dissemination of Recurrent Glioblastoma Using TSPO-PET With 18F-GE-180.* Clinical nuclear medicine, 2018. **43**(7): p. 518-519.

183. Albert, N.L., et al., *TSPO PET for glioma imaging using the novel ligand (18)F-GE-180: first results in patients with glioblastoma.* Eur J Nucl Med Mol Imaging, 2017. **44**(13): p. 2230-2238.
184. Pappata, S., et al., *PET study of carbon-11-PK 11195 binding to peripheral type benzodiazepine sites in glioblastoma: a case report.* J Nucl Med, 1991. **32**(8): p. 1608-10.
185. Takaya, S., et al., *The lack of expression of the peripheral benzodiazepine receptor characterises microglial response in anaplastic astrocytomas.* Journal of neuro-oncology, 2007. **85**(1): p. 95-103.
186. Junck, L., et al., *PET imaging of human gliomas with ligands for the peripheral benzodiazepine binding site.* Ann Neurol, 1989. **26**(6): p. 752-8.
187. Hong, I.K., et al., *Ultra Fast Symmetry and SIMD-Based Projection-Backprojection (SSP) Algorithm for 3-D PET Image Reconstruction.* IEEE Transactions on Medical Imaging, 2007. **26**(6): p. 789-803.
188. Hammers, A., et al., *Statistical neuroanatomy of the human inferior frontal gyrus and probabilistic atlas in a standard stereotaxic space.* Hum Brain Mapp, 2007. **28**(1): p. 34-48.
189. Jucaite, A., et al., *Kinetic analysis and test-retest variability of the radioligand [11C](R)-PK11195 binding to TSPO in the human brain - a PET study in control subjects.* EJNMMI Res, 2012. **2**: p. 15.
190. Richards, E.M., et al., *PET radioligand binding to translocator protein (TSPO) is increased in unmedicated depressed subjects.* EJNMMI research, 2018. **8**(1): p. 57-57.
191. Scheffer, I.E., et al., *ILAE classification of the epilepsies: Position paper of the ILAE Commission for Classification and Terminology.* Epilepsia, 2017. **58**(4): p. 512-521.
192. Turkheimer, F.E., C.B. Smith, and K. Schmidt, *Estimation of the Number of "True" Null Hypotheses in Multivariate Analysis of Neuroimaging Data.* NeuroImage, 2001. **13**(5): p. 920-930.
193. BrainUK. Available from: www.southampton.ac.uk/brainuk.
194. SemmelWeis. Available from: http://semmelweis.hu/hbtb/.
195. Alafuzoff, I., et al., *Staging/typing of Lewy body related alpha-synuclein pathology: a study of the BrainNet Europe Consortium.* Acta Neuropathol, 2009. **117**(6): p. 635-52.
196. Hasegawa-Ishii, S., et al., *Morphological impairments in microglia precede age-related neuronal degeneration in senescence-accelerated mice.* Neuropathology, 2011. **31**(1): p. 20-28.
197. Byun, H., et al., *Cochlear Dead Regions in Sporadic Unilateral Vestibular Schwannomas Using the Threshold-Equalizing Noise Test.* Audiol Neurootol, 2019: p. 1-8.
198. Librizzi, L., et al., *Seizure-induced brain-borne inflammation sustains seizure recurrence and blood-brain barrier damage.* Ann Neurol, 2012. **72**(1): p. 82-90.
199. Butler, T., et al., *Transient and chronic seizure-induced inflammation in human focal epilepsy.* Epilepsia, 2016. **57**(9): p. e191-4.
200. Hirvonen, J., et al., *Increased in vivo expression of an inflammatory marker in temporal lobe epilepsy.* J Nucl Med, 2012. **53**(2): p. 234-40.
201. Gershen, L.D., et al., *Neuroinflammation in Temporal Lobe Epilepsy Measured Using Positron Emission Tomographic Imaging of Translocator Protein.* JAMA Neurol, 2015. **72**(8): p. 882-8.
202. Choi, J., et al., *Cellular injury and neuroinflammation in children with chronic intractable epilepsy.* J Neuroinflammation, 2009. **6**: p. 38.

203. Najjar, S., et al., *Refractory epilepsy associated with microglial activation.* Neurologist, 2011. **17**(5): p. 249-54.
204. Zhao, X., et al., *Noninflammatory Changes of Microglia Are Sufficient to Cause Epilepsy.* Cell Rep, 2018. **22**(8): p. 2080-2093.
205. Nowak, M., et al., *Minocycline as potent anticonvulsant in a patient with astrocytoma and drug resistant epilepsy.* Seizure, 2012. **21**(3): p. 227-8.
206. Vezzani, A., et al., *Epilepsy and brain inflammation.* Exp Neurol, 2013. **244**: p. 11-21.
207. Block, M.L., L. Zecca, and J.S. Hong, *Microglia-mediated neurotoxicity: uncovering the molecular mechanisms.* Nat Rev Neurosci, 2007. **8**(1): p. 57-69.
208. Kim, H.J., et al., *Histone deacetylase inhibitors exhibit anti-inflammatory and neuroprotective effects in a rat permanent ischemic model of stroke: multiple mechanisms of action.* J Pharmacol Exp Ther, 2007. **321**(3): p. 892-901.
209. Black, J.A., S. Liu, and S.G. Waxman, *Sodium channel activity modulates multiple functions in microglia.* Glia, 2009. **57**(10): p. 1072-81.
210. Hambardzumyan, D., D.H. Gutmann, and H. Kettenmann, *The role of microglia and macrophages in glioma maintenance and progression.* Nat Neurosci, 2016. **19**(1): p. 20-7.
211. Li, W. and M.B. Graeber, *The molecular profile of microglia under the influence of glioma.* Neuro Oncol, 2012. **14**(8): p. 958-78.
212. Charles, N.A., et al., *The brain tumor microenvironment.* Glia, 2011. **59**(8): p. 1169-80.
213. Markovic, D.S., et al., *Minocycline reduces glioma expansion and invasion by attenuating microglial MT1-MMP expression.* Brain Behav Immun, 2011. **25**(4): p. 624-8.
214. Owen, D.R., et al., *An 18-kDa translocator protein (TSPO) polymorphism explains differences in binding affinity of the PET radioligand PBR28.* J Cereb Blood Flow Metab, 2012. **32**(1): p. 1-5.
215. Owen, D.R.J., et al., *Mixed-affinity binding in humans with 18-kDa translocator protein ligands.* Journal of nuclear medicine : official publication, Society of Nuclear Medicine, 2011. **52**(1): p. 24-32.
216. Xu, W., et al., *The performance of 11C-Methionine PET in the differential diagnosis of glioma recurrence.* Oncotarget, 2017. **8**(53): p. 91030-91039.
217. Engelhorn, T., et al., *Cellular characterization of the peritumoral edema zone in malignant brain tumors.* Cancer Science, 2009. **100**(10): p. 1856-1862.
218. Shinonaga, M., et al., *Immunohistological evaluation of macrophage infiltrates in brain tumors. Correlation with peritumoral edema.* J Neurosurg, 1988. **68**(2): p. 259-65.
219. Butler, T., et al., *Imaging inflammation in a patient with epilepsy due to focal cortical dysplasia.* J Neuroimaging, 2013. **23**(1): p. 129-31.
220. Roelcke, U., et al., *Association of rubidium and C-methionine uptake in brain tumors measured by positron emission tomography.* J Neurooncol, 1996. **27**(2): p. 163-71.
221. Langen, K.-J., et al., *Transport Mechanisms of 3-[123I]Iodo-α-Methyl-L-Tyrosine in a Human Glioma Cell Line: Comparison with [3H-methyl]-L-Methionine.* Journal of Nuclear Medicine, 2000. **41**(7): p. 1250-1255.